Fachbereich Mathematik und Naturwissenschaften
Fachgruppe Physik
Bergische Universität
Wuppertal

Measurement of the $t\bar{t}$ invariant Mass Distribution and Search for $t\bar{t}$ Resonances

Maren Vaupel

März 2006
WUB-DIS 2006-01

Die Dissertation kann wie folgt zitiert werden:

urn:nbn:de:hbz:468-20060497
[http://nbn-resolving.de/urn/resolver.pl?urn=urn%3Anbn%3Ade%3Ahbz%3A468-20060497]

Contents

List of Tables

List of Figures

1 Introduction

The aim of particle physics is to answer the questions about the fundamental building blocks of nature. The way to achieve this, is to investigate the elementary particles and their interactions in detail. For this purpose, a probe with the smallest possible wave lengths and thus the highest energies is needed to dissolve the small elementary particles. Such a probe can be an electron or proton which get a high energy at large particle accelerators such as the Tevatron at Fermilab. Then these particles collide and through their high energy new particles with high masses can arise. The study of these new particles and their interaction led to the current understanding of nature which is summarized in the Standard Model of particle physics.

This model reduces the number of elementary particles to twelve which are grouped in three generations. In addition, there are gauge bosons which mediate the forces to build new particles out of the elementary particles and the interactions between them. These interactions are described by four fundamental forces, the electromagnetic, the weak, the strong, and the gravitational force. Although the gravitation is the best known force in every day life, it is the weakest of all the forces and is therefore neglected in the Standard Model. Another macroscopic force is the electromagnetism which describes the interaction between charged particles. The two remaining forces on the other hand interact only at small distances between elementary particles. The strongest force of all, the strong force, is responsible for the visible matter of the universe.

The Standard Model is by far not the final answer to all raised questions. The fact that four different forces exist of which only two, the electromagnetic and the weak force, can be unified in a theoretical approach, sparks speculations for a common formalism for all the observed effects. This unification should culminate in a single theory of everything which would describe all known particles and interactions at all energies and distances. Then, the Standard Model would only be a low energy approximation of a more global theory.

After the top quark was discovered in 1995 by the DØ and CDF collaborations, the three generations in the Standard Model of particle physics were complete. The top quark has by far the largest mass of all fermions, a mass comparable with the mass of a gold atom. A consequence of its high mass is a very short lifetime which allows the top quark to decay before it can hadronize. This makes it different from the other quarks and gives the possibility to study a bare quark. In addition, the high mass leads to speculations that the top quark may play a special role and is a window to new physics. A probe of the Standard Model is the investigation of the $t\bar{t}$ invariant mass distribution where an evidence for $t\bar{t}$ resonances and thus new physics beyond the Standard Model could be found.

In this analysis a search for a narrow-width, heavy vector boson X decaying into

$t\bar{t}$ pairs is presented. The final state depends on the decay channel of the $t\bar{t}$ pair. Only the semileptonic decay channel is used for this analysis. Thus the final state consists of one isolated, high p_T lepton, muon or electron, missing transverse energy ($\not\!\!E_T$) from a neutrino, and four associated jets. The dominant physics background for the resonance signal is $t\bar{t}$ pair production itself and electroweak W boson production accompanied by four or more jets. Instrumental backgrounds for these channels originate from QCD-multijet processes with jets faking isolated leptons. The reduction of the background was improved by identifying b-jets using secondary vertices. The analyzed dataset is approximately $363\,\mathrm{pb}^{-1}$ in the μ+jets channel and $366\,\mathrm{pb}^{-1}$ in the e+jets channel corresponding to data taken from the DØ detector between August 2002 and August 2004.

In chapter two the theoretical aspects relevant for this analysis are presented. First, a short overview of the Standard Model is given and the characteristics of the top quark are described. Then, the possibility of $t\bar{t}$ resonances is introduced and one theoretical model predicting a leptophobic Z' boson decaying to $t\bar{t}$ is discussed in detail since it predicts a large enough cross section for the resonance such that it can be observed or excluded at the Tevatron.

In the next chapter the experimental environment is described. This includes the principle machinery of the Tevatron and the different subsystems of the DØ detector. The algorithms and selection criteria needed to reconstruct and identify the objects produced in the $p\overline{p}$ collisions are presented in chapter four. Details of the selection criteria at trigger level and the actual data sample used in this analysis are presented in the following chapter. The reduction of background events and therefore the enhancement of top like events through trigger selections is necessary since the $t\bar{t}$ production cross section is about ten orders of magnitude smaller than the total inelastic cross section of a $p\overline{p}$ collision. Also in chapter five, the Monte Carlo samples are introduced which are needed to simulate signal and background for this analysis.

In chapter six first the preselection criteria are listed and the thereby resulting efficiency losses are investigated in detail. Then the reconstruction of the $t\bar{t}$ invariant mass through a constraint kinematical fit is discussed and two methods to choose the right solution from this fit are introduced. After taking into account all systematic uncertainties influencing the analysis the final $t\bar{t}$ invariant mass distribution is presented and discussed.

Based on the $t\bar{t}$ invariant mass distribution a search for $t\bar{t}$ resonances is performed and limits on $\sigma_X \times B(X \to t\bar{t})$ for narrow resonances with masses between $350 - 1000$ GeV are given in chapter seven. These obtained limits are then interpreted in a benchmark theoretical model. At the end of this chapter an outlook is given for the expected limits on $t\bar{t}$ resonances until the end of the Tevatron run in 2009.

2 Theoretical Aspects

The Standard Model (SM) of particle physics describes the knowledge of the composition of matter and three out of four of its interactions. Matter is built out of particles which do not show a further underlying structure, the fermions, and the interactions between them are mediated through field carrier particles, the gauge bosons. The Standard Model includes the description of three of the four fundamental forces in nature, the electromagnetism, the weak and the strong force. The gravitation is not explained inside the Standard Model. The gravitational force is extremely small compared to the other three forces and can therefore be neglected in particle physics.

A brief introduction to the Standard Model [1, 2, 3] is given in this chapter, before describing the top quark, its production and decay. One possible theory beyond the SM is discussed in the context of $t\bar{t}$ resonances. Such resonances will be searched for in this analysis.

2.1 The Standard Model

The Standard Model postulates that all matter is built out of 12 point-like and structureless constituents, the fermions. These are 6 quarks, called up, down, charm, strange, top, and bottom, and 6 leptons, the electron and the electron-neutrino, the muon and the muon-neutrino, and the tau and the tau-neutrino, all with a spin of 1/2. Quarks and leptons are grouped in three generations as summarized in Table 2.1.

Each fermion has a corresponding anti-particle with the same mass but opposite charge and is denoted e.g. $\bar{u}$ for the anti-up quark. The three generations have a mass hierarchy, where the first generation has the lightest fermions and the third the heaviest with the top quark being the heaviest of the known particles. The questions why these fermions

	Quarks			Leptons		
Generation	Name	Symbol	Charge [e]	Name	Symbol	Charge [e]
I	up	u	$+\frac{2}{3}$	electron	e^-	-1
I	down	d	$-\frac{1}{3}$	electron-neutrino	ν_e	0
II	charm	c	$+\frac{2}{3}$	muon	μ^-	-1
II	strange	s	$-\frac{1}{3}$	muon-neutrino	ν_μ	0
III	top	t	$+\frac{2}{3}$	tau	τ^-	-1
III	bottom	b	$-\frac{1}{3}$	tau-neutrino	ν_τ	0

Table 2.1: The three generations of quarks and leptons are summarized.

can be grouped as shown and have the mass hierarchy, and if there may exist a fourth generation, are still unanswered.

The interactions between the fermions are due to the exchange of field quanta which mediate the forces described by quantized fields. These field quanta carry spin 1 and are called gauge bosons. The gauge boson responsible for the electromagnetic interaction between charged particles is the massless photon (γ) whereas the weak force is mediated by the massive $W^{\pm}$ and Z^0 bosons. The bosons of the strong force are eight massless gluons (g).

2.1.1 The Strong Interaction

Only quarks participate in the strong interaction while the leptons do not feel this force. The eight gluons mediating the strong force carry a color charge of which three different forms of appearance exist, called "red", "blue", and "green". Quarks carry color, while anti-quarks carry anti-color. The gluons carry non-singlet combinations of color and anti-color. All free compound particles in nature are found to be color neutral. Three quarks which build a baryon carry a different color and for a meson the quark and anti-quark carry a certain color and the corresponding anti-color.

The fact that gluons carry a color charge results in gluon self coupling. This and the non-observation of free color charged particles leads to two important behaviors of the strong interaction: confinement and asymptotic freedom. Confinement describes the fact that quarks at small Q^2, i.e. large distances, can only be found in colorless bound states and not as free particles. This is due to the increase in energy which is stored in the color field when increasing the distance between the quarks. If this energy is sufficiently large additional quark anti-quark pairs are produced in a process called fragmentation and thus neutralizing color. Asymptotic freedom on the other hand allows the quasi-free movement of quarks at small distances.

2.1.2 The Electroweak Interaction and the Higgs Mechanism

The electroweak theory is a unified theory of electromagnetism and the weak force, developed by Glashow, Salam and Weinberg [4, 5, 6]. The weak interaction violates parity which means that left and right handed particles are treated differently. The weak interaction affects only left handed particles or right handed anti-particles. Accordingly, the left handed states of one generation are grouped into weak-isospin doublets and the right handed states form singlets. In the original theory the neutrinos appear only as left handed particles since they were assumed to be massless. However, recent experimental results [7] indicate that neutrinos do have mass and the Standard Model needs to be extended.

To take into account the left and right handiness of particles, the spinor field Ψ can be transformed into left and right handed fields:

$$\Psi_L = \frac{1-\gamma_5}{2}\Psi \text{ and } \Psi_R = \frac{1+\gamma_5}{2}\Psi \tag{2.1}$$

This theory includes four gauge fields, one triplet (W_μ^1, W_μ^2, W_μ^3) and one singlet (B_μ). The fields of the electroweak bosons ($W^\pm$, Z^0, γ) are mixtures of these gauge fields where $W_\mu^\pm$, Z_μ, and the photon field A_μ can be written as

$$W_\mu^\pm = \frac{1}{\sqrt{2}}(W_\mu^1 \mp i\, W_\mu^2) \tag{2.2}$$

$$\begin{pmatrix} A_\mu \\ Z_\mu \end{pmatrix} = \begin{pmatrix} \cos\theta_W & \sin\theta_W \\ -\sin\theta_W & \cos\theta_W \end{pmatrix} \begin{pmatrix} B_\mu \\ W_\mu^3 \end{pmatrix} \tag{2.3}$$

The mixing angle θ_W is the Weinberg angle. The theory so far leads only to massless gauge bosons, however the $W^\pm$ boson has a mass of $m_W = (80.425 \pm 0.038)$ GeV [8], and the Z^0 of $m_Z = (91.1876 \pm 0.0021)$ GeV [8]. To give the gauge bosons a mass, a scalar isospin doublet Φ

$$\Phi = \begin{pmatrix} \Phi_1 + i\Phi_2 \\ \Phi_3 + i\Phi_4 \end{pmatrix} \tag{2.4}$$

was introduced by Higgs [9] which couples to the gauge bosons. The scalar potential V takes the form:

$$V(\Phi) = \mu^2 \Phi^\dagger \Phi + \lambda(\Phi^\dagger \Phi)^2 \ , \tag{2.5}$$

with the parameters $\mu^2 < 0$ and $\lambda > 0$ which were chosen such that the vacuum expectation value v of the Higgs potential V is $v = \sqrt{-\mu^2/\lambda}$ and thus not zero. v is the ground state of the system and if it is non-zero the symmetry is broken, which is then called spontaneous symmetry breaking. The masses of the gauge bosons are then given by

$$m_W = \frac{1}{2} v g \tag{2.6}$$

$$m_Z = \frac{1}{2} v \sqrt{g^2 + g'^2} \tag{2.7}$$

$$m_\gamma = 0 \tag{2.8}$$

where g is the coupling constant of the weak and g' the coupling constant of the electromagnetic interaction.

The Higgs mechanism also predicts the neutral Higgs boson h with spin zero and a mass of $m_h = v\sqrt{2\lambda}$. While the vacuum expectation value can be calculated from the Fermi coupling constant G_F [8] to be $v \simeq 246$ GeV, λ is a free parameter. Therefore, the mass of the Higgs boson needs also to be measured. Whereas the Higgs boson has not been found to date, a direct search in e^+e^- annihilations set a mass limit of $m_h > 114.4$ GeV [10].

The charged weak interaction is able to change a member of an isospin doublet to the corresponding partner within one generation. In this case the lighter quark in each generation would be stable, like the neutrino is in the lepton doublets. However, there are no stable particles found in nature which contain s or b quarks; the s quark decays in d quarks instead. This can be explained through the fact that the weak eigenstates do not coincide with the mass eigenstates. It is possible to set weak and mass eigenstates

equal for up-type quarks (u, c, t), which then leaves the transformation from mass to weak eigenstates entirely to the down-type quarks (d, s, b):

$$\begin{pmatrix} d' \\ s' \\ b' \end{pmatrix} = \begin{pmatrix} V_{ud} & V_{us} & V_{ub} \\ V_{cd} & V_{cs} & V_{cb} \\ V_{td} & V_{ts} & V_{tb} \end{pmatrix} \begin{pmatrix} d \\ s \\ b \end{pmatrix} \tag{2.9}$$

where d', s' and b' are the weak eigenstates. This matrix is called the Cabbibo–Kobayashi–Maskawa (CKM) matrix [11].

2.2 The top Quark

After the b quark was discovered in 1977, the top quark was predicted as its electroweak isospin partner. It took 18 years to discover the top quark in 1995 at the Tevatron which then completed the quark sector of the three generations in the Standard Model. With a measured mass of $m_t = 172.7 \pm 2.9$ GeV [12] which is the current world average, it has by far the largest mass of all the known elementary particles in the Standard Model and is as heavy as a gold atom. The lifetime of a top quark is extremely short such that it decays before it can form hadronic bound states.

2.2.1 Top Quark Production

The center-of-mass energy at a particle accelerator needs to be at least twice as large as the mass of the top quark for the production of top anti-top quark pairs. To date this is only possible in $p\bar{p}$ collisions at the Tevatron, running at a center-of-mass energy of $\sqrt{s} = 1.96$ TeV, in the future pp collisions at the Large Hadron Collider (LHC) at $\sqrt{s} = 14$ TeV and e^+e^- collisions at a planned International Linear Collider (ILC) will also produce top quarks.

The top quark can be produced in a $t\bar{t}$ pair where this process is dominated by the strong interaction, and singly due to electroweak interactions. For the $t\bar{t}$ production the Feynman diagrams for the two contributing subprocesses, quark anti-quark annihilation and gluon fusion are shown in Fig. 2.1. At the Tevatron the quark anti-quark annihilation dominates whereas at the LHC $t\bar{t}$ pairs will be generated mostly through gluon fusion.

This can be explained by looking at the parton-model of the $t\bar{t}$ pair production. Protons are a collection of quarks, anti-quarks, and gluons (together called partons) where each parton carries some fraction x of the proton's four momenta. The typical value of x for $t\bar{t}$ production is

$$x \approx \frac{2m_t}{\sqrt{s}} \ . \tag{2.10}$$

The relative contributions in the $t\bar{t}$ pair production from the two processes of quark anti-quark annihilation and gluon fusion depend on this value of x and the parton distribution functions (PDF). For the Tevatron at $\sqrt{s} = 1.96$ TeV the fraction x is $x \approx 0.18$, whereas at the LHC the typical value of x is $x \approx 0.025$. When comparing the PDFs for quarks

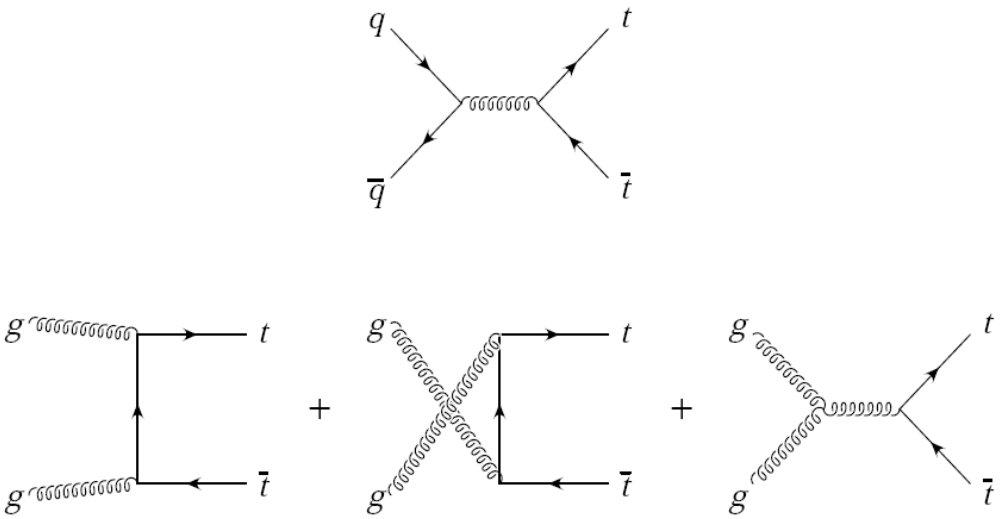

Figure 2.1: Feynman diagrams for the $t\bar{t}$ production through quark anti-quark annihilation (upper diagram) and gluon fusion (lower diagrams). [13]

and gluons, as shown in Fig. 2.2, for the two different values of x it can clearly be seen that quarks dominate at rather large values of x such that quark anti-quark annihilation dominates at the Tevatron with a contribution of 85% to the total cross section. In contrast, for $x \approx 0.025$ at the LHC the gluon distribution function is much larger than those of the quarks which leads to a 90% domination of gluon fusion at the LHC.

The predicted cross-section at next to leading order [14] for $\sqrt{s} = 1.96$ TeV at the Tevatron and an assumed top quark mass of $m_t = 175$ GeV is calculated to be

$$\sigma_{t\bar{t}} = 6.77 \pm 0.42\,\text{pb}. \tag{2.11}$$

There are two processes to produce single top quarks via the weak interaction at the Tevatron, as shown generically in Fig. 2.3. In the first process the single top quark is produced in association with a b quark by the exchange of a s-channel W boson, whereas a t-channel W boson is exchanged in the second process. The b quark in the initial state of the t-channel is produced through gluon splitting resulting in an additional b quark in the final state. A third possibility to produce a single top quark is in association with a real W boson, but this production mechanism will not be observable at the Tevatron due to a low cross section. The s- and t-channel processes on the other hand, although not yet been observed, should be seen for the first time at the Tevatron. The theoretical predictions for the cross sections of the s- and t-channel at the Tevatron in next to leading order are [15, 16, 17, 18]:

$$\sigma_s = 0.88 \pm 0.14\,\text{pb} \tag{2.12}$$

$$\sigma_t = 1.98 \pm 0.30\,\text{pb} \tag{2.13}$$

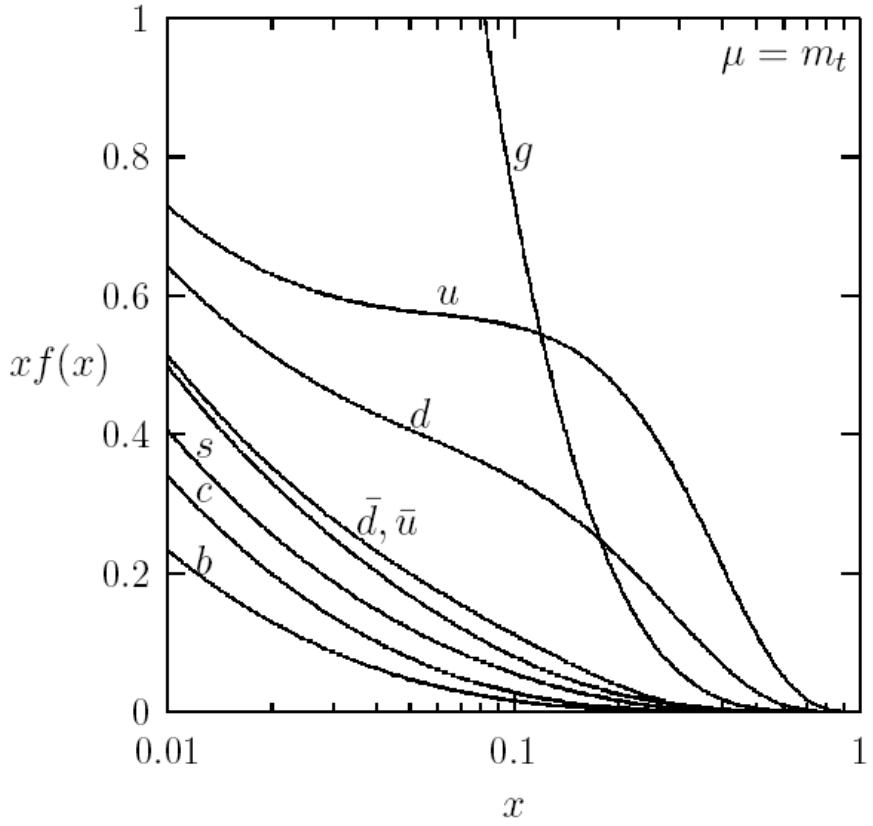

Figure 2.2: The parton distribution functions for different partons at the scale $\mu = m_t$, relevant for top quark production. [13]

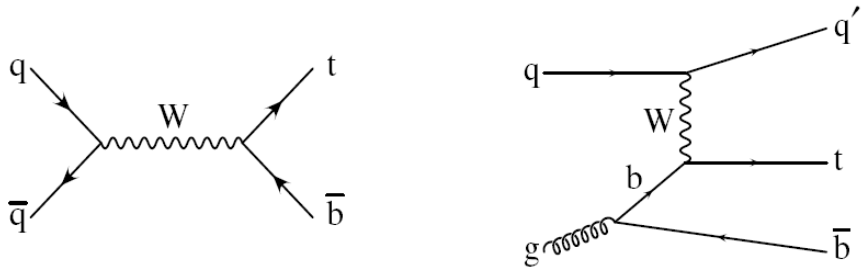

Figure 2.3: Single top quark production via the weak interaction. The left diagram corresponds to the s-channel, the right to the t-channel process. [17]

2.2.2 Top Quark Decay

A consequence of the high mass of the top quark is its total decay width of $\Gamma_t \approx 1.5$ GeV, which corresponds to an extremely short lifetime of about $5 \cdot 10^{-25}$ s. Thus, the top quark decays before it can hadronize. This is a unique property of the top quark since all the other quarks hadronize before they can decay.

The transition probability of a top quark to a b quark is proportional to $|V_{tb}|^2$. In the case of only three generations in the Standard Model, V_{tb} as given by the CKM matrix is constraint to be $|V_{tb}| \approx 0.999$, and since the top quark decay is described by the weak interaction, a top quark decays almost always into a W boson and a b quark. After a $t\bar{t}$ pair has been produced it decays into two b quarks and two W bosons. The experimentally observed signatures depend on the decay of the two W bosons. Three different decay channels can be classified:

- **The alljets channel** where both W bosons decay hadronically into two quarks each is characterized by six jets in the final state, two of which are coming from b quarks. Although this channel has the highest branching ratio of about 46% and allows for the full reconstruction of the event kinematics, it is difficult to separate from the overwhelming multijet background.

- **The dilepton channel** where both W bosons decay leptonically into a charged lepton and a corresponding neutrino has the cleanest signal structure, since it provides a very good separation from the background. Unfortunately, this channel not only suffers from low statistics due to a small branching fraction of 9%, but also does not allow a kinematic reconstruction of the event due to two unmeasured neutrinos.

- **The lepton+jets channel** where one W boson decays hadronically into two quarks and the other leptonically into a charged lepton and a neutrino is the one with a high branching fraction of 45% on one hand and a good separation from background on the other. In principle all three charged leptons contribute to this channel, but usually only the electron and muon channels are considered when referring to the lepton+jets (l+jets) channel. Also in this analysis, which is carried out in the l+jets channel, only the e+jets and the μ+jets channel are considered. The τ lepton has to be treated separately since it can decay leptonically into an electron or muon, or hadronically into pions. In the case of a leptonically τ decay, this event will appear in the electron/muon+jets channels, whereas a hadronically decaying τ is a major challenge to reconstruct at hadron collider and is not considered in this analysis.

The decay channels with their corresponding branching ratios are summarized in Fig. 2.4.

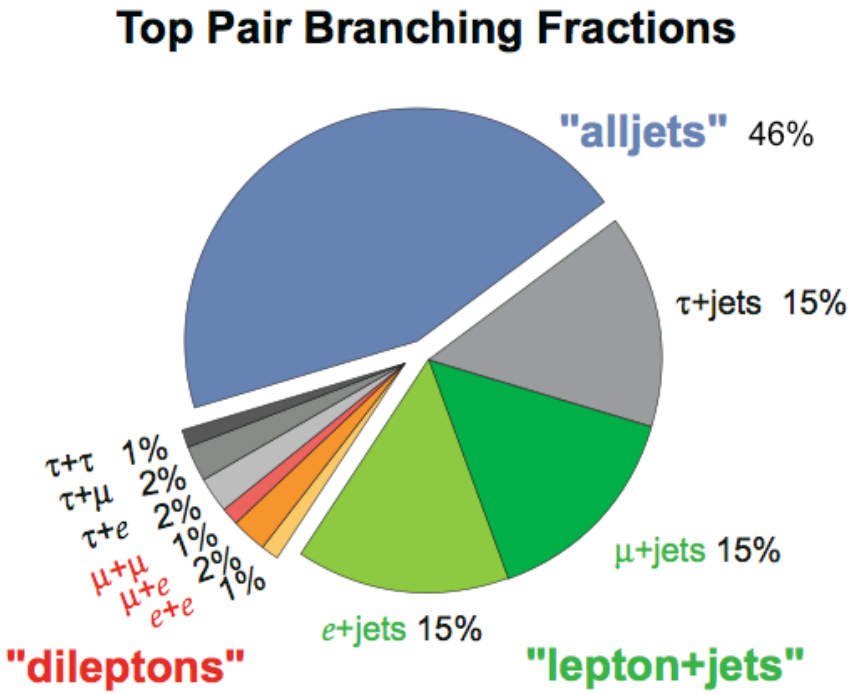

Figure 2.4: $t\bar{t}$ decay channels with their branching ratios. [19]

2.2.3 The Top Quark and the Higgs Boson

In Sect.2.1.2 the mass of the W boson was defined only through the vacuum expectation value of the Higgs field, v and the gauge coupling g. In lowest order, i.e. tree level, v and g can be determined by α, the fine-structure constant and G_F, the Fermi coupling constant such that the W boson mass can be calculated as

$$m_W^2 = \frac{1}{2} m_Z^2 \left(1 + \sqrt{1 - \frac{4\pi\alpha}{\sqrt{2} G_F m_Z^2}} \right) = \frac{\frac{\pi\alpha}{\sqrt{2}G_F}}{\sin^2 \theta_W} \quad . \tag{2.14}$$

In addition, higher order loop diagrams contribute to the W mass which contain virtual top quarks and virtual Higgs bosons. If these corrections are considered, the W boson mass can be written as

$$m_W^2 = \frac{\frac{\pi\alpha}{\sqrt{2}G_F}}{\sin^2 \theta_W (1 - \Delta r)} \quad . \tag{2.15}$$

Δr is a correction due to one-loop processes where both, the top quark and the Higgs boson contribute to. The correction from virtual top quark loops is given by

$$(\Delta r)_t \approx - \frac{3 G_F}{8\sqrt{2}\pi^2 \tan^2 \theta_W} \cdot m_t^2 \quad , \tag{2.16}$$

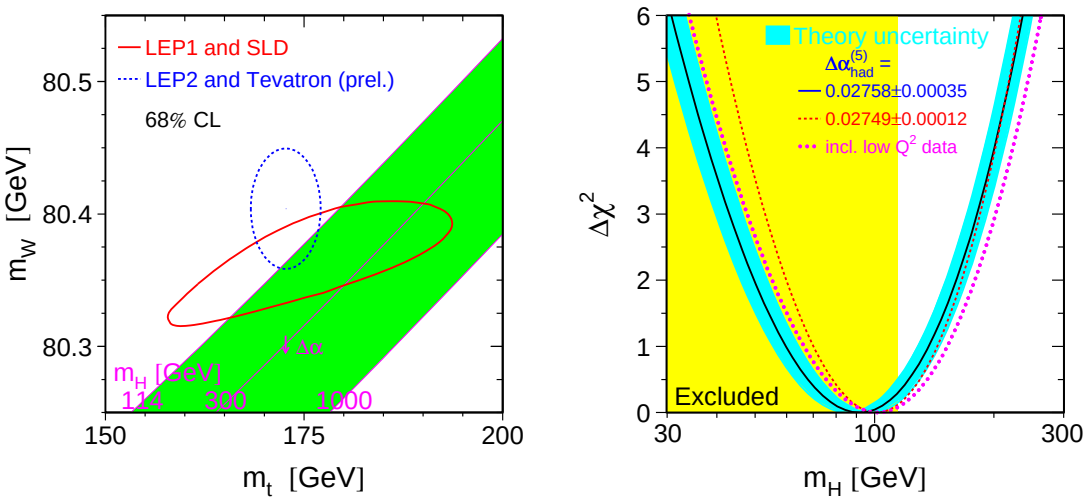

Figure 2.5: On the left contour curves in the (m_t, m_W) plane in a global fit to the electroweak data. Also shown is the correlation between m_t and m_W as expected in the Standard Model for different Higgs boson masses. On the right the indirect measurement of the Higgs boson mass together with the lower limit at 95% confidence level on the Higgs boson mass. [20]

and the contribution from the virtual Higgs boson loop is

$$(\Delta r)_h \approx -\frac{11 G_F m_Z^2 \cos^2\theta_W}{24\sqrt{2}\pi^2} \cdot \ln\frac{m_h^2}{m_Z^2} \quad . \tag{2.17}$$

As can be seen, the mass of the W boson is related to both the mass of the top quark and the mass of the Higgs boson. The dependence is stronger for the top quark since its mass enter quadratically while the mass of the Higgs boson enters only logarithmically. A consequence of these mass relations is an indirect measurement of the SM Higgs boson mass from a fit to electroweak data, as can be seen in Fig. 2.5. The precision of the direct mass measurements of the W boson and the top quark result in a better indirect limit on the Higgs boson mass.

2.3 $t\bar{t}$ Resonances

In the Standard Model no $t\bar{t}$ bound states are expected since the lifetime of the top quark is considerably shorter than the typical timescale of the strong interaction. The only possibility of resonant production of a $t\bar{t}$ pair in the Standard Model is through the decay of the Higgs boson. This is only possible for a heavy Higgs boson with a mass of at least about 350 GeV, i.e. twice the top quark mass. In this case the branching ratio for e.g. a 400 GeV Higgs decaying to $t\bar{t}$ is only of the order of 14% [21]. With

an expected cross section at the Tevatron for a heavy Higgs production through gluon fusion of below 0.1 pb [22] such a $t\bar{t}$ resonance cannot be observed. Apart from this, indirect measurements of the Higgs boson mass from electroweak data indicate a light Higgs boson, as can be seen in Fig. 2.5, thus making a Standard Model Higgs boson decaying to $t\bar{t}$ unlikely.

The top quark properties like its heavy mass and short lifetime are very different from the ones of the lighter quarks. Especially the top mass which is of the order of the electroweak symmetry breaking scale has lead to speculations that it may play a special role for new physics [23]. Therefore, probing the Standard Model properties of the top quark opens a window to new physics. Such a probe is the measurement of the $t\bar{t}$ invariant mass distribution where a deviation from the Standard Model expectation especially in form of a peak structure would hint to a high mass resonance and therefore to new physics.

At the LHC where gluon fusion reigns, a spin zero resonance could manifest itself as a peak-dip structure in the $t\bar{t}$ differential cross section, as well as in the invariant mass distribution. This is due to a possible interference of the production of any spin zero resonance X through $gg \to X \to t\bar{t}$ with the non-resonant $t\bar{t}$ production $gg \to t\bar{t}$. This interference produces at the parton level a peak-dip structure in the cross section [24] in the vicinity of the resonance mass. The production of a spin one resonance at the LHC is only possible through quark anti-quark annihilation since the production mechanism through $gg \to X \to t\bar{t}$ is forbidden by Yang's theorem [25]. Due to the fact that any resonance produced by quark anti-quark annihilation does not interfere with the continuum production, no interference effects will emerge for spin one resonances.

At the Tevatron $t\bar{t}$ is produced predominantly through quark anti-quark annihilation where no interference effects are produced. In the comparably small fraction of production through gluon fusion an interference would only show up for a spin zero resonance. In this case any interference structure would be buried beneath the $q\bar{q} \to t\bar{t}$ continuum. Thus, the peak-dip structure from the interference can be neglected at the Tevatron.

In this work it is only searched for a clear peak signal on top of the $t\bar{t}$ invariant mass spectrum. Such a signal can best be seen if the width of the resonance is smaller than the detector resolution, since otherwise the resonance is too broad to be discriminated from the non-resonant background. Therefore only a search for a narrow width resonance with $\Gamma_X = 0.012 M_X$ will be performed in this analysis.

There are several models which have been proposed for extensions of the Standard Model which could produce resonances in the $t\bar{t}$ invariant mass spectrum [26, 27, 28, 29]. A color-octet vector meson associated with a top condensate [30] and multiscale technicolor [31, 32] are two examples of theoretical models which could lead to an enhanced $t\bar{t}$ production. Although a heavy Higgs boson with a large branching ratio for the decay into $t\bar{t}$ is unlikely in the Standard Model scenario, such a Higgs boson is predicted in the Minimal Supersymmetric Standard Model (MSSM) [33] for the proper choice of parameters.

2.3.1 Leptophobic Z' decaying to $t\bar{t}$

One theoretical model beyond the Standard Model which predicts a $t\bar{t}$ resonance in terms of a leptophobic new gauge boson, Z', with a large enough predicted cross section such that it can be observed or excluded at the Tevatron, is topcolor assisted technicolor. The basic ideas leading to this theory and the predicted cross section in a specific model for the leptophobic Z' will be introduced in the following. The Standard Model explains the masses of quarks and charged leptons by a coupling to the Higgs field, but does not give a dynamical explanation for the mass hierarchy in the different generations. To give a possible explanation, a new theoretical model was introduced, called "technicolor" [34, 35, 36, 37, 38]. It provides a dynamical description of electroweak symmetry breaking by introducing a new strong force which is analogous to the strong color force. In this model new particles are predicted where each Standard Model particle gets its corresponding techniparticle. The electroweak symmetry breaking is then described through the condensation of techniquarks at the technicolor scale of $\Lambda_{TC} \sim 1$ TeV.

Unfortunately, technicolor as such does not address the flavor problem. Therefore, it needed to be extended via another new broken gauge interaction which gives the quarks and leptons their masses. To avoid flavor changing neutral currents also additional extensions to the basic idea have to be introduced. In the new framework, the "extended technicolor" (ETC), in particular with a slowly running ("walking") coupling, the existence of massive vector gauge bosons is predicted which mediate the interaction between fermions and technifermions and generate the fermion masses. Since the masses of the fermions in the three generations range from very few MeV to $\sim$ 175 GeV, a whole spectrum of ETC vector gauge bosons with different masses, one for each fermion, seem to be necessary. Through this mechanism the masses of all fermions but the top quark can be generated.

A theoretical model which could explain the large top mass is based on a new interaction of the third generation quarks, which is called "topcolor" [39]. This interaction should be a minimal dynamical scheme to reproduce the Higgs mechanism and explain the large mass of the top quark. Topcolor can generate a large top quark mass through the formation of a dynamical $t\bar{t}$ condensate, generated by a new strong gauge force, coupling preferentially to the third generation. By itself, topcolor could explain the top quark mass but if the condensates were required to account for all of the electroweak symmetry breaking the resulting fermion masses would be quite large, $\sim$ 600 GeV. To correct for this an excessive fine-tuning would be needed which seems unnatural.

These two theoretical models, the extended technicolor, describing a mechanism for electroweak symmetry breaking, and topcolor, explaining the large top quark mass, were combined in one theory called "topcolor assisted technicolor" (TC2). In TC2 the technicolor interactions cause electroweak symmetry breaking and the combination of ETC with the "walking" coupling can generate the masses of all fermions but the top quark. The topcolor interactions induce a massive dynamical $t\bar{t}$ condensate which gives the large top quark mass. In the TC2 theory massive gauge bosons, a color octet of "colorons" and a color singlet Z', are predicted.

In one particular scenario of topcolor-assisted technicolor [40], Z' couples weakly and

$M_{Z'}$ [GeV]	$\sigma(p\bar{p} \to Z' \to t\bar{t})$ [pb]
400	13.16
450	8.98
500	5.67
550	3.42
600	2.12
650	1.32
750	0.49
850	0.18
1000	0.04

Table 2.2: The theoretically predicted $\sigma_{Z'} \times B(Z' \to t\bar{t})$ for $Z' \to t\bar{t}$ with a width of $\Gamma_{Z'} = 0.012 M_{Z'}$ calculated for the CTEQ5L parton distribution functions.

symmetrically to the first and second generations and strongly to the third generation of quarks, and has no couplings to leptons. Thus, it is called leptophobic. In order to provide a large top quark mass and to ensure that the b quark is light, a "tilting" mechanism is required. This tilting mechanism enhances the formation of the $t\bar{t}$ condensate, while the formation of the $b\bar{b}$ condensate is blocked. Therefore, the resulting predicted cross section for $t\bar{t}$ production is larger than the Standard Model prediction.

The total predicted cross section for $t\bar{t}$ production via the process $p\bar{p} \to Z' \to t\bar{t}$ is given by:

$$\sigma = \int_{m_0}^{\sqrt{s}} \mathrm{d}m \frac{2}{m} \int_{-\ln(\sqrt{s}/m)}^{\ln(\sqrt{s}/m)} \mathrm{d}y_b x_p x_{\bar{p}} \sum_q \left[\mathcal{L}(x_p, x_{\bar{p}}) \hat{\sigma}(p\bar{p} \to Z' \to t\bar{t})\right] \ , \tag{2.18}$$

where x_p ($x_{\bar{p}}$) is the initial parton fractional momenta inside the proton (anti-proton), and m_0 is the $t\bar{t}$ threshold mass ($2m_t$). The boost of the partonic system y_b is given by $y_b = (1/2)\ln(x_p/x_{\bar{p}})$. The partonic "luminosity function", summed over all quark and anti-quark combinations from the parent particles, is the product of the parton distribution functions $q(x,\mu)$ ($\bar{q}(x,\mu)$) of a quark (anti-quark) evaluated at fractional momenta x and renormalization scale μ:

$$\mathcal{L}(x_p, x_{\bar{p}}) = q(x_p,\mu)\bar{q}(x_{\bar{p}},\mu) + \bar{q}(x_p,\mu)q(x_{\bar{p}},\mu) \tag{2.19}$$

In the narrow width approximation and assuming no interference between $\gamma/Z^0/Z'$, the parton level subprocess cross section $\hat{\sigma}$ can be written as [40]:

$$\begin{aligned}
\hat{\sigma}(p\bar{p} \to Z' \to t\bar{t}) \ &= \ \frac{\alpha^2\,\pi}{64\cos^4\theta_W} \cot^4\theta_H \\
&\times (2 \text{ for initial state } u+\bar{u};\ (1) \text{ for initial state } d+\bar{d}) \\
&\times \left[\beta\,(1+\frac{1}{3}\beta) \times (\beta\,(1-\beta^2)+2)\right] \\
&\times \left[\frac{\hat{s}}{(\hat{s}-M_{Z'}^2)^2 + \hat{s}\,\Gamma_{Z'}^2}\right] \times \theta\,(\hat{s}-4m_t^2) \ ,
\end{aligned} \tag{2.20}$$

where $\sqrt{\hat{s}}$ is the partonic center-of-mass energy which is equal to the $t\bar{t}$ invariant mass m. β is the p/E ratio for the top quark $\beta = \sqrt{1 - \frac{4m_t^2}{M_{Z'}^2}}$. The mixing angle $\cot^2\theta_H$ is a parameter of the topcolor model and is related to the total decay width $\Gamma_{Z'}$ of Z' as:

$$\Gamma_{Z'} = \frac{\alpha \cot^2\theta_H M_{Z'}}{8\cos^2\theta_W}\left[\sqrt{1-\frac{4m_t^2}{M_{Z'}^2}}\,(2-5\frac{m_t^2}{M_{Z'}^2})+4\right] \tag{2.21}$$

With these formulae, the theoretically predicted cross section for a Z' resonance decaying in $t\bar{t}$ has been calculated. To qualify as a narrow resonance, a width of $\Gamma_{Z'} = 0.012 M_{Z'}$ was chosen since this value is smaller than the mass resolution of the DØ detector. In Table 2.2, this can be found for different resonance masses, all with a width of $\Gamma_{Z'} = 0.012 M_{Z'}$ and calculated for the CTEQ5L parton distribution functions.

3 Tevatron and the DØ Detector

The Tevatron accelerator at Fermilab produces proton-antiproton ($p\bar{p}$) collisions at the currently highest center-of-mass energy of $\sqrt{s} = 1.96$ TeV. It is the world's only facility to produce the top quark and will remain in this position until the Large Hadron Collider (LHC) will start producing pp collisions in 2007 at a significantly higher center-of-mass energy of $\sqrt{s} = 14$ TeV. Two collider experiments are located at the Tevatron accelerator: the Collider Detector at Fermilab (CDF) and DØ.

Between 1991 and 1995, in the first data taking period (Run I) at an energy of $\sqrt{s} = 1.8$ TeV, each experiment collected about 125 pb^{-1} of data. In Run I the first top-quarks were discovered and measurements of their production and properties were performed. After 1995 the accelerator was upgraded to a center-of-mass energy of $\sqrt{s} = 1.96$ TeV and the new data taking period (Run II) started in 2001 and will go on until 2009. The Tevatron machine accelerates 36 bunches of protons and anti-protons which leads to a time between bunch crossings of 396 ns. As a consequence the detector systems to record the data and the detector components themselves have to be sophisticated to ensure fast enough response time. In addition, the detector components needed a sophisticated design to measure the emerging particles precisely.

3.1 The Tevatron Accelerator

Before the protons and anti-protons can collide in the CDF and DØ detectors, they first have to be produced and then accelerated through a series of accelerators. The accelerator chain which the protons and anti-protons have to travel through, is shown in Fig. 3.1.

The first accelerator is the Cockcroft-Walton pre-accelerator where negatively charged hydrogen ions are produced. Hydrogen gas is converted into ionized hydrogen gas (H^-) which is then accelerated through a potential to an energy of 750 keV. Then the H^- ions are transfered into the Linear Accelerator or "Linac" where they are accelerated to 400 MeV. An oscillating electric field in the radio frequency (RF) cavities of the Linac accelerates the ions and groups them into bunches. After that the ions are injected into the Booster, a circular accelerator, or synchrotron, with a 75 m radius. There the electrons are stripped off and the remaining protons are then accelerated to 8 GeV.

The Main Injector (MI) is a circular synchrotron seven times the circumference of the Booster and accelerates protons from the Booster to either 120 GeV or 150 GeV, depending on their destination. When the injected protons are used to produce anti-protons, the final beam energy is 120 GeV. Then, the proton beam is sent towards the Anti-proton Source where it strikes a nickel target. A spray of all sorts of secondary

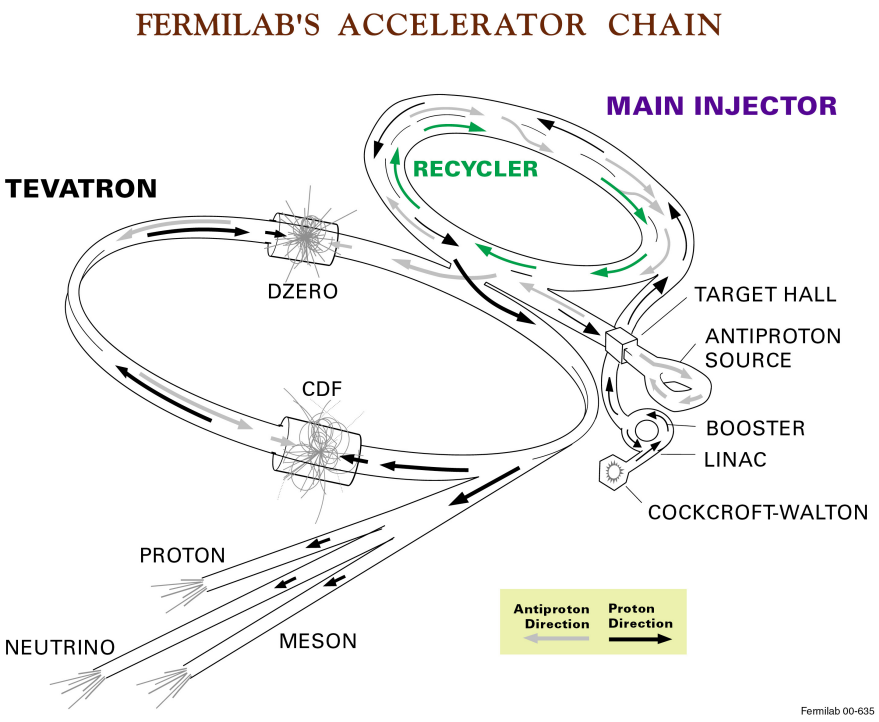

Figure 3.1: The Fermilab accelerator chain. [41]

particles is produced and magnets are used to collect 8 GeV anti-protons according to their momentum and charge from this. These anti-protons are sent to the Debuncher where the high momentum spread anti-protons are captured and a beam with a constant energy of 8 GeV is maintained. In addition, the beam is "cooled", i.e. the particle density in the beam is increased by reducing the physical size and energy spread of the beam. After that the anti-protons are transferred to the Accumulator where all of the produced anti-protons are stored at 8 GeV and cooled until needed. Another anti-proton storage ring is the Recycler which is housed in the same tunnel as the Main Injector, where remaining anti-protons from preceding Tevatron collisions are cooled and stored alongside those sent from the antiproton source.

Once enough anti-protons are produced they are transfered to the Main Injector and both, protons and anti-protons are accelerated to 150 GeV, before being injected into the Tevatron. Such an injection contains 36 bunches, with a proton bunch containing around $3 \cdot 10^{11}$ protons, whereas an anti-proton bunch contains only around $3 \cdot 10^{10}$ anti-protons.

The last and largest accelerator is the Tevatron with a circumference of about 6 km. Protons and anti-protons are injected at 150 GeV and then accelerated to 980 GeV. Once a stable situation is achieved, the two counter-rotating beams collide at the two collision points where the DØ and CDF detectors are located. A detailed description, including technical details can be found in Ref. [42]. The luminosity is given by:

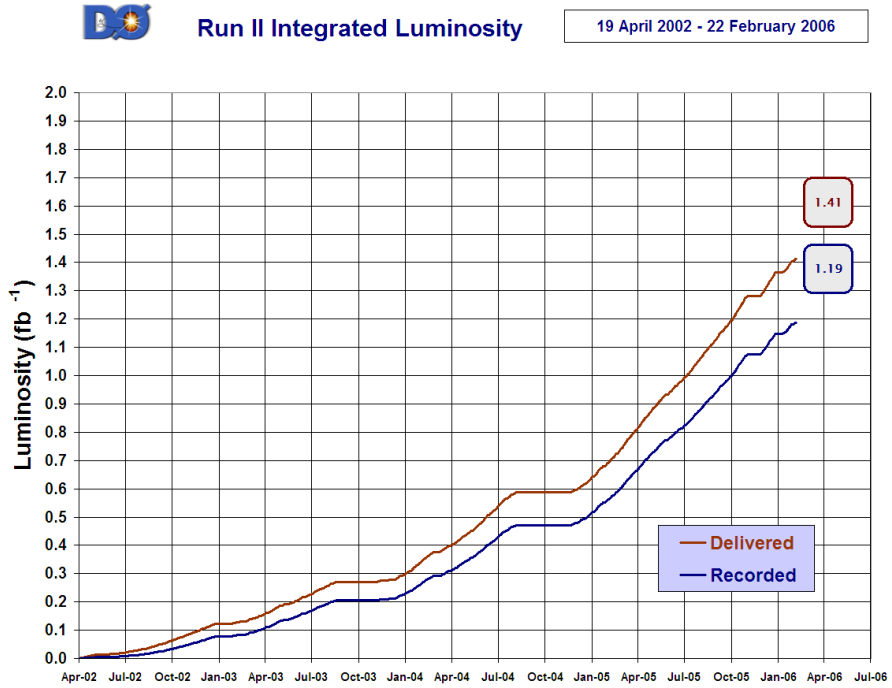

Figure 3.2: The integrated luminosity delivered to and recorded with the DØ detector in Run II until end of February 2006. [44]

$$\mathcal{L} = \frac{fBN_pN_{\bar{p}}}{2\pi(\sigma_p^2 + \sigma_{\bar{p}}^2)} F(\sigma_l/\beta^*) \tag{3.1}$$

where f is the revolution frequency, B the number of bunches in each beam, N_p ($N_{\bar{p}}$) is the number of protons (anti-protons) in a bunch, σ_p ($\sigma_{\bar{p}}$) is the root mean square (RMS) proton (anti-proton) beam size at the interaction point, and F is a form factor that depends on the ratio of the bunch length σ_l to the beta function at the interaction point, as defined in Ref. [43]. In Figure 3.2 the integrated luminosity of the Tevatron is shown which was delivered to and recorded with the DØ detector in Run II until the end of February 2006.

3.2 The DØ Detector

The DØ detector is a multipurpose detector designed to detect particles created in $p\bar{p}$ collisions of the Tevatron and to cover a broad spectrum of physics processes. An overview of the DØ detector and all of its subdetector systems is given in Fig. 3.3.

The subdetectors are arranged symmetrically around the beam pipe where the $p\bar{p}$ collisions take place. The innermost part is the tracking system, followed by the calorimeter and the outermost subdetector is the muon system. All informations concerning the DØ detector given in this chapter and many more details can be found in Ref. [45].

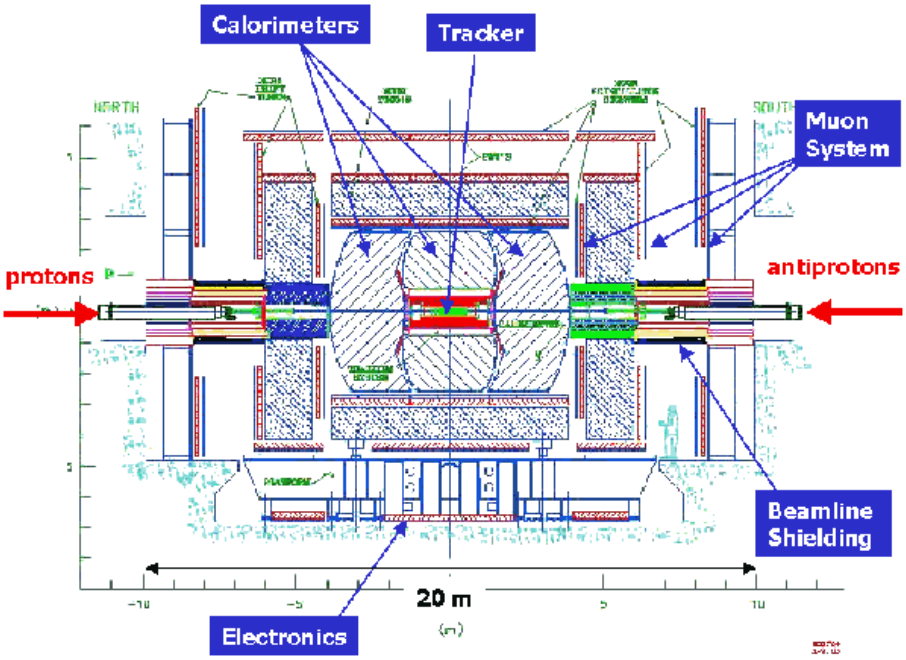

Figure 3.3: Overview of the DØ detector. [45]

3.2.1 The DØ Coordinate System

The DØ coordinate system is right-handed with the origin at the center of the detector. The positive z axis is along the beam pipe in direction of the proton beam and the y axis points upwards. As a consequence the x axis points towards the center of the Tevatron ring. The "transverse plane" is the plane perpendicular to the beam. In $p\bar{p}$ collisions the total center-of-mass energy of the $p\bar{p}$ system is not conserved since many of the produced particles escape down the beam pipe. Also, the energy fraction of the colliding proton and anti-proton is not known. As a result, the center-of-mass system of the parton collision is boosted along the beam direction by an unknown amount. Quantities defined in the transverse plane such as the transverse momenta of particles are conserved in the collision: $\Sigma\vec{p}_T = 0$. In the transverse plane cylindrical coordinates (r, ϕ) are often used, due to the fact that the physics processes are symmetric in ϕ which also explains the cylindrical structure of the detector. Instead of using the polar angle θ to describe the angle between the z axis and the momentum of the particle, the pseudo-rapidity η

$$\eta = -\ln \tan(\theta/2) \tag{3.2}$$

is used. The spatial separation between two objects which is invariant under Lorentz transformation is defined as

$$\Delta R = \sqrt{(\eta_1 - \eta_2)^2 + (\phi_1 - \phi_2)^2} = \sqrt{\Delta\eta^2 + \Delta\phi^2}. \tag{3.3}$$

3.2.2 The Tracking System

A good tracking system is needed to study many important physics topics such as the top-quark, the search for new phenomena and many more, since they all rely on the determination of the primary interaction vertex. The informations obtained from the tracking system allow for a b-jet identification, which is a necessary part in this analysis.

The central tracking system consists of the silicon microstrip tracker (SMT) and the central fiber tracker (CFT) surrounded by a solenoidal magnet. This superconducting solenoidal magnet has a nearly uniform magnetic field of 2 T parallel to the beam axis. Charged particles passing through the magnetic field are bent around the field lines and the curvature allows for a measurement of the transverse momentum. A schematic view of the central tracking system is shown in Fig. 3.4.

The Silicon Microstrip Tracker

The Silicon Microstrip Tracker is the innermost tracking detector and makes a precise measurement of the three dimensional trajectories of the charged particles. The SMT provides tracking information over a large η range, which is also necessary for vertexing. This is realized by designing barrel modules interspersed with disks for the low η region around $z = 0$ and disks only in the forward regions with large $|\eta|$. The barrel detectors measure primarily the $r-\phi$ coordinate while the disks also measure the $r-z$ coordinate. An isometric view of the SMT is shown in Fig. 3.5.

The detector has six barrels in the central regions and each barrel is capped at the high $|z|$ end with a disk, a so called "F-disk". In addition three F-disk are placed at the ends of the outermost barrels. At the far forward region two large-diameter disks ("H-disks") complete the SMT. All disks and also the four layers each barrel consists

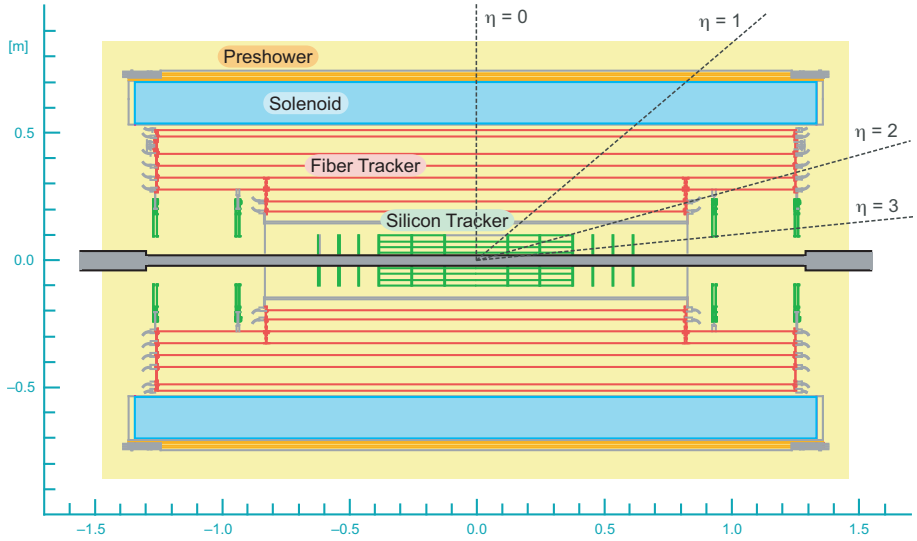

Figure 3.4: Schematic view of the central tracking system in the $y-z$ plane.

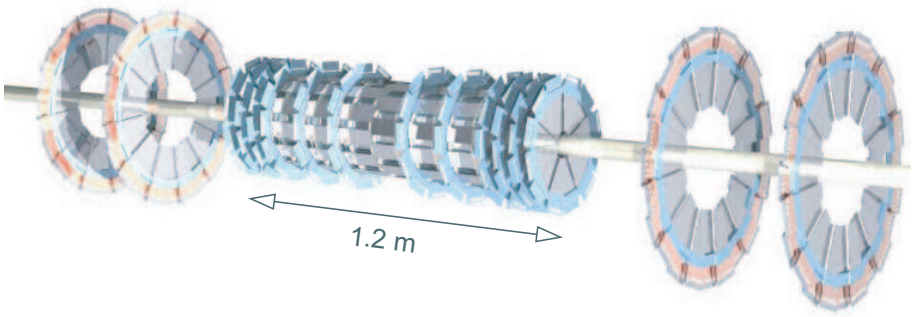

Figure 3.5: The disk/barrel design of the SMT. [45]

of, are equipped with 300 μm thick semiconducting silicon sensors which are segmented into strips. This leads to a total of about 800000 read-out channels.

When a charged particle passes through these sensors electron-hole pairs are produced. The electrons drift towards the anode and the holes towards the cathode where the charge is collected. The charge is read out separately for each strip. Since parts of the sensors are double-sided stereo sensors where the strips at one side are at a 2° angle with respect to the other, a measurement in two dimensions is possible. The SMT provides a resolution of approximately 10 μm.

The Central Fiber Tracker

The CFT is built out of scintillating fibers with a diameter of 835 μm and surrounds the silicon detector. In addition to the measurement of the p_T of particles, the CFT also provides fast track triggering for Level 1. It consists of eight support cylinders on each of which two double-layers of fibers are mounted. One of these two layers is oriented along the beam direction and the other one at a stereo angle in ϕ of $\pm 3°$. When a charged particle passes through one of the fibers, the scintillator emits light. This light is transported through waveguides, which are coupled to the scintillating fibers, to visible light photon counters for read-out. The CFT gives a resolution of about 100 μm.

The Preshower Detectors CPS and FPS

The preshower detectors are two additional tracking detectors outside the magnetic field. The central preshower detector CPS is mounted on the solenoid whereas the forward preshower detector FPS is located on the inner end of the calorimeter cryostat. They help in the electron identification and background rejection during triggering and offline reconstruction. Offline they are also used to correct the electromagnetic energy measurement of the calorimeter for losses in the solenoid and upstream material, such as cables and support structures.

3.2.3 The Calorimeter

The calorimeter is used to measure the energy of all particles, including the neutral ones which could not be detected in the tracking system. At DØ a sampling calorimeter is realized by alternating layers of passive material in which the particles produce electromagnetic or hadronic showers with layers of active material where the surviving fraction of the shower energy can be measured. The calorimeter system consists of one central and two endcap calorimeters and an intercryostat detector. The central calorimeter (CC) covers the range of $|\eta| \leq 1$ and the two end calorimeters (EC) extend the coverage up to $|\eta| \approx 4$. Each calorimeter contains an electromagnetic section which is located closest to the interaction region, followed by a fine and a coarse hadronic section. All three detectors are located within their own cryostat to keep the detector temperature at 90 K. This is needed to keep the liquid argon in its liquid phase which is used as the active material in the calorimeter. Figure 3.6 shows the whole calorimeter system.

The absorber material used in the electromagnetic sections (EM) is made of depleted uranium and the combined thickness of all uranium layers captures almost all of the energy of electromagnetic particles. In the fine hadronic sections much thicker uranium plates are used, whereas in the coarse hadronic part copper is used as absorber. Since the nuclear interaction length is much larger than the radiation length, hadrons typically deposit most of their energy in the hadronic sections. Each calorimeter section is first divided into layers which are then segmented into cells. The third EM layer where an EM shower is expected to reach the maximum, has the finest segmentation with a cell size of $\eta \times \phi = 0.05 \times 0.05$, thus providing a rather precise information about the shower position. Towards the far forward region at $|\eta| > 3.2$ the cell size is about $\eta \times \phi = 0.2 \times 0.2$

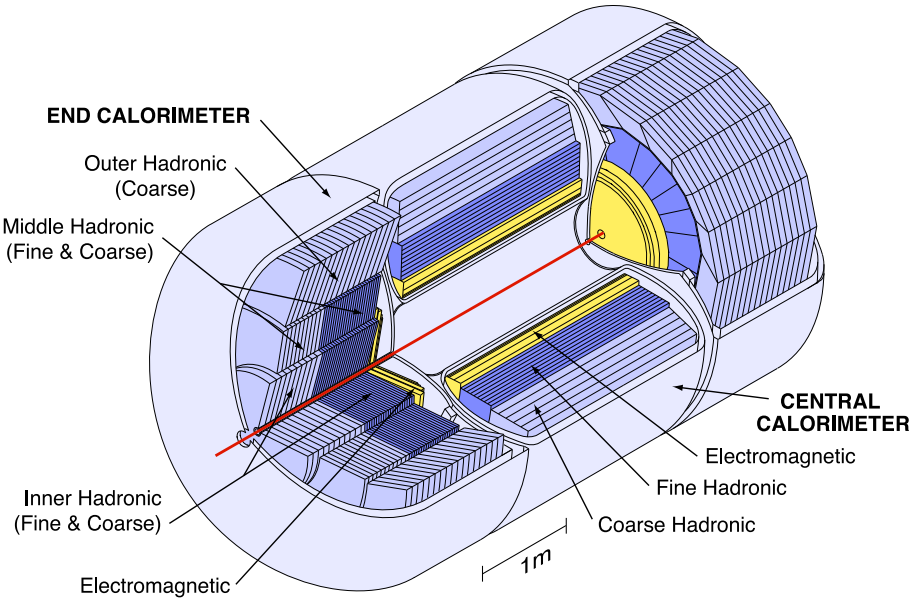

Figure 3.6: Isometric view of the central and two end calorimeters. [45]

whereas in the rest of the calorimeter a cell is of the size $\eta \times \phi = 0.1 \times 0.1$.

Due to the necessity of the separate cryostats for the different calorimeter parts, the calorimeter has incomplete coverage as well as additional material in the region $0.8 < |\eta| < 1.4$. The intercryostat detector (ICD) has been added to address this problem. The ICD provides scintillator sampling that is located at the exterior surfaces of the end cryostats and covers the region $1.1 < |\eta| < 1.4$.

3.2.4 The Muon System

When muons interact with matter they only deposit small amounts of ionization energy in the material. Therefore, they are the only charged particles which pass through the whole calorimeter and produce hits in the muon detection system. The muon detector consists of central and forward detectors where each one is separated into three layers, A, B, and C. Between the A and the B layer a toroidal magnet with a magnetic field of 1.9 T is placed to allow for a momentum measurement. The muon system is outline in Fig. 3.7.

The central muon detector covers $|\eta| < 1$ and consists of proportional drift tube (PDT) chambers and scintillation counters in each layer. The PDTs are built out of layers of drift cells where each cell has an anode wire in its center and is filled with a gas mixture of 84% argon, 8% methane, and 8% CF_4. Additional vernier cathode pads are located below and above the wire to measure the charge deposition and together with the drift time the hit position can be determined. The scintillation counters use scintillating fibers which are read out by phototubes. They provide a fast timing signal to associate a muon in a PDT with the corresponding bunch crossing since the drift times of the PDTs are longer than the bunch crossing time.

The region $1.0 < |\eta| < 2.0$ is covered by the forward muon system which uses mini drift tubes (MDT) instead of PDTs. Again, the forward system is arranged in three planes (A, B, C) each of which have layers of MDTs and a layer of scintillation pixel counters. The pixels make a precise measurement of the particle arrival times and the coincidence of these signals is used to match with the MDT information and to distinguish between muons coming from a collision and cosmic muons.

3.2.5 Luminosity Monitor

The luminosity at the DØ interaction region is measured by the luminosity monitor (LM) by detecting inelastic $p\overline{p}$ collisions. The LM consists of two detectors which are located around the beam pipe in front of the end cap calorimeters at $z = \pm 140$ cm. The detectors are built out of plastic scintillation counters which are read out by photo multiplier tubes. In order to differentiate between $p\overline{p}$ interactions and beam halo backgrounds the z coordinate of the interaction vertex is estimated using time of flight differences from particles hitting the LM detectors at $z = \pm 140$ cm. $p\overline{p}$ collisions are selected by requiring $|z_{vertex}| < 100$ cm, whereas beam halo particles will fake a vertex at $z_{vertex} \approx \pm 140$ cm.

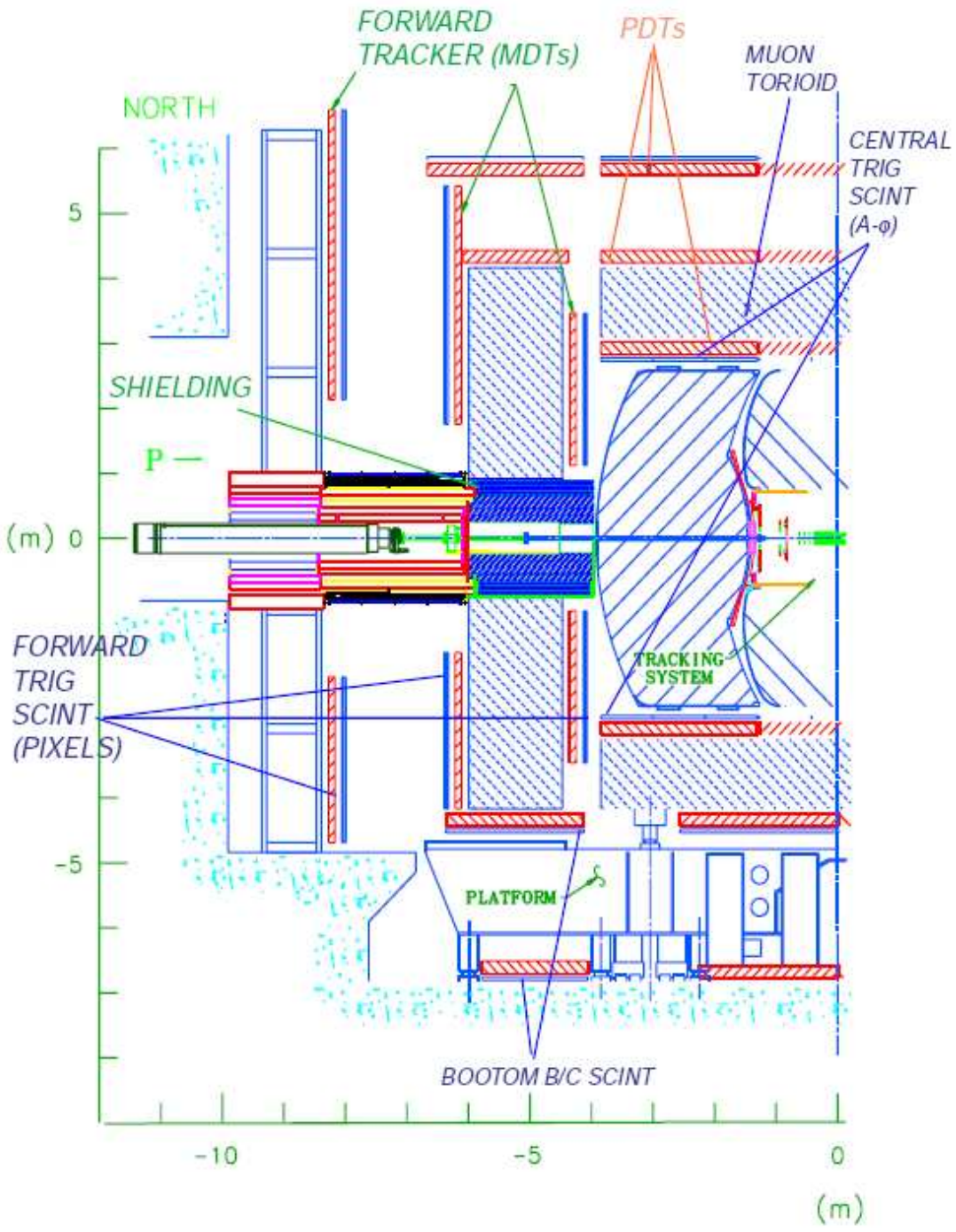

Figure 3.7: Half view of the muon system in the $r - z$ plane. [46]

3.2.6 The Trigger System

At the Tevatron collisions happen every 396 ns which is at a higher rate than events can be read out. Therefore, a trigger system is used to select interesting physics events with massive particles such as W boson, Z boson, or top-quark, out of the overwhelming number of collisions of little interest. The trigger system is separated into three levels (Level 1-3) where each succeeding level examines fewer events in more detail.

Level 1

The first stage is a collection of hardware trigger elements which reduce the rate of initially about 2.5 MHz to 2 kHz. The Level 1 trigger is divided into subdetector triggers which examine every event for interesting features. The calorimeter trigger (L1Cal) looks for energy depositions exceeding certain thresholds, whereas L1CTT (central track trigger) and L1Muon look for tracks in the central tracker and muon system, respectively.

Level 2

The Level 2 trigger tests for correlations in physics signatures and reduces the rate to 1 kHz. First L2 preprocessors collect data from each subsystem and form physics objects. Then the L2Global processor combines the information from all subsystems and examines event-wide correlations.

Level 3

At Level 3 a software trigger further reduces the rate to 50 Hz at which the data is recorded to tape. The event is approximately reconstructed using simplified reconstruction algorithms to reconstruct the physics objects, such as electrons, muons, and jets. The trigger decision is made on the whole reconstructed event by running a dedicated filter algorithm.

4 Object Identification

After a collision has taken place in the detector and all the subdetectors have provided the raw event data, this raw data has to be processed through various software algorithms to reconstruct physics objects. First clusters like hits in the tracker or deposited energy in neighboring cells of the calorimeter are formed. Various algorithms then reconstruct physical objects like electrons, muons, or jets from these clusters. The physical objects that are crucial for this analysis are tracks, vertices, electrons, muons, jets, and missing transverse energy, $\not\!\!E_T$. These objects, their reconstruction and identification is described in the following sections.

4.1 Tracks

When a charged particle traverses through the tracking detectors it passes the various detector layers and deposits energy in them. Such energy deposits are called hits. Track finding is the process of building tracks from a group of hits. The first step is pattern recognition where a list of candidate tracks is produced. At DØ two different tracking algorithms are used for pattern recognition, the AA track algorithm, as described in Ref. [47], and the Histogramming Track Finder (HTF), as described in Ref. [48]. Both are run separately to generate a list of track candidates each, which are then combined and duplicates are removed. The next and final step is then a Kalman fit to each track, which is described in detail in Ref. [49]. The Kalman fit takes care of the right propagation through the detector and calculates the final track parameters.

The AA track algorithm selects all sets of three SMT hits which lie along a path originating from the beam spot. It then extrapolates the path of the track outwards to the next layer of either SMT or CFT, to calculate the location where the track would cross the layer. If there is a hit near this location a χ^2 value is calculated for the track including the hit. If the χ^2 value is below a given maximum value the hit is kept. When there are multiple hits in a layer that produce acceptable tracks additional candidate tracks are constructed. In the case that there is no hit in a given layer, the algorithm continues in the next layer and counts a miss for that track. This procedure is repeated for each layer and each initial set of three SMT hits until a list of candidate tracks is produced. Out of all the track candidates a list of vertices is constructed. This is used to look for more track candidates that have only hits in the CFT. The same extrapolation procedure as above is used but starting at the CFT with the constraint that the track starts at a vertex.

The HFT algorithm uses the fact that the trajectory of a charged particle in the plane perpendicular to the magnetic field is a circle with its curvature and direction at the

distance of closest approach as the parameters. The algorithm divides this parameter space into bins where each pair of hits in the tracking detector corresponds to a point in this parameter space and the corresponding bin is incremented. All hits from one track correspond to the same bin, so a peak in the histogrammed parameter space is a track candidate.

4.2 Primary Vertex

The primary vertex (PV) is the point of collision between the proton and the anti-proton. Its position changes on an event-by-event basis but is crucial for identifying b-jets and to determine whether a lepton originates from the PV or not. In order to reconstruct the PV it has to be within the SMT fiducial region ($|z_{PV}| < 60$ cm), whereas the position of the PV in the transverse plane is limited by the beam size (40μm). The approach to reconstruct the PV consists of the reconstruction of candidate vertices, as described in detail in Ref. [50], and the selection of the hard scatter vertex in the event, as described in Ref. [51].

The reconstruction of candidate vertices is done in two major steps. First, tracks with $p_T > 0.5$ GeV and a loose cut on the *dca* significance (*dca*, the distance of closest approach, divided by its uncertainty) of $S_{(0,0)} < 100$, calculated with respect to $(x, y) = (0, 0)$, are fitted to a PV to locate the beam spot position. This results in a list of possible primary vertices. Then the *dca* significance of the tracks is calculated with respect to all vertex positions found in the first step. At this point only tracks with at least two SMT hits and a tight cut on the *dca* significance of $S_{(x,y)} < 3$ are used to fit the final primary vertices. There are two implementations of the PV reconstruction algorithm which differ in the track selection and fitting techniques, but show comparable performance [50]. One uses the procedure as described above and the momenta of calorimeter objects, jets, leptons and the $\not\!\!E_T$, are calculated with respect to the PV found with this algorithm. The other algorithm first clusters tracks along the z-coordinate within 2 cm of each other. All tracks in each cluster are then fitted to a vertex with a Kalman Filter technique and thus not only the vertex position is obtained, but also the tracks are refitted with the constraint of coming from the vertex. This algorithm is used for tracking related quantities and for the reconstruction of secondary vertices for b-tagging. The PVs of the two reconstruction algorithms are required to have a z-separation of less than 5 cm.

After having obtained a list of reconstructed primary vertex candidates the hard scatter vertex has to be selected. The method used [51] is based on the fact that tracks from minimum bias interactions tend to have smaller transverse momenta than tracks from hard scatter interactions. The probability of each track to come from a minimum bias event is defined using the $\log_{10} p_T$ distribution of a minimum bias sample. For each vertex the probability to originate from a minimum bias interaction is a combination of the associated track probabilities. Thus the vertex with the lowest probability is selected as the hard scatter vertex in the event.

4.3 Electrons

Electrons are identified as an accumulation of energy in the electromagnetic calorimeter (EM cluster). First a tower has to be defined as the sum of all cells sharing the same η and ϕ window of its innermost cell. An initial tower is selected in the calorimeter which has the maximum energy content and together with additional towers inside a cone of radius $R = \sqrt{\Delta\eta^2 + \Delta\phi^2} = 0.4$ a cluster is defined. The energy of the cluster is measured in all calorimeter systems and layers inside the cone. Since electrons deposit almost all of their energy inside the electromagnetic part of the calorimeter an EM cluster has to have a large EM fraction

$$f_{EM} = \frac{E_{EM}}{E_{tot}} \tag{4.1}$$

where E_{EM} is the energy of the cluster in the EM part of the calorimeter and E_{tot} the total calorimeter energy in the cone. In addition, high p_T electrons, as required in this analysis, tend to be isolated in the calorimeter. Thus the isolation fraction

$$f_{iso} = \frac{E_{tot}(R < 0.4) - E_{EM}(R < 0.2)}{E_{EM}(R < 0.2)} \tag{4.2}$$

should be small, meaning that there is not much energy in a halo around the EM cluster.

Also, the shower shape of the cluster has to be consistent with that of an electron. For this a χ^2_{Cal}, or H-Matrix (hmx7) is calculated for each cluster based on seven variables which compare the deposited energy in each layer of the EM calorimeter and the total energy of the shower based on distributions obtained from simulation. Electrons tend to have small values of χ^2_{Cal}.

All the above criteria are based on calorimeter information only. However, it is not sufficient for determining whether the EM cluster is really an electron, since photons and neutral pions also can look like electrons. Hence, the EM cluster is required to have an associated track match with

$$|\Delta\phi(EM, track)| < 0.05 \text{ and } |\Delta\eta(EM, track)| < 0.05. \tag{4.3}$$

Even after all of these cuts applied a major background remains from photons from π^0 decays which may overlap with a track from a nearby charged particle. To reject this background an electron likelihood is build out of seven variables, as described in Ref. [52]. The likelihood discriminant value of 1 indicates compatibility with the electron hypothesis while a value of 0 indicates background. When passing a value of 0.85 an electron is called tight.

The efficiencies for selecting an electron are different in data and Monte Carlo. The Monte Carlo tends to have higher efficiencies since it does not describe all of the features of the real detector, e.g. dead channels. Therefore, MC-to-data correction factors of the form

$$\kappa = \frac{\epsilon(data)}{\epsilon(MC)} \tag{4.4}$$

are used to scale Monte Carlo efficiencies to match the data efficiencies. Also the energy resolution is better in Monte Carlo than in data. The energy of the electron cluster is therefore smeared to reproduce the resolution in data. In addition, the reconstructed Z mass peak in $Z \to ee$ events is shifted compared to the position measured in data. To correct for the peak position a scale factor is applied in Monte Carlo. A detailed description of scale factors, smearing and resolution can be found in Ref. [53].

4.4 Muons

Muons are reconstructed with the informations of the muon detector and the tracking system. A muon is required to have hits in all layers of the muon system and has to be matched to a central track. For the selection in this analysis a muon with $nseg = 3$, i.e. a medium muon, is required which is given after fulfilling the following criteria as described in Ref. [54]:

- at least two wire hits in the A layer
- at least one scintillator hit in the A layer
- at least two wire hits in the B or C layer
- at least one scintillator hit in the B or C layer (except for central muons with less than four BC wire hits)
- central track and local muon track have to match

Also, the central track matched to the muon has to pass certain quality criteria:

- $\chi^2/ndf < 4$ for the track fit to remove bad track fits
- $\Delta z(\mu, PV) < 1$ cm, separation from the PV to reduce cosmic muons and/or badly reconstructed tracks
- $dca/\sigma(dca) < 3$ to reject muons from heavy flavor decays

In addition a veto on cosmic muons is applied by making use of the timing information from the scintillator hits associated with the muon. The timing cuts are scintillator times of $|t_A| < 10$ ns for the A layer and $|t_{BC}| < 10$ ns for the BC layers. Due to the toroid magnet the muon momentum can be determined from the muon detector information alone. However, the precision of the momentum measurement is significantly higher when using in addition the tracking information of the matched central track. Thus, the local momentum measurement in the muon detector is replaced by the tracking information of a global fit.

When comparing the reconstructed Z mass peak in $Z \to \mu\mu$ events in data and Monte Carlo, a better resolution and a shifted peak position is observed in Monte Carlo. To

reproduce the scale and resolution found in data, the muon momentum in Monte Carlo events is smeared accordingly, as described in Ref. [55].

Since muons in this analysis are coming from leptonic W boson decays they should be isolated from jets and thus being away from calorimeter or tracking activity. To differentiate between isolated muons and muons originating from semi-leptonic heavy flavor decays where the hadronic activity of a b-quark is not reconstructed as a calorimeter jet, the following two variables are defined:

- $$Rat11 = \text{Halo}(0.1, 0.4)/p_T^\mu \tag{4.5}$$

  where $\text{Halo}(0.1, 0.4)$ is the E_T sum of clusters in the electromagnetic or fine hadronic calorimeter in a hollow cone between $\Delta R = 0.1$ and $\Delta R = 0.4$ around the muon direction.

- $$Rattrk = \text{TrkCone}(0.5)/p_T^\mu \tag{4.6}$$

  where $\text{TrkCone}(0.5)$ is the p_T sum of all tracks, except the one matched to the muon, within a cone of $\Delta R = 0.5$ around the muon direction.

If a muon passes the cuts of $Rat11 < 0.08$ and $Rattrk < 0.06$ it is isolated and called a tight muon.

4.5 Jets

Particles resulting from a hadronization process of a quark or gluon, are reconstructed as jets in the calorimeter. Since the identification and energy measurement of jets rely on the information of the cells of the calorimeter, an algorithm has been developed to obtain a finer and uniform treatment of the calorimeter noise, which is usually due to Gaussian electronic or uranium noise. This algorithm is called T42 and is described in detail in Ref. [56, 57]. The T42 algorithm removes 3D-isolated cells which have an energy below a threshold of 4σ, where σ is the RMS of the pedestal. All cells with positive energy in the first electromagnetic layer (layer 1) or the layers 8, 9, 10 in the intercryostat region are not removed whereas cells with negative energy resulting from baseline subtracted pile-up are rejected in all layers. It was found that the T42 algorithm has almost no effect on high energy electrons which are used in this analysis [58].

After having removed the noise cells, an algorithm can be run to reconstruct the jets and the kinematic properties of the initial hadronic particle. The ideal jet algorithm should be infrared and collinear safe as illustrated in Figures 4.1 and 4.2.

In addition it should not depend on detector properties such as cell type, number or size, have a maximal reconstruction efficiency, a good energy resolution and require a minimal CPU time. Two different jet algorithms are described in the following sections, the cone and the k_T algorithm of which only the cone algorithm is used in this analysis.

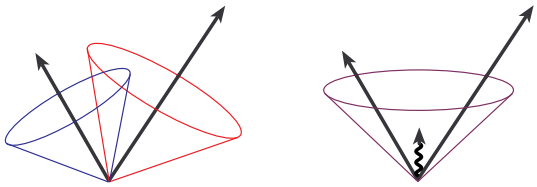

Figure 4.1: Illustration of infrared sensitivity in jet reconstruction. Clustering begins around seed particles shown as arrows with length proportional to energy. The presence of soft radiation between two jets may cause merging of the jets that would not occur in the absence of the soft radiation. [59]

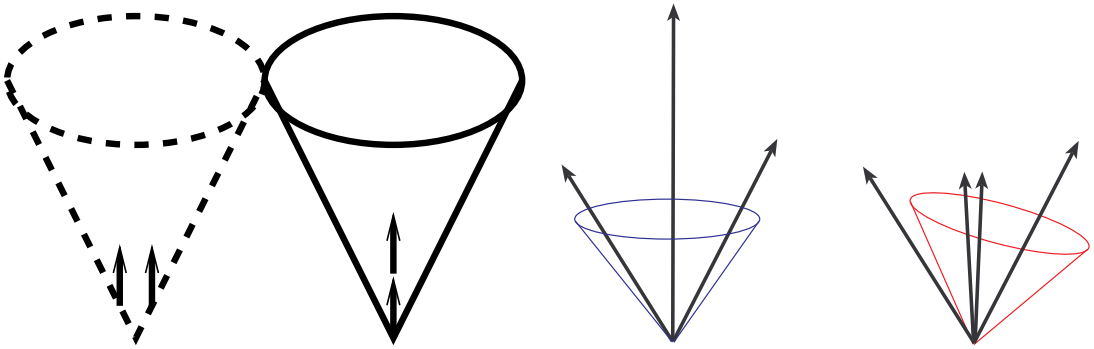

Figure 4.2: Illustration of collinear sensitivity in jet reconstruction. Left sketch: The configuration on the left fails to produce a seed because its energy is split among several detector towers, whereas a seed is produced on the right because its energy is more narrowly distributed. Right sketch: The possible sensitivity to E_T ordering of the particles that act as seeds is shown. [59]

4.5.1 The Cone Jet Reconstruction Algorithm

The cone algorithm forms jets by combining towers whose centers lie within a circle of a specific radius R in $\eta \times \phi$ space. The algorithm starts with a trial geometric axis for a cone and calculates the energy-weighted center including the contributions from all cells within the cone. This new point in $\eta \times \phi$ space is then used as a new center for the next iteration. This is repeated until a stable solution is found for the cone center which is then called a proto-jet. After all stable cones, i.e. proto-jets, have been found, a splitting and merging process starts for all proto-jets with overlapping cones. The split and merge algorithm is fully described in Fig. 4.3.

Ideally the algorithm would use each tower in the calorimeter as the first trial geometric axis. Unfortunately the number of calorimeter towers in DØ are in the order of 6000 for tower sizes of $\Delta\eta \times \Delta\phi = 0.1 \times 0.1$ and thus very large. Therefore, the theoretically favored seedless approach is computationally expensive. An acceptable approximation is obtained when using only towers with energies above a seed threshold for finding proto-jets. In the seed based cone algorithm only calorimeter towers passing a cut of

$$E_T^{tower} > E_T^{seed} = 0.5 \text{ GeV} \tag{4.7}$$

are used as starting points for the proto-jets. Another improvement of the seed-based algorithm is the implementation of additional starting seeds, so called midpoints. These midpoints are E_T weighted centers between pairs of proto-jets. To reduce the sensitivity of the algorithm to soft radiation, midpoints are created where all seeds lie within a distance

$$\Delta R < 2.0 \cdot R_{cone} \tag{4.8}$$

of each other. The described jet reconstruction procedure is called Improved Legacy Cone Algorithm and is the one used in this analysis with a cone size of $R = 0.5$. More and detailed information can be found in Ref. [59].

4.5.2 The k_T Jet Reconstruction Algorithm

The k_T jet algorithm starts with a list of preclusters which are formed from calorimeter cells. Such preclusters are built out of calorimeter towers with positive energy which are merged if they are close together in $\eta \times \phi$ space. A flowchart of the k_T algorithm is shown in Fig. 4.4. The distance between preclusters (*i*,*j*) is defined as

$$d_{ij} = \min(p_{t,i}^2, p_{t,j}^2) \frac{(y_i - y_j)^2 + (\phi_i - \phi_j)^2}{D^2} \tag{4.9}$$

where D is a parameter of the algorithm and the rapidity, y, is defined as

$$y = \frac{1}{2} \ln \frac{E + p_z}{E - p_z} \tag{4.10}$$

For $D = 1$ and

$$\Delta\mathcal{R}_{ij} = \sqrt{(y_i - y_j)^2 + (\phi_i - \phi_j)^2} << 1, \tag{4.11}$$

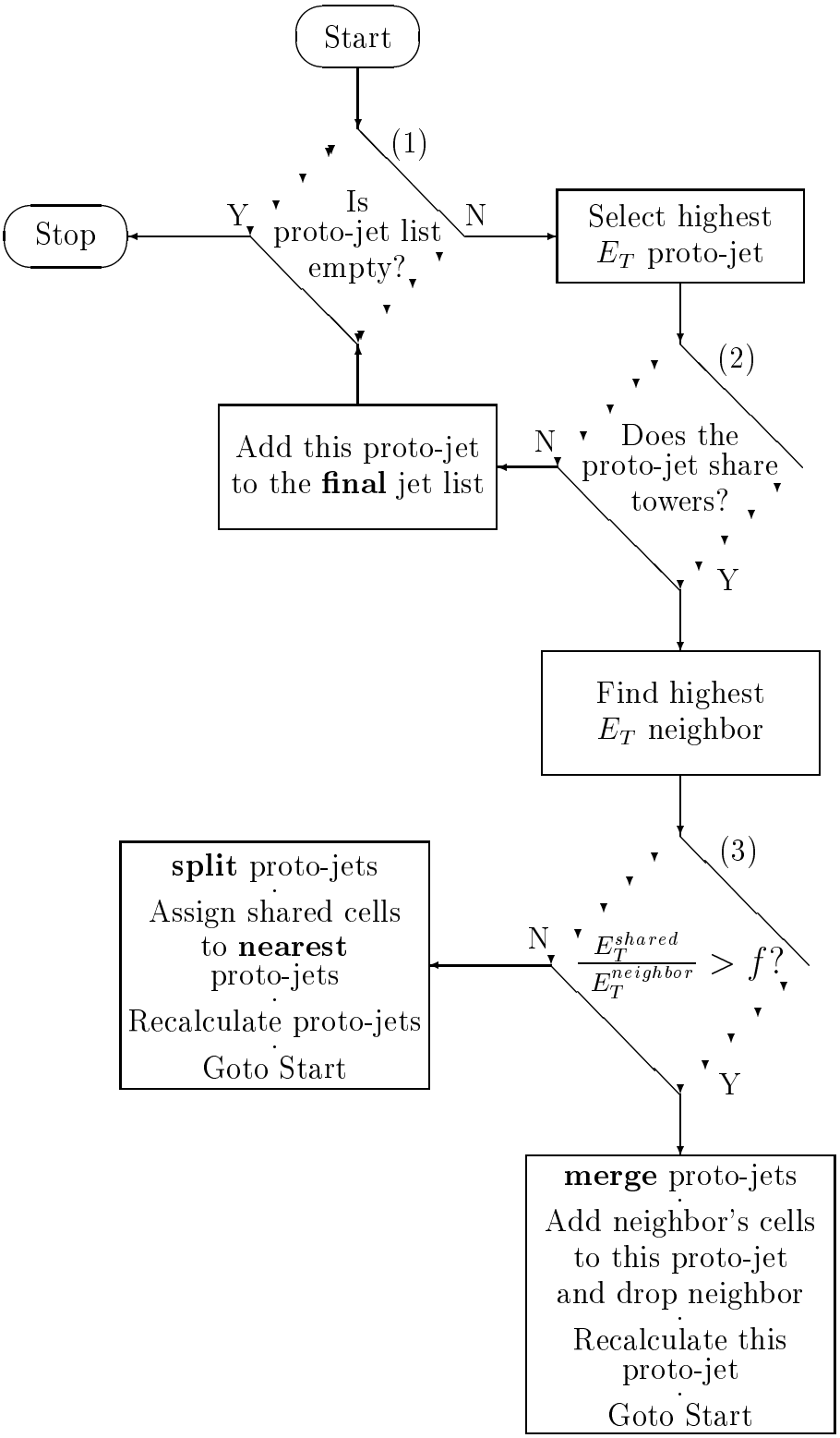

Figure 4.3: Description of a fully specified splitting and merging algorithm. The threshold of energy fraction being shared is $f = 0.5$. [59]

d_{ij} is the minimal relative transverse momentum k_T^2 of one vector with respect to the other. In Figure 4.5 an example of how the k_T algorithm successively merges preclusters can be seen. More detailed information about the k_T algorithm can be found in Ref [59]. The k_T algorithm produces a list of jets where the jets are separated by $\Delta\mathcal{R} > D$. Thus, the parameter D has the same meaning as the parameter R for the cone algorithm. Note that k_T jets do not have to include all particles within a cone of radius D around the jet axis, and can also contain particles outside of this cone.

The two algorithms differ in their principle method of constructing jets. A cone jet is constructed through geometrical constraints and has a fixed size and shape which is ideally a cone (except for the splitted and merged jets). Therefore, it will not gather the energy of particles which have been produced through hadronization and are lying just outside the cone. A k_T jet on the other hand is adjusted to the particles coming from radiation processes and will include the energy of nearby clusters, as sketched in Fig. 4.6. When comparing a $R = 0.7$ cone jet with a k_T jet of the corresponding size $D = 1.0$, the k_T jet typically includes more energy when reconstructing the same parton [60].

4.5.3 Jet Identification

After the jets are reconstructed with the cone algorithm and all jets with $E_T^{reco} < 8$ GeV are removed, further quality selection cuts have to be applied to separate real jets from fake ones due to noise. These cuts are:

- The requirement of $0.05 < f_{EM} < 0.95$ removes the electromagnetic particles at the high end and jets with a disproportional amount of hadronic energy at the low end.
- Since the coarse hadronic section has a higher noise level a jet is required to have a coarse hadronic fraction of $CHF < 0.4$. This removes jets which deposit their energy predominantly in the coarse hadronic layers of the calorimeter and are likely to have clustered around noise.
- Jets clustered from hot cells are removed by cutting on the ratio of the highest to the next-to-highest transverse energy cell in the calorimeter $HotF < 10$.
- To remove those jets reconstructed from a single hot tower, the number of towers containing 90% of the energy has to be greater than 1, $n_{90} > 1$.
- To further reject noise jets, a comparison of the energy in the L1 calorimeter towers to the energy obtained in the precision read-out is being performed. This is a powerful discriminant against noise which does not appear simultaneously in the two independent read-out chains. Defining $L1SET$ to be the scalar sum of the E_T of the trigger towers in the same cone as the jet, the cut applied is:

$$\frac{L1SET}{p_T^{jet}(1 - CHF)} > 0.4 \text{ (in CC and EC) or } > 0.2 \text{ (in ICD)} \qquad (4.12)$$

  More information about L1 confirmation can be found in Ref. [61].

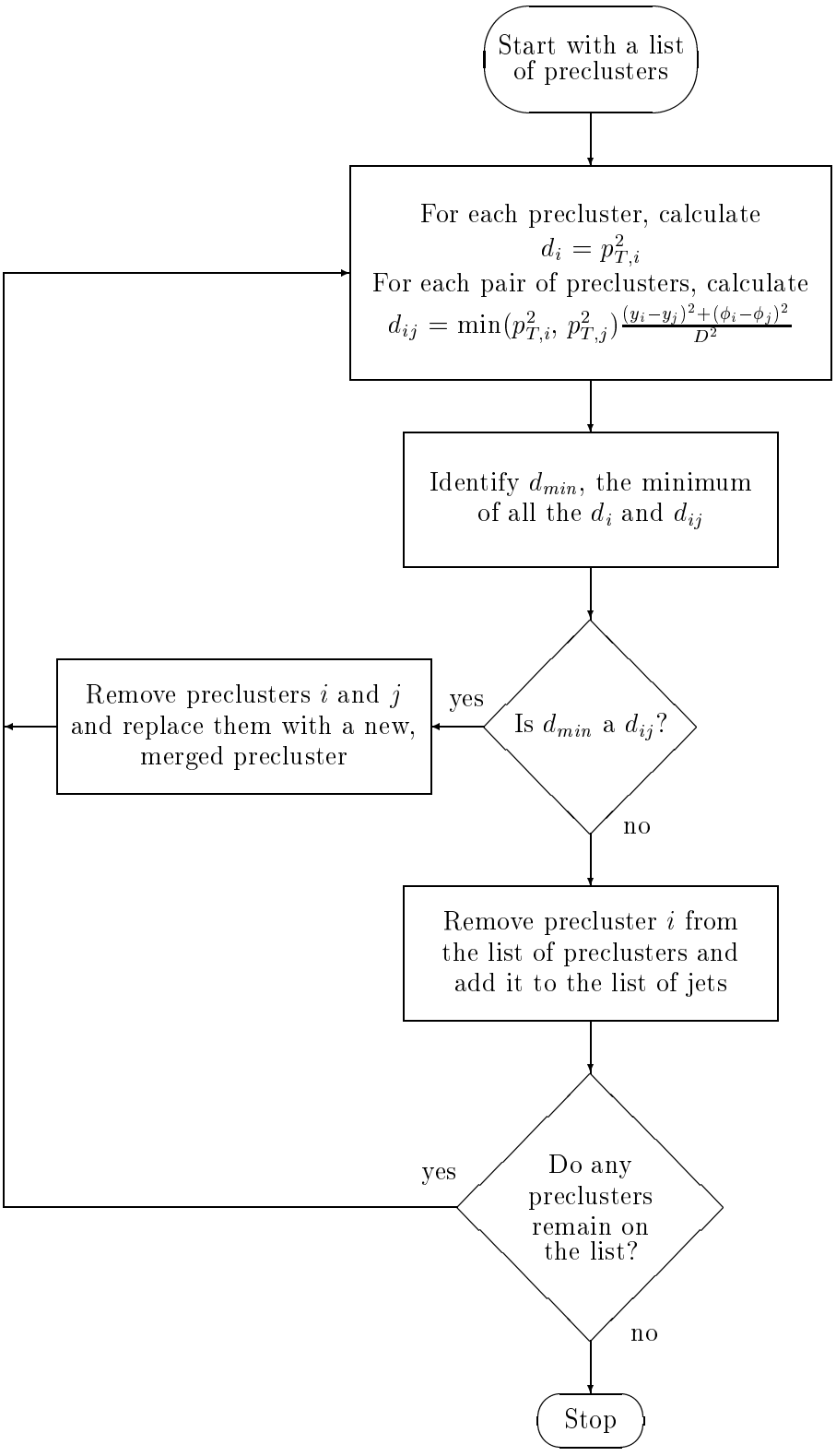

Figure 4.4: Flowchart of the k_T jet algorithm. [59]

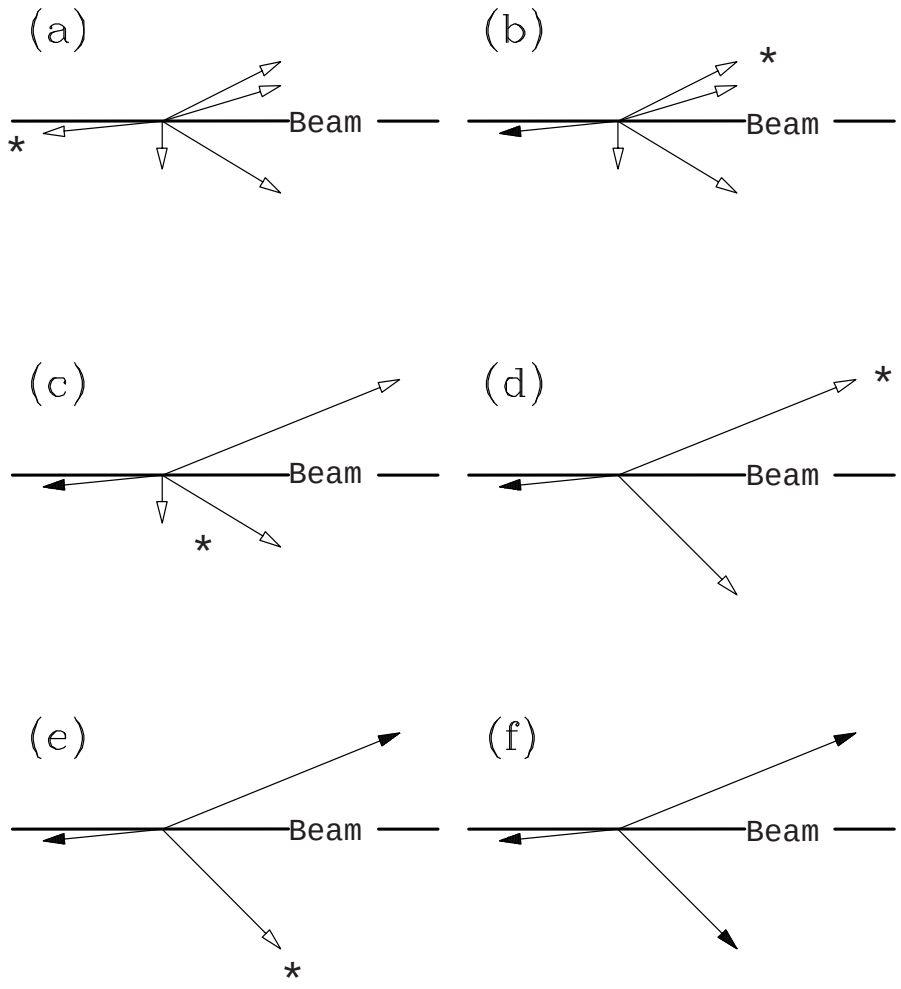

Figure 4.5: Example of merging preclusters with the k_T jet algorithm. Open arrows represent preclusters, while the solid arrows represent the final jets. The six diagrams show the successive iterations and the asterisk labels the relevant precluster at each step. In each diagram either a jet is defined or preclusters are merged. [59]

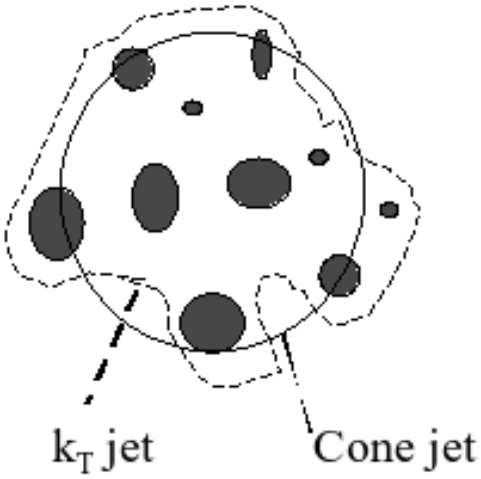

Figure 4.6: Shape comparison of cone and k_T jets.

Electrons and photons with a transverse energy above 8 GeV and which pass a cut on $f_{EM} > 0.9$ are also reconstructed as jets in the calorimeter. These jets are removed from the list if they can be matched to an electromagnetic object within $\Delta R(jet, EM) < 0.5$ and have a $p_T > 15$ GeV.

As with electrons and muons, the jet reconstruction and identification efficiencies in Monte Carlo do not agree with the ones from data. Therefore, p_T-dependent scale factors have been determined and MC jets are randomly removed in order to reproduce the jet reconstruction and identification efficiency present in data. The exact description of the procedure and the derivation of the scale factors can be found in Ref. [62].

4.5.4 Jet Energy Scale

The raw energy of a reconstructed jet is given by the sum of energies deposited in the calorimeter cells within the jet cone and is affected by noise, calorimeter response, showering effects, and the underlying event. The jet energy scale (JES) corrections attempt to correct the reconstructed jet energies, E_{reco}, back to the particle level energy, E_{corr}, which the partons had at the point of their generation. So the original energy of the particle which it had before interacting with the calorimeter should be regained. The correction can be written as

$$E_{corr} = \frac{E_{reco} - O}{R \cdot S}, \tag{4.13}$$

where R is the calorimeter response, S the fraction of shower leakage outside the jet cone due to instrumental effects, and O is the energy offset due to the underlying event, energy pile-up, multiple interactions, and electronic and uranium noise. R is determined by requiring E_T balancing in γ+jet events between the photon and the calorimeter towers

of the jet, while S is obtained by measuring the energy profiles of jets. O is derived from energy densities in minimum bias trigger events. Despite all these corrections, E_{corr} does not need to be the parton energy since the parton may have radiated additional partons before hadronization which may or may not end up in the cone jet.

Heavy flavor jets are expected to have a different JES correction. In particular b-jets may have a different response and also a different showering correction due to their harder fragmentation. In this analysis a different correction is only applied to jets which contain a muon within $\Delta R(\mu, \text{jet}) < 0.5$). This muon is assumed to come from a semileptonic b decay, which produces a neutrino along with the muon. In Ref. [63] a detailed description of the jet energy scale measurement can be found.

In this analysis the JetCorr v5.3 package is used which corrects the jet energies in data as well as in Monte Carlo. The corrections are done jet-by-jet and different corrections are applied for jets in data and Monte Carlo, since the Monte Carlo may not model all the effects mentioned above accurately. A description of the package can be found in Ref. [64]. The jet energy scale measurement depends significantly on the used jet algorithm. Up to the point in time when this analysis was performed, JES corrections were only available for a cone algorithm with $\Delta R = 0.5$.

4.5.5 Jet Energy Resolution

The resolution of the jet energy measurement is important for every analysis, especially the resolution found in data and Monte Carlo should be equal. Unfortunately, the width of the jet energy distribution is found to be underestimated in the simulation, and Monte Carlo jets are smeared to match the jet resolution observed in data, as described in detail in Ref. [55]. The applied smearing is done according to a random Gaussian distribution with a width of

$$\sigma = \sqrt{(\sigma_{p_T}^{data})^2 - (\sigma_{p_T}^{MC})^2} \tag{4.14}$$

with $\sigma_{p_T}^{MC}$ being the resolution found in Monte Carlo, and $\sigma_{p_T}^{data}$ the one in data.

4.6 *b*-Tagging

The identification of jets coming from a b-quark is a crucial ingredient for this analysis to improve the signal to background ratio. Due to the relatively long lifetime of the b-quark it can travel several millimeters before decaying. This results in two main ways to identify a b-jet. One possibility is to reconstruct secondary vertices from charged particle tracks, another to select charged particle tracks which are significantly displaced from the primary vertex. A third possibility is to identify a muon within a jet, since in 10% of the time a B-hadron will decay semileptonically into a muon. Five different methods to identify ("tag") a b-jet are used at DØ.

- **Counting Signed Impact Parameters (CSIP):** counts the number of tracks identified in a jet with a large impact parameter (dca) significance with respect to the primary vertex. The sign of the impact parameter is given by the sign of

the projection of the impact parameter onto the track-jet axis. For an event to be considered tagged (i.e. having an identified b-jet) it has to have at least three tracks with an impact parameter significance greater than 2, or two tracks with an impact parameter significance greater than 3. More information can be found in Ref. [65].

- **Jet Lifetime Probability (JLIP):** combines the impact parameter information from all tracks inside a jet into one variable, the jet lifetime probability (JLIP Prob) which is the probability that all tracks originate from the primary vertex. The closer to zero the more likely that the jet comes from a b-quark. More information can be found in Ref. [66].

- **Secondary Vertex Tagger (SVT):** explicit reconstruction of a secondary vertex with a large decay length significance with respect to the primary vertex. More information follows in this section and can be found in Ref. [67, 68, 69].

- **Soft Lepton Tagging (SLT):** uses the identification of a muon within a jet. More information can be found in Ref. [70].

- **Neural Network b-tagging Tool:** uses variables from the SVT, CSIP and JLIP taggers as input for a neural network to identify b-jets. More information follows in this section and can be found in Ref. [71, 72].

In this analysis the SVT algorithm is used to tag a jet as a b-jet. The algorithm will be described in the following section. The Neural Network tagger will also be described since it will be used for cross-checks later on in the analysis.

4.6.1 Secondary Vertex Tagger

The SVT algorithm needs the reconstruction and identification of the primary vertex, as described in Sect. 4.2. Then track-based jets, so called track-jets need to be reconstructed before finding a secondary vertex. The first step in the reconstruction of the track-jets is to cluster tracks according to their z of closest approach with respect to $z = 0$ and then to form preclusters by looping in descending order of p_T over the tracks and adding the track if $\Delta z < 2$ cm (Δz is the difference between the z of closest approach of the track and the precluster). For every precluster the closest primary vertex is identified and tracks are selected which have $p_T > 0.5$ GeV, ≥ 1 SMT hits, $|dca| < 0.20$ cm and $|zdca| < 0.4$ cm. These selected tracks are then clustered in $\eta \times \phi$ space using the cone jet algorithm with seed $p_T > 1$ GeV, forming the track-jets. A track-jet consists of at least two tracks.

For every track-jet the secondary vertex finding is performed, following these steps:

1. Track selection: only tracks with $p_T > 1.0$ GeV and a (signed) impact parameter significance with respect to the primary vertex of $|dca|/\sigma(dca) > 3.5$ are considered.

2. Vertex finding and fitting: search for a secondary vertex within every track-jet is performed with at least two selected tracks, using the *Build-Up* algorithm.
   Build-Up algorithm: The algorithm starts with finding seed vertices by fitting all combinations of pairs of tracks within a track-jet. Then, additional tracks are attached to the seed vertices according to the resulting χ^2 contribution to the vertex. This process is repeated until no more tracks can be associated to the seed. The resulting vertices are allowed to share tracks.

3. Vertex selection: the secondary vertices found are required to fulfill the following cuts:

   - track multiplicity ≥ 2
   - $|L_{xy}| < 2.6$ cm, with the decay length $|L_{xy}| = |(\vec{r}_{SV} - \vec{r}_{PV})_{xy}|$
   - $|L_{xy}/\sigma(L_{xy})| > 7.0$
   - $|\hat{L}_{xy} \cdot \hat{p}_{SV}| > 0.9$, where $\hat{p}_{SV}$ is the normalized vertex momentum which is computed as the vector sum of the momenta of all tracks attached to the secondary vertex, and $\hat{L}_{xy}$ is the normalized decay length.
   - $\chi^2/ndf < 10$

A calorimeter jet is identified as a b-jet if it contains a selected secondary vertex within $\Delta R < 0.5$. The sign of the decay length is given by the sign of $\hat{L}_{xy} \cdot \hat{p}_{SV}$. If the jet contains at least one secondary vertex with $L_{xy} > 0$, the tag is called positive, otherwise the tag is called negative. Until otherwise noticed only positive tags are used.

Throughout this analysis an event is called tagged if it contains at least one jet which is identified as a b-jet. The terminology of an untagged event corresponds to an event before b-tagging is applied.

Taggability

The tagging efficiencies observed in data are not well described by the current version of the DØ Monte Carlo simulation, since dead detector material and noise in the tracking system are not or inadequately modeled. As a result, applying the SVT algorithm directly to Monte Carlo gives wrong results, i.e. significantly higher b-tagging rate, and jet tagging efficiencies have to be applied instead. The probability to identify a b-jet is composed of the probability for a jet to be "taggable" (also called taggability) and the probability for a taggable jet to be tagged, also called tagging efficiency. A calorimeter jet is taggable if it is matched within $\Delta R \leq 0.5$ to a track-jet as defined above. The separation of these two probabilities decouples the tagging efficiency from tracking and calorimeter noise problems which are absorbed in the taggability.

The taggability is expected to have a strong dependence on the position of the primary vertex, since the SMT coverage is different for barrel and F-disks. The geometrical constraints imposed by the tracking system require that the position of the PV along the beam axis (z_{PV}) has to be taken into account when determining the jet taggabilities. The relative sign between the z_{PV} and the jet η must also be considered, as can be seen

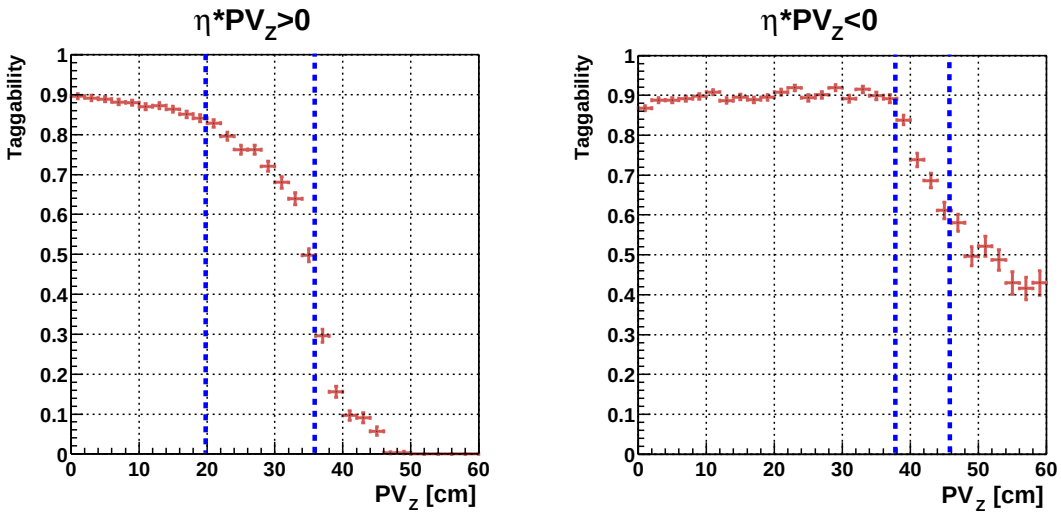

Figure 4.7: Dependence of the taggability on the relative sign between z_{PV} and jet η (z_{PV} is denoted PV_z in the plots). [73]

in Fig. 4.7. This figure shows the behavior of the taggability observed in preselected l+jets data as a function of z_{PV} for a positive and negative relative sign.

In Figure 4.8 the taggability parameterized as a function of jet p_T and η in six bins of z_{PV} is shown. It can be seen that the taggability is lower for high η regions when the PV is more central. If the PV is at the edges of the SMT barrels, the taggability drops and is even 0 for low $|\eta|$, since the F-disks at this positions do not provide coverage at $\eta = 0$. The determination and validation of the parameterization can be found in detail in Ref. [73].

The taggability measured in data is dominated by the light jet contribution (from u,d,s quarks or gluon) and therefore, it describes the taggability of light jets. But some flavor dependence of the taggability can be expected since the track p_T spectrum is harder and the average track multiplicity is larger for heavy flavor (b and c) jets than for light jets, due the harder fragmentation of heavy flavor jets. To account for this, the taggability is corrected by the ratios of the b to light and c to light jet taggabilities, as specified in Ref. [73].

Tagging Efficiencies, Mistag Rate and Scale Factors

The b-tagging efficiency in data is measured for semileptonic b-decays on a sample enriched in $b\bar{b}$production, as described in Ref. [74]. The b- and c-tagging efficiency in Monte Carlo is obtained from processes like $Wb\bar{b}$, $Wc\bar{c}$, $Z \rightarrow b\bar{b}, c\bar{c}$ and parameterized as a function of jet E_T and η. All details can be found in Ref. [74]. Since the Monte Carlo is expected to yield a significantly higher tagging efficiency than in data, as mentioned above, the b-tagging efficiency in Monte Carlo needs to be calibrated to that measured

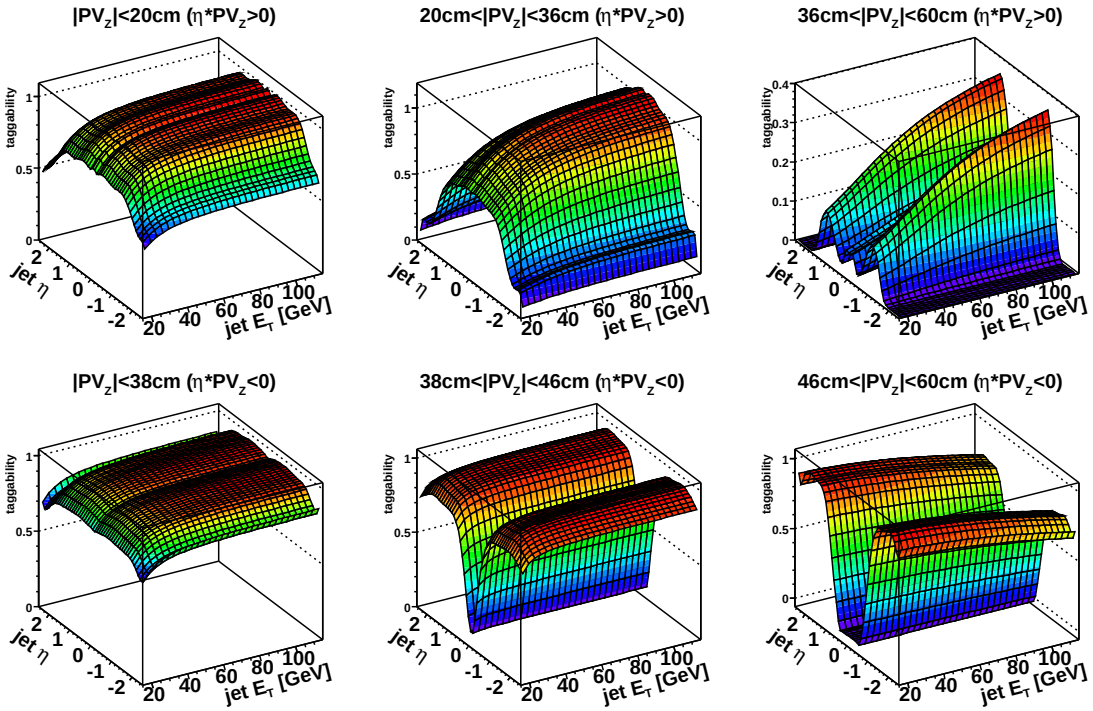

Figure 4.8: Two dimensional parameterization of taggability for different (z_{PV},$z_{PV} * \eta$) bins (z_{PV} is denoted PV_z in the plots). [73]

in data. Therefore, a scale factor is defined as:

$$SF_{b\to\mu}(E_T,\eta) = \frac{\epsilon^{data}_{b\to\mu}(E_T,\eta)}{\epsilon^{MC}_{b\to\mu}(E_T,\eta)} \tag{4.15}$$

where $\epsilon^{MC}_{b\to\mu}$ is the semileptonic b-tagging efficiency in Monte Carlo and $\epsilon^{data}_{b\to\mu}$ in data. Assuming that the scale factor for inclusive b-decays is the same as for semileptonic ones, $SF_b = SF_{b\to\mu}$, the calibrated Monte Carlo tagging efficiency for inclusive b-decays is defined as:

$$\epsilon_b(E_T,\eta) = \epsilon^{MC}_b(E_T,\eta)\cdot SF_b(E_T,\eta) \tag{4.16}$$

where ϵ^{MC}_b is the inclusive b-tagging efficiency in Monte Carlo. Since it is not straightforward to measure the c-tagging efficiency in data, and thus the scale factor SF_c, it is assumed to be equal to the b-tagging scale factor,$SF_c = SF_b$. The inclusive c-tagging efficiency in Monte Carlo is then defined analogously:

$$\epsilon_c(E_T,\eta) = \epsilon^{MC}_c(E_T,\eta)\cdot SF_c(E_T,\eta) \tag{4.17}$$

Mistags are light flavor jets which are tagged mostly because of track misreconstruction and/or resolution effects causing tracks from the PV to appear displaced. Since resolution effects are expected to contribute to both positive and negative tags, the mistag rates can be measured in data from the rates of jets with negative tags. The negative tagging efficiency in data for taggable jets is defined as

$$\epsilon^{data}_-(E_T,\eta) = \frac{\#\text{negatively tagged jets in}(E_T,\eta)\text{ bin}}{\#\text{taggable jets in }(E_T,\eta)\text{ bin}}, \tag{4.18}$$

and derived as a negative tag rate function from data. To correct for the effects of heavy flavor contamination (hf) and contributions from long-lived particles (ll) such as K^0_S and Λ, as described in detail in Ref. [74], scale factors are applied in such a way that the negative tag efficiency measured in data is corrected to obtain the positive mistag efficiency for light flavor jets defined by:

$$\epsilon_l(E_T,\eta) = \epsilon^{data}_-(E_T,\eta)\cdot SF_{hf}(E_T,\eta)\cdot SF_{ll}(E_T,\eta) \tag{4.19}$$

where SF_{hf} is the ratio of negative tagging efficiency for light flavor jets only and the one inclusive over flavors, and SF_{ll} is the ratio of positive to negative tagging efficiencies for light flavor jets.

All the parameterizations described above are applied to all jets in all Monte Carlos samples resulting in an individual weight for each event.

4.6.2 Neural Network Tagger

Another method to identify a b-jet is to use the Neural Network (NN) b-tagging tool, as described in Ref. [71], which combines the information of the different b-tagging algorithms mentioned above. The input variables to the NN ranked in order of their separation power are:

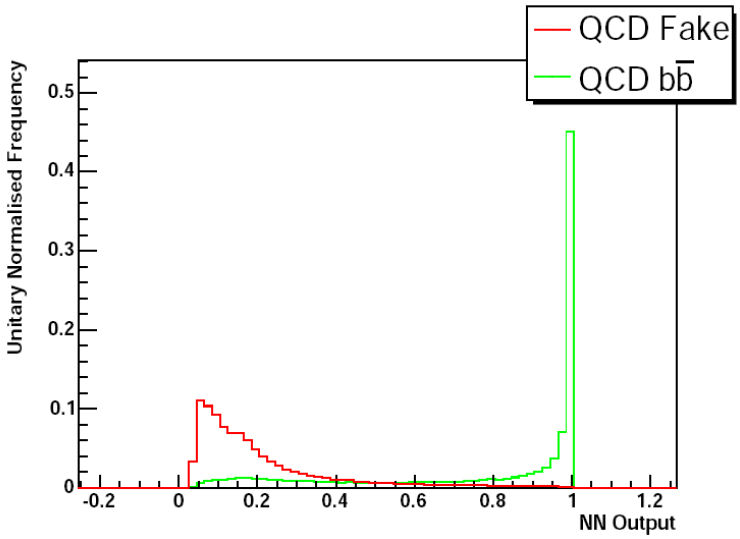

Figure 4.9: Comparative NN output for a QCD b-jet and a QCD uds-jet sample. [71]

- **SVT DLS:** the decay length significance of the secondary vertex with respect to the primary vertex given by the SVT algorithm.
- **CSIP Comb:** weighted combination of the impact parameter significance of all the tracks.
- **JLIP Prob:** probability that the jet originates from the primary vertex.
- **SVT χ^2_{ndf}:** χ^2 per degree of freedom of the secondary vertex.
- **SVT N_{track}:** number of tracks used to reconstruct the secondary vertex.
- **SVT Mass:** mass of the secondary vertex.
- **SVT Num:** number of secondary vertices found in the jet.

Before a jet is fed into the NN it has to fulfill the selection cuts: SVT DLS > 2.5 or JLIP Prob < 0.02 or CSIP Comb > 8. The output from the optimized NN b-tagger for a QCD b-jet signal sample and a QCD uds-jet background sample is shown in Fig. 4.9. Since variables from the SVT algorithm are used in the NN only those jets can potentially be tagged which already have a secondary vertex.

What was the case for the SVT algorithm is also true for the NN b-tagger. The tagging efficiencies observed in data are not described well by the Monte Carlo simulation, where in comparison the b-tagging efficiency is too high. In order to use the NN output for Monte Carlo as used for data, i.e. taking the NN output value as a probability for a jet to be tagged, corrections would be needed. Unfortunately these are not available since for each single output value of the NN a Monte Carlo correction would have to

be derived. This is obviously impracticable. Instead, Monte Carlo parameterizations in η and p_T were derived for six operation points of the NN. This reduces the b-tag information on data to a tagged or not tagged (0/1) decision when the NN output is above or below the operation point. On Monte Carlo the efficiencies corresponding to the chosen operating point are applied to each jet. The procedure is in analogy to the one described in Sect. 4.6.1 and details can be found in Ref. [72].

Despite of the operating points and the derived parameterizations to treat the Monte Carlo correctly, the NN will be directly applied to Monte Carlo in this analysis, treating it the same way as data. This is due to fact that it is desired to have a b-tagging algorithm which is not reduced to a 0/1 decision on data, but gives b-tag weights. Since it is know that the b-tagging efficiencies are too high for Monte Carlo when applying the NN directly, the NN b-tag information will be used only as a cross-check.

4.7 Missing Transverse Energy

The direct observation of neutrinos in the detector is impossible since they do not interact with any of the detector systems. Therefore neutrinos have to be identified as an imbalance of energy in the transverse plane and thus appear as missing transverse energy, $\not\!\!E_T$. The imbalance is reconstructed from the vector sum of the transverse energies of all calorimeter cells which pass the T42 algorithms, see Sect. 4.5. Excluded from the calculation are the cells in the coarse hadronic layers due to their high noise level. They are only considered if they are part of a reconstructed jet. Having calculated the vector sum of all transverse energies, the raw $\not\!\!E_T$ is the momentum vector pointing in the opposite direction in ϕ to balance the energy in the transverse plane.

Since electromagnetic objects and jets are corrected for different calorimeter response, these corrections have to be propagated to the $\not\!\!E_T$ vector to account for the change in energy imbalance, resulting in the calorimeter $\not\!\!E_T$. If a high-p_T muon is present in the event it will not deposit much energy in the calorimeter. Since the calorimeter $\not\!\!E_T$ does not account for this, part of the energy imbalance in the transverse plane may come from a muon and not from neutrinos. Therefore, an additional correction is applied to the calorimeter $\not\!\!E_T$. The momentum of all muons as measured in the central tracking detector is corrected for the expected minimum-ionizing energy deposition in the calorimeter and then subtracted vectorically from the calorimeter $\not\!\!E_T$. This results in the $\not\!\!E_T$ which is used throughout this analysis.

5 Data and Monte Carlo Simulation Samples

In this analysis data recorded by the DØ detector between August 2002 and August 2004 has been analyzed. After a $p\bar{p}$ collision has taken place, it has to be decided by the trigger system if the event is interesting enough to be recorded, since the capabilities of the data recording and analysis structures are limited. For different physics processes different triggers are required which preselect events with certain objects, in this analysis the decay products of $t\bar{t}$. Then a quality check is made for the recorded data to make sure that all detector components were fully operational.

To compare the data with the expectation, Monte Carlo simulations are needed. Samples of different physics processes were generated to describe signal and background, which together add up to the selected data in this analysis.

5.1 Event Trigger

In this analysis events with a $t\bar{t}$ signature, i.e. one lepton, one neutrino and at least four jets are needed. Therefore, a trigger was designed which selects a lepton and jets, to ensure that the relevant data are recorded. While the analyzed data sample was recorded, different triggers were applied over time, since the triggers had to be adapted to the increased luminosities. Single triggers are collected in trigger lists and versions 8 to 13 were used during this data taking period.

5.1.1 Trigger in the e+jets channel

The trigger conditions for the e+jets channel [75] for trigger list versions v8–v11 are at Levels 1 to 3 ("EM15_2JT15"):

- **Level 1** (CEM$(1, 10)$_CJT$(2, 5)$)**:** one calorimeter EM trigger tower with a transverse energy $E_T > 10$ GeV and two jet towers with $E_T > 5$ GeV
- **Level 2** (EM$(.85, 10)$_JET$(2, 10)$)**:** one EM candidate with $E_T > 10$ GeV and EM fraction of > 0.85 and two jet candidates with $E_T > 10$ GeV
- **Level 3** (ELE_LOOSE_SHT$(1, 15)$_JET$(2, 15)$)**:** one electron candidate with a transverse energy $E_T > 15$ GeV and two jet candidates with $E_T > 15$ GeV

For v12 the following conditions are used ("E1_SHT15_2J20"):

- **Level 1** (CEM(1, 11))**:** one calorimeter EM trigger tower with $E_T > 11$ GeV
- **Level 2:** no requirements
- **Level 3** (ELE_NVL_SHT(1, 15)_JET(2, 20))**:** one electron candidate with transverse energy $E_T > 15$ GeV and two jet candidates with $E_T > 20$ GeV

For v13 the following conditions are used ("E1_SHT15_2J_J25"):

- **Level 1** (CEM(1, 11))**:** one calorimeter EM trigger tower with $E_T > 11$ GeV
- **Level 2** (CALEM(1, 15))**:** one calorimeter EM cluster with $E_T > 15$ GeV
- **Level 3** (ELE_NVL_SHT(1, 15)_JET(1, 20)_JET(2, 25))**:** one electron candidate with $E_T > 15$ GeV, two jet candidates with $E_T > 20$ GeV and one jet candidate with $E_T > 25$ GeV

5.1.2 Trigger in the μ+jets channel

In the μ+jets channel the following trigger conditions [75] were used in trigger list versions 8 to 11 ("MU_JT20_L2_M0"):

- **Level 1** (mu1pxatxx_CJT(1, 5))**:** one muon scintillator coincidence and one jet tower with $E_T > 5$ GeV
- **Level 2** (MUON(1, *med*))**:** one medium muon
- **Level 3** (JET(1, 20))**:** one jet candidate with $E_T > 20$ GeV

For v12 the following conditions are used ("MU_JT25_L2_M0"):

- **Level 1** (mu1pxatxx_CJT(1, 3))**:** one muon scintillator coincidence and one jet tower with $E_T > 3$ GeV
- **Level 2** (MUON(1, *med*)_JET(1, 10))**:** one medium muon and one jet candidate with $E_T > 10$ GeV
- **Level 3** (JET(1, 25))**:** one jet candidate with $E_T > 25$ GeV

For trigger list version 13 slightly different subversions (v13.0-v13.1 and v13.2) are used whose conditions differ only at Level 3. The trigger conditions are ("MUJ2_JT25" for v13.0-v13.1 and "MUJ2_JT25_LM3" for v13.2):

- **Level 1** (mu1pxatlx_CJT(1, 5)_ncu)**:** one muon scintillator coincidence and a wire hit, and one jet tower with $E_T > 3$ GeV
- **Level 2** (MUON(1, *med*)_JET(1, 8))**:** one medium muon and one jet candidate with $E_T > 8$ GeV
- **Level 3:**
  for v13.0-v13.1 (JET(1, 25)): one jet candidate with $E_T > 25$ GeV
  for v13.2 (JET(1, 25)_MUON(1, 3., *loose*)): one jet candidate with $E_T > 25$ GeV and one muon with $E_T > 3$ GeV

	e+jets	μ+jets
Trigger List	$\int \mathcal{L}$ (pb^{-1})	$\int \mathcal{L}$ (pb^{-1})
v8	19.4	20.0
v9	21.2	21.2
v10	15.1	15.3
v11	54.9	57.3
v12	209.8	209.8
v13	45.8	39.6
total	366.2	363.2

Table 5.1: Breakdown of integrated luminosities by trigger list version for the e+jets and the μ+jets channels.

5.2 Data Quality

The performance of the detector is monitored online by the shifters in the control room and offline by comparing relevant kinematical distributions of reconstructed objects. If a subdetector was not working properly or was even disabled during a run, which is a data taking period of usually up to four hours during which the configuration of the detector has not changed, its condition is stored in a run quality database. The quality of the data is ensured by requiring a good run, where all detector systems were working properly.

A luminosity block (LBN) corresponds to about a minute of data taking and is the smallest unit for which the integrated luminosity can be calculated. A LBN is declared bad if it is affected by problems in the calorimeter causing certain noise patterns. The selection of good luminosity blocks ensures good calorimeter data quality.

Finally, events are rejected if the information recorded by the precision read-out deviates significantly from the independent Level 1 trigger read-out. This is a way to reject events with fake high $\not\!\!E_T$ due to calorimeter electronic related effects, like noise. A detailed motivation and description of this procedure is given in Ref. [76].

After all these event quality cuts the final data sample consists of 366 pb^{-1} in the e+jets channel and 363 pb^{-1} in the μ+jets channel. In Table 5.1 a breakdown of the luminosities for the different trigger list versions in the e+jets and μ+jets channels can be seen. The uncertainty on the luminosity is 6.5% [77].

5.3 Monte Carlo

For this analysis the study of the signature of the signal process and the comparison with the background processes is indispensable. Therefore, Monte Carlo (MC) simulations of these processes were used. The complete chain of generating a Monte Carlo event for a given process is as following:

- The hard scatter interaction is described by calculating the leading order matrix

element using a specific Monte Carlo generator. The generator used at this point is different for the signal and background processes and will be discussed below. The set of parton distribution functions used for all generators is CTEQ5L [78].

- The underlying event which consists of beam-beam remnants and multiple parton interactions are modeled with PYTHIA 6.202 [79]. Beam-beam remnants describe the outgoing partons of the $p\overline{p}$ interaction which did not take part in the hard scattering process. Multiple parton interactions can occur when after the hard scattering the remaining partons interact.

- Multiple proton interactions, i.e. when more than one $p\overline{p}$ interaction in the two colliding bunches take place, is simulated by superimposing minimum bias Monte Carlo events to the event. The number of added events is taken from a Poisson distribution with a mean of 0.8 events. The minimum bias is added in a program called `d0sim` [80].

- Pile-up describes overlapping $p\overline{p}$ interactions from consecutive bunch crossings in the detector which are reconstructed in one event. This is currently also simulated with `d0sim`, in the future randomly recorded zero bias data events will be used for modeling.

- The hadronization of the generated partons into colorless mesons and baryons is done by PYTHIA.

- After all particles have been generated their passage through the detector and the energy deposition within has to be simulated. This is done by `d0gstar`, a GEANT based simulation package, as described in Ref. [81], in which the detector material and geometry is described.

- The response of the detector to the energy depositions are simulated with `d0sim`.

- The next step is the reconstruction of the physical objects based on the digitized information from all detector components. From this point on Monte Carlo events are treated the same way as data events.

The only thing which is not included in simulation is the trigger information. Therefore, the probability of each Monte Carlo event to pass the trigger requirements is calculated, as described in Ref. [82], using trigger efficiencies measured in data.

All Monte Carlo samples for the signal and background processes are generated at $\sqrt{s} = 1.96$ TeV and are discussed in the following.

5.3.1 Resonance Signal

The resonance signal Monte Carlo is generated using PYTHIA 6.202 for the hard scatter interaction and the following parton shower for ten different resonance masses M_X, between 350 GeV and 1000 GeV. The width of the resonance is set to $\Gamma_X = 0.012 M_X$.

M_X [GeV]	Γ_X [GeV]	number of MC events	M_{top} [GeV]
350	4.2	56000	175.0
400	4.8	57000	175.0
450	5.4	61000	175.0
500	6.0	64000	175.0
550	6.6	55000	175.0
600	7.2	59000	175.0
650	7.8	60000	175.0
750	9.0	60000	175.0
850	10.2	64000	175.0
1000	12.0	83000	175.0

Table 5.2: Summary of all resonance Monte Carlo samples.

This qualifies X as a narrow resonance since its width is smaller than the assumed mass resolution of the DØ detector which was about 0.04 M_X in Run I and has not been measured yet in Run II. The width of 1.2% was also chosen in order to compare the results with Run I analyses where this width was used.

In PYTHIA the resonance X was set to be a Z' boson generated through the process $f_i\bar{f}_i \rightarrow \gamma/Z^0/Z^{0\prime}$. In the matrix elements only the $Z^{0\prime}$ boson is considered and thus no interference between γ, Z^0, and $Z^{0\prime}$ is taken into account which is valid for a narrow width approximation. The width is calculated dynamically as a function of the actual mass and is set to the desired value by setting the vector and axial couplings. This is needed since in general the full interference structure $\gamma/Z^0/Z^{0\prime}$ needs to be included to get the right cross section away from the peaks, even though the interference is switched off for this analysis. The resonance is forced to decay to $t\bar{t}$ only; the $t\bar{t}$ decays are inclusive. The top quark mass is set to 175 GeV. A list of the main parameters used in PYTHIA is provided in Appendix A.1.

Since this analysis is performed only in the l+jets channel the generic Monte Carlo event selector `d0_mess` [83] is used to filter events where $t\bar{t}$ decays semileptonically. Only these events are processed through the full detector simulation and event reconstruction. The semileptonic $t\bar{t}$ decays include the τ+jets channel and the τ decay is described by TAUOLA [84]. Table 5.2 provides a summary of all resonance MC samples X$\rightarrow t\bar{t}$. The samples sizes are the numbers of reconstructed events after `d0_mess`.

5.3.2 Standard Model $t\bar{t}$

The hard interaction for the Standard Model $t\bar{t}$ production is simulated using ALPGEN 1.3.3 [85]. For subsequent generation of parton shower, hadronization and hadron decays PYTHIA was used. The $t\bar{t}$ Monte Carlo was generated in the $t\bar{t} \rightarrow l$+jets and the $t\bar{t} \rightarrow l\bar{l}$+jets channel for top-quark masses of 170 GeV, 175 GeV, and 180 GeV. The main samples used are the ones with a top-quark mass of 175 GeV, whereas the other samples are needed for systematic studies. The nominal top-quark mass was set

flavor sample	fraction in %
$Wjjjj$	77.99 ± 0.44
$Wcjjj$	4.87 ± 0.16
$W(b\bar{b})Jjj$	2.83 ± 0.15
$W(c\bar{c})Jjj$	4.93 ± 0.35
$Wb\bar{b}Jj$	2.85 ± 0.11
$Wc\bar{c}Jj$	4.52 ± 0.20

Table 5.3: Expected fraction of each W+jets flavor after preselection and parton-jet matching for both channels. [74].

to 175 GeV because this value lies within the uncertainties of the world average value of 172.7 ± 2.9 GeV [12] at the point in time of this analysis. For additional systematic studies a $t\bar{t}$ $+j$ sample has been generated where one additional jet comes directly from the matrix element calculation and not later on from the parton shower.

5.3.3 W+jets

The W+jets background is simulated using ALPGEN for the hard interaction which also allows various combinations of flavored quarks to be generated separately. For W+4jets events the following samples were used: $Wjjjj$, $Wcjjjj$, $WccJj$, $WbbJj$, $W(cc)Jjj$, and $W(bb)Jjj$, where j is any of u,d,s,g and J is any of u,d,s,c,g partons. $(c\bar{c})$ and $(b\bar{b})$ denote heavy quark pairs which are reconstructed in one jet. The processes $Wcccc$, $Wbbcc$, and $WbbbbJj$ have not been generated since their cross sections are negligible.

The W+jets events are generated in ALPGEN and then interfaced with PYTHIA for showering and additional jets can be produced by the parton shower. No parton-matching is applied at generator level to merge a matrix element calculation and a parton shower Monte Carlo. So in order to get the right W+jets flavor fractions only those events were used in this analysis where an initial quark produced by ALPGEN can be matched to a reconstructed jet. The fractions of the different W+jets flavor subprocesses can be found in Table 5.3.

5.3.4 Single Top Production

The electroweak production of the top-quark is modeled by the SingleTop generator which is based on the CompHEP package, described in Ref. [86]. For the simulation of the underlying event and the hadronization PYTHIA is used. For this analysis only the t-channel process was considered. The cross section of the s-channel process is by a factor of two lower and in addition it has a lower jet multiplicity which would only lead to a very small background contribution and is therefore neglected.

6 The $t\bar{t}$ Invariant Mass Distribution

After the dataset has been defined and all the important objects have been identified, $t\bar{t} \rightarrow l$+jets like events have to be selected for the analysis. Then, the background needs to be estimated in order to compare the data to the standard model expectation. The essential part of this analysis is the determination of the invariant mass of the $t\bar{t}$ system. Thus, the reconstruction of the $t\bar{t}$ decay products and the correct combination to rebuild the top and anti-top quarks needs to be discussed and studied in detail.

6.1 Event Selection

Due to the signature of top-quark events as described in Sect. 2.2, the event preselection requires a high p_T lepton, at least four jets and high missing E_T. The lepton is either an electron or a muon in the e+jets or μ+jets channel, respectively. After the general object identification, as described in Sect. 4, special quality cuts have to be applied to select top-like events for this analysis. Common to both channels are the general event quality cuts such as passing the trigger requirement and the ones related to the primary vertex and the jets. At least one of the jets has to be tagged as a b-jet by the SVT algorithm as previously described in Sect. 4.6.1. These cuts are summarized in Table 6.1. Compared to other top-quark analyses which have a jet p_T cut of 20 GeV, the cut in this analysis (and also other b-tag analyses) could be lowered to 15 GeV since the requirement of at least one b-tag reduces additional background. For the low p_T jets in the range of $15 - 20$ GeV the uncertainty on the jet energy scale is larger but on the other hand the statistic for the analysis is enhanced.

In the e+jets channel an isolated electron is required which passes all quality cuts shown in Table 6.2 including the tight criteria. The quality cuts which a muon in the μ+jets channel has to pass are shown in Table 6.3. This includes that the muon has to

Object	Selection Cut
Event	match trigger requirement
Primary vertex	≥ 3 tracks attached
	$\lvert z_{PV} \rvert < 60$ cm
Jets	≥ 4 jets with $p_T > 15$ GeV and $\lvert \eta \rvert < 2.5$
	≥ 1 jet tagged as b-jet

Table 6.1: Event preselection cuts.

Object	Selection Cut (e+jets)
Electron	$f_{EM} > 0.9$, $f_{iso} < 0.15$, hmx7 $\chi 2 < 50$ } *Electron ID*
	$\lvert\eta\rvert < 1.1$
	only 1 *tight* electron with $p_T > 20$ GeV
	matched to central track
	electron track $p_T > 10$ GeV
	$\lvert\Delta z(e, PV)\rvert < 1$ cm
	Likelihood $L > 0.85$ } *tight requirement*
Muon	no tight muon with $p_T > 15$ GeV
Missing E_T	$\not\!\!E_T > 20$ GeV
	$\Delta\phi(e, \not\!\!E_T) > 2.2 - \not\!\!E_T \cdot 2.2/48.9$

Table 6.2: Preselection cuts for the e+jets channel.

Object	Selection Cut (μ+jets)
Muon	medium muon with $n_{seg} = 3$, satisfies cosmic veto } *Muon ID*
	matched to central track
	$\lvert\eta\rvert < 2.0$
	$p_T > 20$ GeV
	$\Delta R(\mu, jet) > 0.5$
	muon track $\chi 2 < 4$
	$\lvert dca\rvert/\sigma_{dca} < 3$
	$\lvert\Delta z(\mu, PV)\rvert < 1$ cm
	no second tight μ with $p_T > 15$ GeV
	Z veto on 70 GeV $< m_{\mu\mu} <$ 110 GeV
	Halo$(0.1, 0.4)/p_T < 0.08$, TrkCone$(0.5)/p_T < 0.06$ } *tight requirement*
Electron	no electron with $p_T > 15$ GeV
Missing E_T	$\not\!\!E_T > 20$ GeV
	$\Delta\phi(\mu, \not\!\!E_T) > 0.1 \cdot \pi - 0.1 \cdot \pi \cdot \not\!\!E_T/50$
	$\Delta\phi(\mu, \not\!\!E_T) < 0.8 \cdot \pi + 0.2 \cdot \pi \cdot \not\!\!E_T/30$

Table 6.3: Preselection cuts for the μ+jets channel.

be isolated and thus fulfill the tight requirements. In both channels there is a veto on any additional tight lepton above a certain p_T. A cut on the missing transverse energy is required as well as a cut on the azimuthal angle, $\Delta\phi$, between the lepton and $\not\!\!E_T$, to reduce background. A more detailed discussion of the cuts and their optimization can be found in Ref. [87] for the e+jets channel and in Ref. [62] for the μ+jets channel.

6.1.1 Preselection Efficiencies

The preselection efficiencies after applying the trigger weight but before performing the b-tag are shown in Table 6.4 for the SM $t\bar{t}$ $\rightarrow l$+jets sample and the samples of X$\rightarrow t\bar{t}$ with ten different masses.

When looking at the efficiencies of the different samples it is noticeable that the efficiency for a 400 GeV resonance is almost comparable to the efficiency of the $t\bar{t}$ sample while the efficiencies of the different resonance samples deviate a lot from each other. From the lowest mass of 350 GeV to a mass of 600 GeV the preselection efficiency is increasing in both e+jets and μ+jets channels while it decreases for the higher masses up to 1000 GeV.

To understand the differences between $t\bar{t}$ $\rightarrow l$+jets and the different masses of X$\rightarrow t\bar{t}$ the individual preselection cuts have to be looked at in detail. A break down of the preselection efficiencies for the SM $t\bar{t}$ $\rightarrow l$+jets sample and three samples of X$\rightarrow t\bar{t}$ with exemplary masses of 400 GeV, 600 GeV, and 1000 GeV can be found in Table 6.5 for the e+jets channel and in Table 6.6 for the μ+jets channel. The three chosen X$\rightarrow t\bar{t}$ samples include the ones with the highest and with the lowest preselection efficiency.

By comparing the cut efficiencies it can be seen that the cuts on energy related variables like lepton p_T and $\not\!\!E_T$, isolating variables like ΔR and the tight criteria, and the requirement of at least four jets have the biggest changes in efficiency between the presented samples. A 400 GeV resonance has almost the same cut flow as the SM

sample	e+jets	μ+jets
$t\bar{t}$ $\rightarrow l$+jets	14.42 ± 0.13	14.28 ± 0.18
350 GeV X$\rightarrow t\bar{t}$	12.53 ± 0.22	12.22 ± 0.22
400 GeV X$\rightarrow t\bar{t}$	14.87 ± 0.24	13.59 ± 0.23
450 GeV X$\rightarrow t\bar{t}$	16.25 ± 0.24	15.50 ± 0.23
500 GeV X$\rightarrow t\bar{t}$	17.64 ± 0.24	16.92 ± 0.24
550 GeV X$\rightarrow t\bar{t}$	17.83 ± 0.26	17.21 ± 0.26
600 GeV X$\rightarrow t\bar{t}$	18.23 ± 0.25	17.80 ± 0.25
650 GeV X$\rightarrow t\bar{t}$	17.20 ± 0.25	17.08 ± 0.25
750 GeV X$\rightarrow t\bar{t}$	15.43 ± 0.24	15.56 ± 0.24
850 GeV X$\rightarrow t\bar{t}$	13.52 ± 0.22	14.72 ± 0.22
1000 GeV X$\rightarrow t\bar{t}$	11.39 ± 0.18	12.53 ± 0.19

Table 6.4: Preselection efficiencies before applying the b-tagging in the e+jets and μ+jets channel for SM $t\bar{t}$ $\rightarrow l$+jets and X$\rightarrow t\bar{t}$ for the ten different resonance masses.

	exclusive efficiency in e+jets			
cut	$t\bar{t} \rightarrow l$+jets	400 GeV X	600 GeV X	1000 GeV X
Electron ID	67.78 ± 0.17	66.14 ± 0.32	69.62 ± 0.30	65.69 ± 0.26
η	84.45 ± 0.16	84.22 ± 0.30	84.69 ± 0.28	83.01 ± 0.26
p_T	93.88 ± 0.12	93.07 ± 0.24	94.37 ± 0.21	95.59 ± 0.16
track match	91.57 ± 0.13	91.31 ± 0.25	92.02 ± 0.23	91.44 ± 0.21
track p_T	99.91 ± 0.02	99.92 ± 0.03	99.95 ± 0.02	99.95 ± 0.02
$\not\!\!E_T$	89.24 ± 0.16	87.72 ± 0.32	91.96 ± 0.25	95.87 ± 0.16
$\Delta\phi(e, \not\!\!E_T)$	93.98 ± 0.13	94.31 ± 0.24	94.12 ± 0.23	95.94 ± 0.16
2. lepton veto	99.94 ± 0.01	99.98 ± 0.02	99.97 ± 0.02	99.90 ± 0.03
good PV	97.64 ± 0.09	98.11 ± 0.15	98.01 ± 0.14	97.46 ± 0.13
tight	89.20 ± 0.18	88.29 ± 0.35	88.04 ± 0.32	82.20 ± 0.32
≥ 4 jets	43.59 ± 0.30	44.71 ± 0.57	51.45 ± 0.53	35.03 ± 0.45
trigger	92.21 ± 0.25	91.64 ± 0.46	92.77 ± 0.39	92.77 ± 0.45
total efficiency	14.42 ± 0.13	14.87 ± 0.24	18.23 ± 0.25	11.39 ± 0.18

Table 6.5: A break down of preselection efficiencies in the e+jets channel for SM $t\bar{t} \rightarrow l$+jets and X$\rightarrow t\bar{t}$ for three different resonance masses.

	exclusive efficiency in μ+jets			
cut	$t\bar{t} \rightarrow l$+jets	400 GeV X	600 GeV X	1000 GeV X
good PV	97.56 ± 0.06	97.76 ± 0.10	97.45 ± 0.10	97.50 ± 0.09
Muon ID	75.32 ± 0.16	74.90 ± 0.29	75.45 ± 0.29	75.96 ± 0.24
track match	97.12 ± 0.07	97.01 ± 0.13	96.98 ± 0.13	96.35 ± 0.12
η	99.87 ± 0.02	99.89 ± 0.03	99.87 ± 0.03	99.87 ± 0.02
p_T	72.93 ± 0.19	71.88 ± 0.36	74.63 ± 0.34	77.93 ± 0.27
ΔR(μ,jet)	84.49 ± 0.18	83.09 ± 0.35	84.48 ± 0.33	75.05 ± 0.32
track $\chi 2$	99.88 ± 0.02	99.86 ± 0.04	99.91 ± 0.03	99.87 ± 0.03
$\lvert dca \rvert / \sigma_{dca}$	94.06 ± 0.13	94.38 ± 0.24	93.92 ± 0.23	93.52 ± 0.21
$\lvert \Delta z(\mu, PV) \rvert$	99.98 ± 0.01	99.97 ± 0.02	99.97 ± 0.02	99.98 ± 0.01
$\not\!\!E_T$ & $\Delta\phi$	89.90 ± 0.17	87.58 ± 0.35	92.91 ± 0.26	95.52 ± 0.18
2. lepton veto	99.85 ± 0.02	99.91 ± 0.03	99.78 ± 0.05	99.61 ± 0.06
Z veto	99.56 ± 0.04	99.56 ± 0.07	99.38 ± 0.08	98.47 ± 0.11
tight	87.39 ± 0.20	85.22 ± 0.40	88.68 ± 0.33	85.45 ± 0.32
≥ 4 jets	48.06 ± 0.32	49.68 ± 0.61	55.95 ± 0.56	43.26 ± 0.49
trigger	92.27 ± 0.25	91.96 ± 0.47	92.44 ± 0.40	92.98 ± 0.43
total efficiency	14.28 ± 0.18	13.59 ± 0.23	17.80 ± 0.25	12.53 ± 0.19

Table 6.6: A break down of preselection efficiencies in the μ+jets channel for SM $t\bar{t} \rightarrow l$+jets and X$\rightarrow t\bar{t}$ for three different resonance masses.

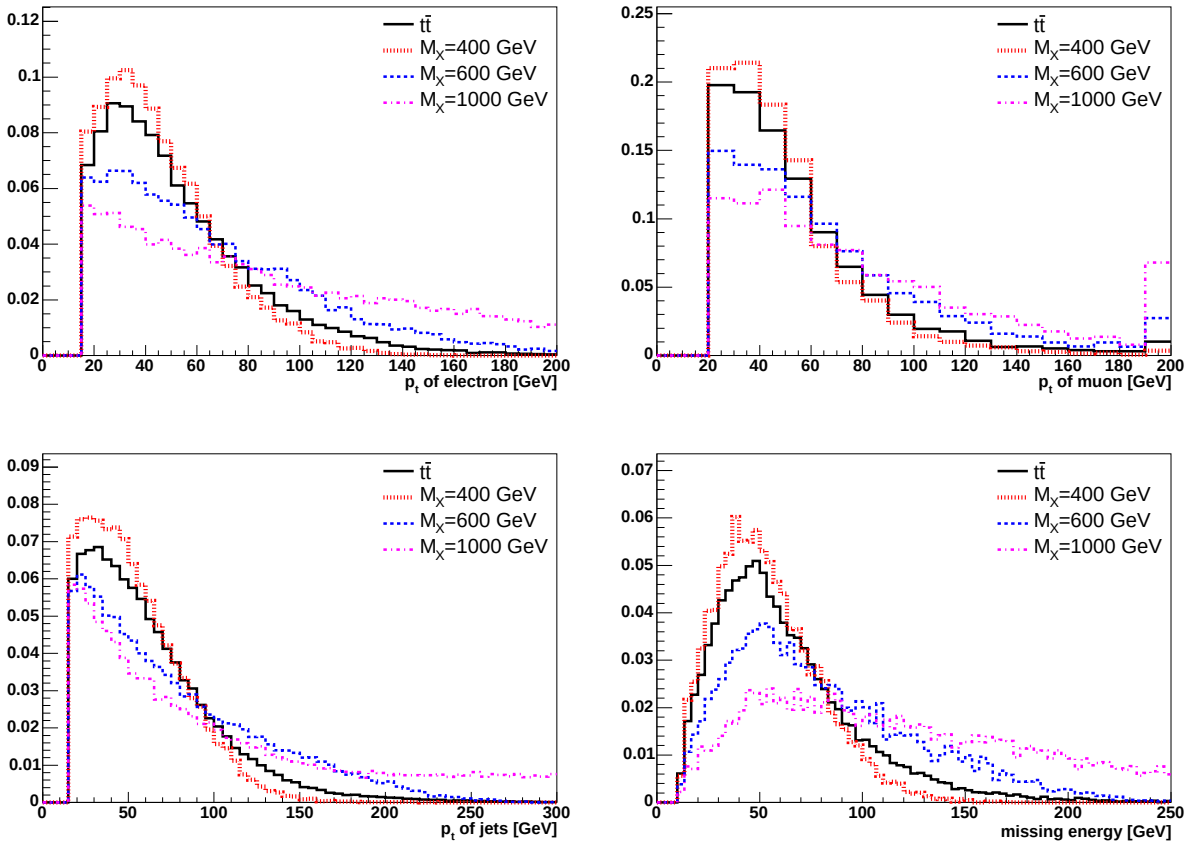

Figure 6.1: Shape comparison of energy variables between $t\bar{t}$ and X$\rightarrow t\bar{t}$ for three different resonance masses. The variables from top left to bottom right are: p_T of the electron in the e+jets channel, p_T of the muon in the μ+jets channel, p_T of the jets for both channels combined and missing E_T for both channels combined.

$t\bar{t} \rightarrow l$+jets sample because the continuum $t\bar{t}$ is produced mostly at threshold. With higher resonance masses the total energy rises and leptons, jets and neutrinos are more energetic as can be seen in Fig. 6.1, which shows a shape comparison of energetic variables between $t\bar{t} \rightarrow l$+jets and X$\rightarrow t\bar{t}$. As a consequence the efficiencies of the cuts on lepton p_T and $\not\!\!E_T$ increase from low to high resonance masses.

On the other hand the $t\bar{t}$ system is more boosted with higher resonance masses and the jets and leptons get closer together. As a result the efficiency of cuts on ΔR between muon and the closest jet (in the μ+jets channel) and the tight requirements which include an isolation criteria decrease towards high resonance masses. Also a decrease in the efficiency of the cut on $\Delta\phi(\text{lepton}, \not\!\!E_T)$ could be expected but since this cut depends also on $\not\!\!E_T$, the efficiency increases. In the e+jets channel this slightly increasing cut efficiency can directly be seen, whereas in the μ+jets channel the efficiency of the $\Delta\phi(\mu, \not\!\!E_T)$ is only available combined with the efficiency of the $\not\!\!E_T$ cut.

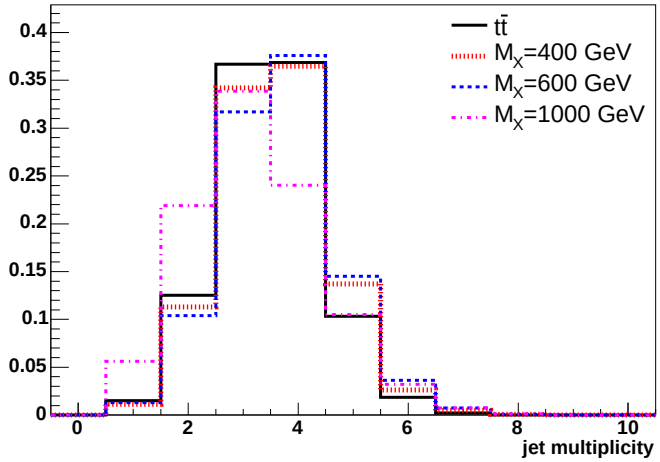

Figure 6.2: Jet multiplicity distribution of $t\bar{t}$ and X$\rightarrow t\bar{t}$ for three different resonance masses.

By far the largest impact especially on the low efficiency of the 1000 GeV resonance mass sample has the requirement of at least four jets in an event. While the rate of having at least four jets in the event is of about the same size for the SM $t\bar{t} \rightarrow l$+jets and the 400 GeV X$\rightarrow t\bar{t}$ sample, it increases for the 600 GeV resonance and decreases for 1000 GeV. This is due to the fact that the average jet multiplicity is higher for the lower resonance masses and gets lower for higher resonance masses as can be seen in Fig. 6.2.

To find a reason for the jet multiplicity behavior in the high mass resonance samples, the minimal distance between the direction of two quarks at parton level was investigated. This distribution is shown in Fig. 6.3 for the $t\bar{t} \rightarrow l$+jets and three different X$\rightarrow t\bar{t}$ samples. For the 1000 GeV sample the shape of the distribution is very different than for the samples with lower masses or even $t\bar{t} \rightarrow l$+jets . While the distributions of SM $t\bar{t} \rightarrow l$+jets and 400 GeV X$\rightarrow t\bar{t}$ are very broad and peak above 1.0, the distribution of the 1000 GeV sample is much narrower and peaks around 0.6. This trend towards narrower distributions which peak towards lower ΔR for higher resonance masses can be confirmed when looking at the distribution of the 600 GeV X$\rightarrow t\bar{t}$ sample. When taking into account the cone size of 0.5 of the jet reconstruction algorithm as described in Sect. 4.5.1 it is obvious that the jet finder cannot separate two quarks closer together than 0.5. Thus, the chosen value of ΔR of the cone jet finding algorithm influences, i.e. reduces the preselection efficiency. With a greater fraction below 0.5 compared to the others, the 1000 GeV resonance sample is forced to have a lower jet multiplicity and therefore a low efficiency when requiring at least four jets. The opposite fits for the 600 GeV resonance sample where the distribution is lower than for the other samples up to $\Delta R \approx 0.7$. This can also explain the efficiency increase of the jet multiplicity cut between the 400 GeV and 600 GeV resonances samples.

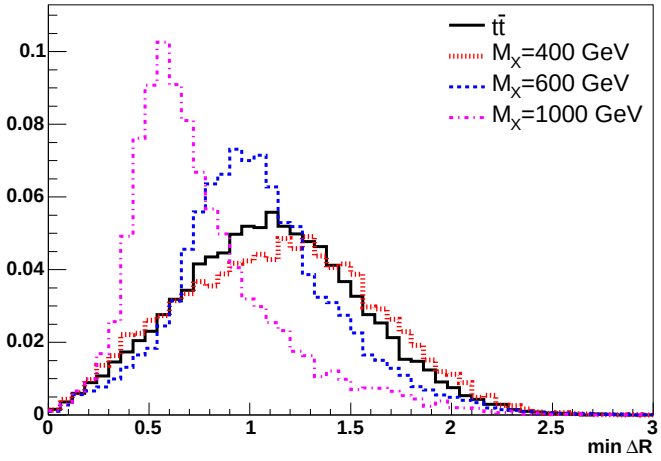

Figure 6.3: Minimal distance in ΔR in $\eta \times \phi$ space between two quarks at parton level for $t\bar{t}$ and X$\rightarrow t\bar{t}$ for three different resonance masses.

For the high mass resonances, the two quarks closest to each other are most likely the two quarks coming from the W-boson, whereas the two b quarks have the largest distance between each other, as Fig. 6.4 shows for the selected samples. But also the light quarks from the W boson decay are close to one of the b quarks, the one flying in the same direction as the W boson and coming from the same top quark. For the lower resonance masses and $t\bar{t}$ the quarks are not that close together and ΔR is more distributed between $2-3$.

A possible improvement could be the use of a cone size of $R = 0.3$ or an entirely different jet finding algorithm such as the k_T algorithm, as described in Sect. 4.5.2. The k_T algorithm is taking into account only energetic towers in the calorimeter resulting in a variable shape and size according to the energy deposition rather than being fixed to a well defined size given by a cone. Unfortunately these different jet finders could not be used in this analysis since no jet energy scales existed for them.

In the preselection efficiencies presented up to now, the requirement of at least one tagged jet was not included. Therefore, the b-tagging efficiencies for the different samples are presented separately in Table 6.7. As can be seen, the b-tagging efficiencies are about equal for all the different samples.

6.2 Background Estimation

The two main backgrounds common to both $t\bar{t}$ pair production and the resonance production are electroweak W boson production accompanied by four or more jets (W+jets) and QCD multi-jet (in short QCD) events where an isolated electron or muon is faked by leptons coming from a semileptonic b or c quark decays where the rest of the jet is not reconstructed. Also, $t\bar{t} \rightarrow l\bar{l}$+jets and single top production are considered as

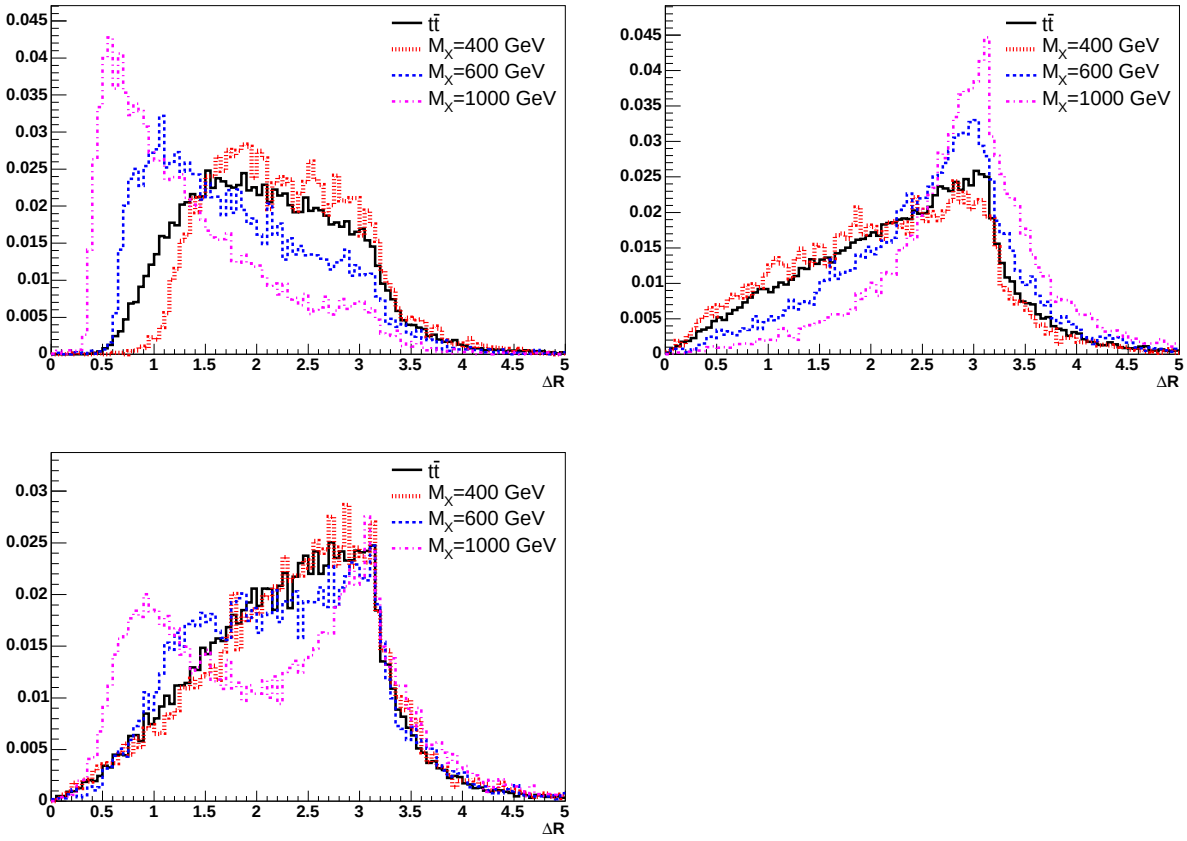

Figure 6.4: Distance in ΔR in $\eta \times \phi$ space between the quarks from the top-quark decays shown as a comparison between $t\bar{t}$ and X$\rightarrow t\bar{t}$ for three different resonance masses. The different plots from top left to bottom are: ΔR between the two light quarks from the W boson, ΔR between the two b quarks, and ΔR between a light and a b quark

sample	e+jets	μ+jets
$t\bar{t}$ $\rightarrow l$+jets	57.02 ± 0.48	56.10 ± 0.48
350 GeV X$\rightarrow t\bar{t}$	54.67 ± 0.96	53.57 ± 0.96
400 GeV X$\rightarrow t\bar{t}$	55.22 ± 0.86	54.23 ± 0.91
450 GeV X$\rightarrow t\bar{t}$	56.14 ± 0.79	55.64 ± 0.82
500 GeV X$\rightarrow t\bar{t}$	57.08 ± 0.75	56.43 ± 0.77
550 GeV X$\rightarrow t\bar{t}$	57.75 ± 0.80	56.61 ± 0.82
600 GeV X$\rightarrow t\bar{t}$	56.96 ± 0.77	57.38 ± 0.78
650 GeV X$\rightarrow t\bar{t}$	58.27 ± 0.78	57.26 ± 0.80
750 GeV X$\rightarrow t\bar{t}$	58.51 ± 0.84	58.14 ± 0.85
850 GeV X$\rightarrow t\bar{t}$	57.85 ± 0.91	57.25 ± 0.87
1000 GeV X$\rightarrow t\bar{t}$	56.99 ± 0.90	56.44 ± 0.87

Table 6.7: b-tagging efficiencies in the e+jets and μ+jets channel for SM $t\bar{t}$ $\rightarrow l$+jets and X$\rightarrow t\bar{t}$ for the ten different resonance masses.

background sources in this analysis. In contrast to usual analyses in top quark physics, here the SM $t\bar{t}$ pair production itself is the largest background when searching for a $t\bar{t}$ resonance.

6.2.1 Estimation of QCD-multijet Background

The normalization of the QCD-multijet background is estimated from data using the matrix method [88]. Two samples of events, a loose and a tight set, are needed where the latter is a subset of the first. The loose set (containing N_ℓ events) corresponds to the preselected sample without the tight cut. The tight sample (containing N_t events) requires in addition a likelihood cut in the e+jets channel and a tight muon isolation in the μ+jets channel. The number of events with a real lepton originating from a W+jets or a top event, i.e. $t\bar{t}$ $\rightarrow l$+jets , $t\bar{t}$ $\rightarrow l\bar{l}$+jets or singletop, is N^{W+top}, the number of events with a fake lepton is N^{QCD}. Then N_ℓ and N_t can be written as:

$$\begin{aligned} N_\ell &= N^{W+top} + N^{QCD} \\ N_t &= \varepsilon_{sig} N^{W+top} + \varepsilon_{QCD} N^{QCD} \end{aligned} \tag{6.1}$$

Solving this linear system for N^{QCD} and N^{W+top} yields:

$$N^{W+top} = \frac{N_t - \varepsilon_{QCD} N_\ell}{\varepsilon_{sig} - \varepsilon_{QCD}} \quad \text{and} \quad N^{QCD} = \frac{\varepsilon_{sig} N_\ell - N_t}{\varepsilon_{sig} - \varepsilon_{QCD}} \tag{6.2}$$

ε_{QCD} is the rate at which fake electrons (in the e+jets channel) or non-isolated muons (in the μ+jets channel) pass the corresponding tight cuts and is taken from data. The efficiency for a real lepton, ε_{sig}, is derived from Monte Carlo. The values for ε_{QCD} and ε_{sig} were obtained for each trigger list version v8–v13 separately. In Table 6.8 the luminosity weighted values are shown for both the e+jets and the μ+jets channel. The procedure to derive them can be found in Ref. [87] and Ref. [62].

Channel	ϵ_{QCD}	ϵ_{sig}
e+jets	0.170 ± 0.022	0.812 ± 0.006
μ+jets	0.083 ± 0.057	0.827 ± 0.005

Table 6.8: Efficiencies for the tight selection in both channels.

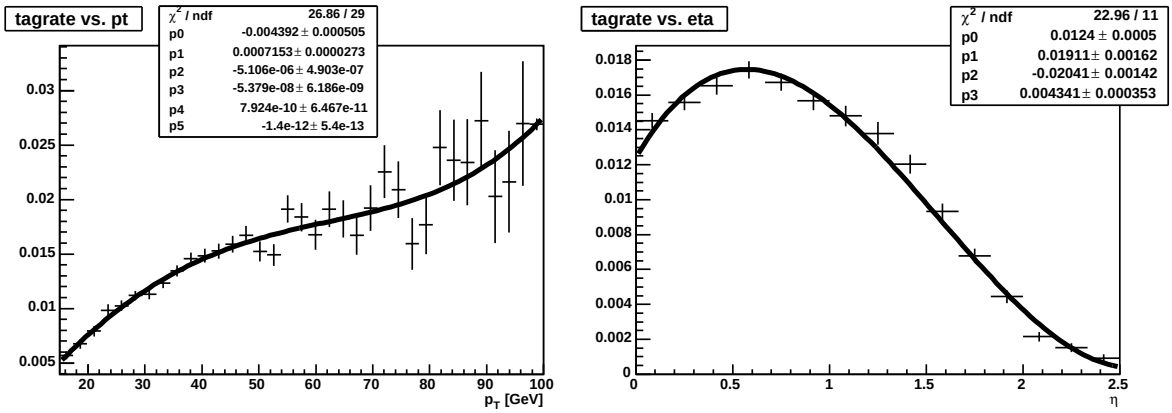

Figure 6.5: Tag rate functions for the QCD background derived from the e+jets dataset: versus jet p_T on the left and versus detector η on the right.

The shape of the QCD background obtained from the predicted number of QCD events suffers from low statistics. Therefore, the shape is derived from a sample enriched in QCD events. This sample is obtained by reversing the tight criteria of the lepton selection on the untagged sample, i.e. the sample before applying the b-tag, which is chosen due to larger statistics. Thus, the sample consists of untagged events, which pass the loose but not the tight preselection. From this untagged QCD sample, the expected $t\bar{t}$ contribution is subtracted bin by bin assuming $\sigma_{t\bar{t}} = 6.77$ pb. The remaining events are then weighted to account for the b-tag using tag rate functions. These tag rate functions are derived from the e+jets dataset using almost the same preselection as for the e+jets signal sample. The following differences in the selection ensure that dominantly QCD events are selected:

- only events with less than four jets are used,
- the cuts on $\not\!\!E_T$ and $\Delta\phi(e, \not\!\!E_T)$ are removed,
- the cut on the electron likelihood is reversed.

The derived tag rate functions which are parameterized in p_T and detector η are shown in Figure 6.5 and are applied on the untagged sample in both e+jets and μ+jets channel. A shape comparison between the tagged QCD events and the modified untagged QCD events can be seen in Figure 6.6, showing good agreement within the limited statistics.

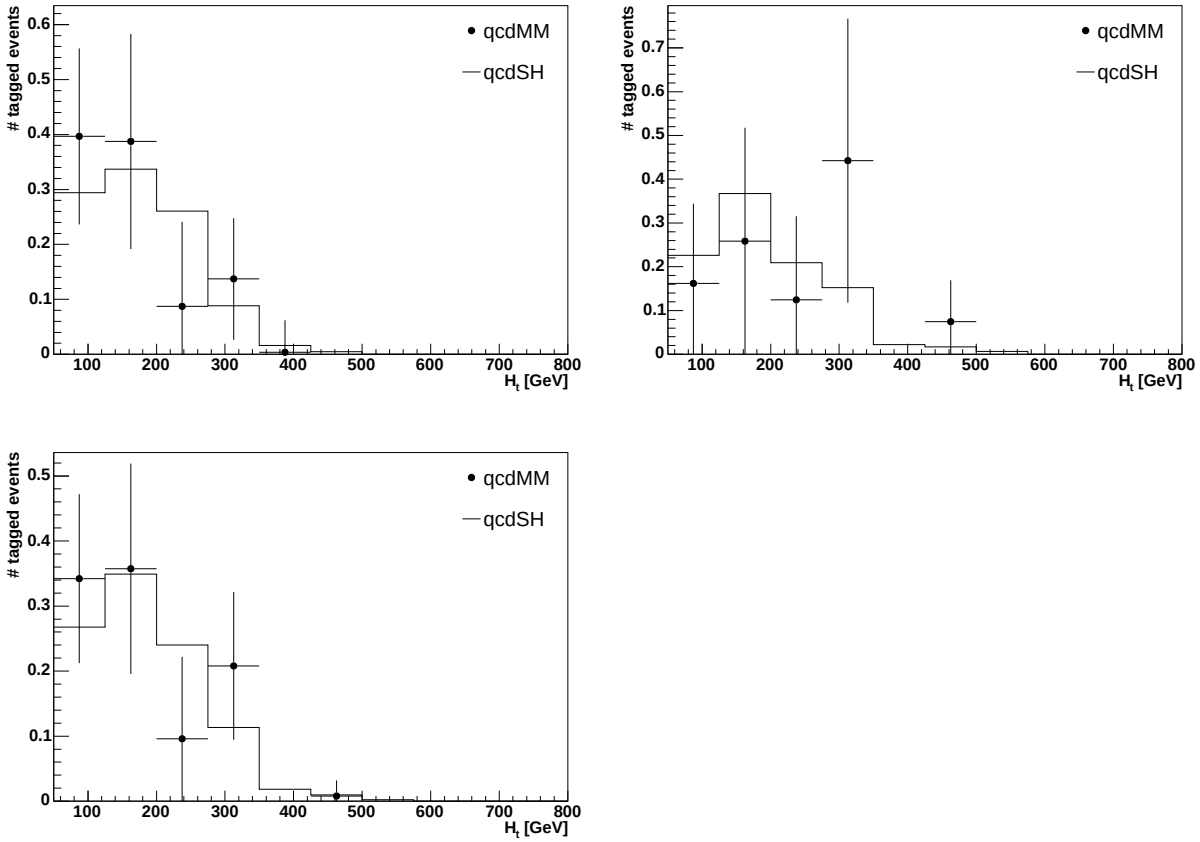

Figure 6.6: Shape comparison for the tagged QCD events from the matrix method (points with error bars (qcdMM)) and the shape derived from the untagged sample (open histogram (qcdSH)). The upper left plot shows H_t, the sum of the four leading jet E_t, in the e+jets channel, the upper right plot in the μ+jets channel, and the lower plot shows both channels combined.

6.2.2 W+jets Background

For the estimation of the W+jets background it could be expected to use the theoretical cross section for this process. Unfortunately, this is theoretically difficult and is not reliable for four additional jets, especially at next-to-leading order. Therefore, the normalization of the W+jets background is taken partly from data. The expected total number of untagged W+jets events is derived from the matrix method. Taking the event numbers of the untagged sample the matrix method is applied as described above. The $t\bar{t}$ contribution with the standard model predicted cross section of 6.77 pb is subtracted from this number. The number of W+jets events after b-tagging is then calculated as the product of the number of untagged W+jets events and the average tagging probability. The latter is obtained by combining the W+jets flavor fractions with the event tagging probability for each flavor. The event tagging probabilities for each flavor are shown in Table 6.9. More detailed information of the W+jets background estimation can be found in Ref. [74].

6.2.3 Top Background

The expected number of events after b-tagging is calculated assuming a standard model $t\bar{t}$ cross section of 6.77 ± 0.42 pb for the $t\bar{t} \rightarrow l$+jets and $t\bar{t} \rightarrow l\bar{l}$ backgrounds. This represents the currently best NNLO estimate on the $t\bar{t}$ cross section [14]. For single top production a cross section of 1.98 ± 0.23 pb [18] was assumed to calculate the expected number of events for this background source. Since the efficiency of some cuts on the electron or muon is different in data and in Monte Carlo, as already mentioned in Sect. 4, MC-to-data correction factors are derived from $Z \rightarrow ee$, respectively $Z \rightarrow \mu\mu$ events, as described in Ref. [87] and Ref. [62]. The MC-to-data correction factors are summarized in Table 6.10 and were applied to all Monte Carlo samples. The number of expected events for all different background sources will be given in Sect. 6.4.

	tagging probability in %	
	e+jets	μ+jets
$Wjjjj$	1.00 ± 0.10	1.11 ± 0.10
$Wcjjj$	8.14 ± 0.48	8.53 ± 0.51
$W(bb)Jjj$	33.83 ± 4.01	34.72 ± 3.89
$W(cc)Jjj$	7.56 ± 1.35	9.35 ± 1.45
$WbbJj$	46.03 ± 2.85	46.14 ± 2.90
$WccJj$	12.24 ± 1.05	13.34 ± 1.08

Table 6.9: Tagging probabilities for W+jets events with different flavor composition in the e+jets and μ+jets channel.

e+jets		μ+jets	
$\kappa_{electronreco,ID}$	0.996	$\kappa_{\mu\ ID\times\ acc\times\ cosmic\ veto}$	1.000
$\kappa_{electrontrackmatch}$	0.984	$\kappa_{\mu\ track}$	0.988
$\kappa_{electronlikelihood}$	0.910	$\kappa_{\chi^2_{trk}<4}$	0.983
		$\kappa_{\lvert dca\rvert/\sigma_{dca}<3}$	0.997
		$\kappa_{\mathrm{Rat11<0.08\ and\ RatTrk<0.06}}$	0.985
κ_{PV}	1.004	κ_{PV}	0.991
$\kappa_{\lvert\Delta z(e,PV)\rvert<1\ \mathrm{cm}}$	0.997	$\kappa_{\lvert\Delta z(\mu,PV)\rvert<1\ \mathrm{cm}}$	0.998

Table 6.10: MC-to-data correction factors for the e+jets channel (see Ref. [87]) and the μ+jets channel (see Ref. [62]).

6.3 Reconstruction of the $t\bar{t}$ Invariant Mass

The invariant mass of the $t\bar{t}$ system is reconstructed using the four-vectors of the $t\bar{t}$ decay products. These are combined using a constraint kinematic fit which is based on the SQUAW [89] algorithm and has already been used successfully in the top mass measurements of Run I [88] and Run II [90]. The kinematic fit works as described in Ref. [91] and is implemented in a package called `HitFit`.

Given a set of measured four-vectors $\vec{x}^m$, `HitFit` looks for the smallest changes on the fitted four-vectors $\vec{x}$ to satisfy a given set of constraints. This translates into minimizing a χ^2 defined as:

$$\chi^2 = (\vec{x} - \vec{x}^m)^T \mathbf{G} (\vec{x} - \vec{x}^m), \tag{6.3}$$

where $\mathbf{G}$ is the inverse error matrix, which is diagonal since the input vectors are transformed such that their errors are uncorrelated. The following constraints are used in the fit:

- two jets must form the invariant mass of the W boson ($M_W = 80.4$ GeV),
- the lepton and the $\not\!\!E_T$ must form the invariant mass of the W boson,
- the masses of the two reconstructed top quarks have to be equal, and
- the top mass is set to 175 GeV.

The top mass can be set to the approximated world average value since no measurement of the top mass is performed in this analysis. The constraint on the top mass also improves the resolution of the reconstructed $t\bar{t}$ invariant mass. If the kinematic fit does not converge, this fit is discarded.

For the jets and the charged lepton the four-vectors can directly be measured in the detector, but for the neutrino the only information is the transverse momentum which is taken to be the missing transverse energy, $\not\!\!E_T$. To fully reconstruct the neutrino also the longitudinal component of the neutrino momentum, p_z^ν, needs to be known. Therefore,

the p_z of the neutrino is the only kinematic unknown of the event. To solve this problem and to calculate the neutrino p_z^ν component, it is taken advantage of the fact that both top-quarks have to have to same mass:

$$\begin{aligned} 0 &= [(p_z^c)^2 - (E^c)^2](p_z^\nu)^2 + \alpha p_z^c p_z^\nu - (E^c p_T^\nu)^2 + \frac{\alpha^2}{4} \qquad \text{with} \\ \alpha &= m_t^2 - m_c^2 + 2\vec{p}_T^{\,\nu} \cdot \vec{p}_T^{\,c} \end{aligned} \tag{6.4}$$

where c is the sum of the four-vectors of the lepton and the b-jet. This equation leeds to two possible solutions for p_z^ν which both are tried as starting values in the fit and the one leading to the lower χ^2 solution is kept.

The kinematic fit is performed for each set of jet-parton assignments since it is not known which jet came from which parton. This leads to $4! = 24$ possible permutations, but since there is no need to distinguish between the two jets coming from the hadronically decaying W boson, the number can be reduced to 12. When more than four jets are reconstructed in the event, only the four highest p_T jets are considered in the fit. The correct treatment of initial and final state radiation would lead to an increased number of jet-parton combinations which would complicate the analysis.

Out of the 12 permutations only one has the right jet-parton assignment. The permutation with the highest probability P is chosen to be the correct solution in this analysis. Two different methods to calculate this probability are used:

- **Plain:** The permutation with the lowest χ^2 value and thus the highest χ^2 probability is chosen.
$$P = P(\chi^2) \tag{6.5}$$

- **SVT:** It is taken advantage of the b-tagging information. The χ^2 probability of each permutation is multiplied with the probability that the jet assigned to be the b-jet in the permutation is tagged by the SVT algorithm.

$$P = P(\chi^2) \cdot P_{b,SVX} \qquad \text{with} \quad P_{b,SVX} = \begin{cases} 1 & \text{if tagged jet is } \texttt{HitFit}\, b\,\text{jet} \\ 0 & \text{else} \end{cases} \tag{6.6}$$

While the jets in data are either tagged (weight of 1) or not (weight of 0), jets in Monte Carlo are weighted with the tagging probability, as described in Sect. 4.6.1. So in order to decide whether a jet assigned to be the b-jet in the permutation is tagged or not, the b-tagging probabilities on Monte Carlo need to be forced to 1 or 0. This is done by rolling the dice for each jet according to the actual b-tag weight. If a jet with a weight of 1 is chosen to be the b-jet in a given permutation, a weight of 1 is assigned to the permutation which is therfore kept, while in the other case a weight of 0 is assigned and the permutation is discarded. Thus, the knowledge of the tagged jet reduces the number of possible permutations to a maximum of 6, and discards obviously wrong permutations. In the case of double tagged events, where both b-jets are identified, the number of possible permutations is reduced to 2. On

the other hand, when applying this method on an untagged sample, i.e. before b-tagging is applied, the full set of 12 permutations is taken into account and thus using the "Plain" method for events which cannot be tagged. With this method the number of correct solutions, i.e. the permutation where the assigned jets can be matched to the corresponding partons, is expected to be higher compared to the "Plain" method.

6.3.1 Fraction of correct Solutions

A parton to jet matching was performed on Monte Carlo on the tagged samples to determine the fraction of correct solutions out of all possible permutations, when using the two different methods described above. The partons, i.e. the b, the $\bar{b}$, and the two quarks from the hadronic W boson decay, have to be separated by $\Delta R \geq 0.5$ and are matched to a jet within a cone of $\Delta R = 0.5$. For these unambiguously parton-matched events the correct permutation can be found and thus the fraction of correct solutions can be determined. These fractions are summarized for two different methods in Table 6.11 for the e+jets and μ+jets channel combined.

The fraction of correct solutions is about $12-15\%$ higher when making use of the SVT b-tagging information to choose the best permutation compared to the "Plain" method. The increase in correct solutions was expected since at least 6 wrong permutations are discarded in the "SVT" method from the beginning.

6.3.2 Convergence rate of the kinematical Fit

As mentioned above, fits which do not converge are discarded. If the constrained fits of all permutations of a preselected event do not converge, the event is taken out of the

sample	Plain	SVT
$t\bar{t} \rightarrow l$+jets	49.6 ± 0.4	62.1 ± 0.4
350 GeV X$\rightarrow t\bar{t}$	38.7 ± 0.8	52.3 ± 0.9
400 GeV X$\rightarrow t\bar{t}$	37.5 ± 0.8	50.4 ± 0.8
450 GeV X$\rightarrow t\bar{t}$	41.6 ± 0.7	54.2 ± 0.7
500 GeV X$\rightarrow t\bar{t}$	45.2 ± 0.7	58.2 ± 0.7
550 GeV X$\rightarrow t\bar{t}$	49.8 ± 0.7	61.6 ± 0.7
600 GeV X$\rightarrow t\bar{t}$	52.2 ± 0.7	64.5 ± 0.7
650 GeV X$\rightarrow t\bar{t}$	54.1 ± 0.7	66.6 ± 0.7
750 GeV X$\rightarrow t\bar{t}$	52.7 ± 0.8	66.4 ± 0.8
850 GeV X$\rightarrow t\bar{t}$	51.3 ± 0.9	65.6 ± 0.9
1000 GeV X$\rightarrow t\bar{t}$	47.0 ± 0.9	62.5 ± 1.0

Table 6.11: Fractions of correct solutions for the two different methods "Plain" and "SVT". Shown in the e+jets and μ+jets channel combined for SM $t\bar{t} \rightarrow l$+jets and X$\rightarrow t\bar{t}$ for the ten different resonance masses.

sample	e+jets	μ+jets
$t\bar{t} \rightarrow l$+jets	99.46 ± 1.30	98.82 ± 1.30
350 GeV X$\rightarrow t\bar{t}$	99.63 ± 2.59	99.73 ± 2.60
400 GeV X$\rightarrow t\bar{t}$	99.92 ± 2.35	99.69 ± 2.47
450 GeV X$\rightarrow t\bar{t}$	99.79 ± 2.16	99.37 ± 2.23
500 GeV X$\rightarrow t\bar{t}$	99.73 ± 2.04	98.58 ± 2.07
550 GeV X$\rightarrow t\bar{t}$	98.89 ± 2.18	97.85 ± 2.20
600 GeV X$\rightarrow t\bar{t}$	98.57 ± 2.07	96.78 ± 2.06
650 GeV X$\rightarrow t\bar{t}$	97.29 ± 2.09	95.16 ± 2.07
750 GeV X$\rightarrow t\bar{t}$	93.94 ± 2.16	93.04 ± 2.13
850 GeV X$\rightarrow t\bar{t}$	88.17 ± 2.14	86.71 ± 2.01
1000 GeV X$\rightarrow t\bar{t}$	81.72 ± 1.92	80.74 ± 1.83

Table 6.12: Fractions for at least one converged fit for all the 12 permutations. Shown in the e+jets and μ+jets channel for SM $t\bar{t} \rightarrow l$+jets and X$\rightarrow t\bar{t}$ for the ten different resonance masses.

dataset. The fraction for which at least one jet combination out of the possible 12 has a converged fit is summarized in Table 6.12 for $t\bar{t} \rightarrow l$+jets and X$\rightarrow t\bar{t}$ Monte Carlo samples.

As can be seen, the fraction of at least one converged fit per event is very high for the $t\bar{t}$ sample and for the low mass resonance samples. But for high resonance masses, starting at 600 GeV, the efficiency decreases significantly. For a sample of 1000 GeV the convergence fraction is only around 80%. One of the reasons for the decreasing convergence fraction is the fact that the minimal distance in ΔR between the quarks gets smaller the larger the resonance mass, as was already shown in Fig. 6.3. This leads to a lower jet-multiplicity for higher masses, since two quarks can be reconstructed in the same jet. In this case the fourth jet which is needed in the kinematic fit may in fact come from a gluon. Having one jet with the mass of two quarks and a gluon jet, the $t\bar{t}$ hypothesis cannot be fulfilled.

When using the SVT information to choose the best solution the number of possible permutations is reduced to a maximum of 6, since all permutations where the tagged jet does not correspond to a b-jet in the permutation are discarded. Correspondingly the convergence rate goes down significantly due to fewer option, as can be seen in Table 6.13, but the general observations when comparing the rates for different samples are the same as mentioned above.

6.3.3 Mass Resolution

Figure 6.7 shows the $t\bar{t}$ invariant mass, $M_{t\bar{t}}$, distributions for SM $t\bar{t} \rightarrow l$+jets obtained from `HitFit` using the "Plain" and the "SVT" method to choose the correct solution. Also, the $t\bar{t}$ invariant mass distribution obtained from parton level information, i.e. reconstructed from the initial quarks, the charged lepton, and the neutrino, is shown for

sample	e+jets	μ+jets
$t\bar{t} \rightarrow l$+jets	94.42 ± 1.25	93.87 ± 1.25
350 GeV X$\rightarrow t\bar{t}$	94.07 ± 2.48	94.64 ± 2.50
400 GeV X$\rightarrow t\bar{t}$	93.66 ± 2.23	93.77 ± 2.36
450 GeV X$\rightarrow t\bar{t}$	93.56 ± 2.06	93.33 ± 2.13
500 GeV X$\rightarrow t\bar{t}$	93.28 ± 1.94	91.42 ± 1.95
550 GeV X$\rightarrow t\bar{t}$	91.71 ± 2.06	90.25 ± 2.07
600 GeV X$\rightarrow t\bar{t}$	90.89 ± 1.95	88.98 ± 1.94
650 GeV X$\rightarrow t\bar{t}$	88.95 ± 1.96	86.54 ± 1.93
750 GeV X$\rightarrow t\bar{t}$	82.26 ± 1.96	81.58 ± 1.94
850 GeV X$\rightarrow t\bar{t}$	75.04 ± 1.91	74.22 ± 1.80
1000 GeV X$\rightarrow t\bar{t}$	66.71 ± 1.67	65.64 ± 1.58

Table 6.13: Fractions for at least one converged fit for the maximum of 6 permutations when using SVT information. Shown in the e+jets and μ+jets channel for SM $t\bar{t} \rightarrow l$+jets and X$\rightarrow t\bar{t}$ for the ten different resonance masses.

comparison in this figure. In addition the difference between the invariant mass at parton level and the one coming from `HitFit` is shown for both methods. The distributions reconstructed with `HitFit` agree in shape with the distribution at parton level. When comparing the two methods, "plain" and "SVT", to choose the correct solution it can be seen that they agree in shape of the $M_{t\bar{t}}$ distribution. But although the "SVT" method is slightly better in obtaining the correct mass given at parton level by having a mean value closer to 0 and a slightly smaller RMS, no general improvement in the mass resolution could be achieved.

In Figures 6.8-6.10, the $t\bar{t}$ invariant mass distributions from `HitFit` can be seen for the different resonance masses. Since the "SVT" method showed a slightly better performance when finding the correct mass than the "Plain" method, $M_{t\bar{t}}$ is only shown for the "SVT" method to choose the best permutation. For the higher resonance mass samples a tail in the $M_{t\bar{t}}$ distribution towards lower masses can be seen at parton level. This is due to the influence of the PDFs which prefer the lower mass regions. In the distributions obtained from `HitFit` it can be seen that the mass resolution gets worse for higher resonance masses. One of the reasons for this behavior is the lower jet-multiplicity with the consequences described in Sect. 6.1.1. In order to study this behavior, further checks were made. In Figures 6.11 and 6.12, the reconstructed masses of the W boson and the top quark are shown for resonance masses of 400 GeV and 1000 GeV. These invariant masses are reconstructed only for events where the quarks at the parton level are separated by $\Delta R \geq 0.5$ and can unambiguously be matched to reconstructed jets within $\Delta R \leq 0.5$. This is the case in about 65% of $t\bar{t} \rightarrow l$+jets events and 59%, 61%, and 42% of events with the resonance mass of 400 GeV, 600 GeV, and 1000 GeV, respectively. The invariant mass is then formed from the reconstructed jets, the lepton and $\not\!\!E_T$ without using `HitFit`. For the 1000 GeV sample, it can already be seen that at the reconstruction level the $M_{t\bar{t}}$ distribution widens mainly due to the poor resolution for

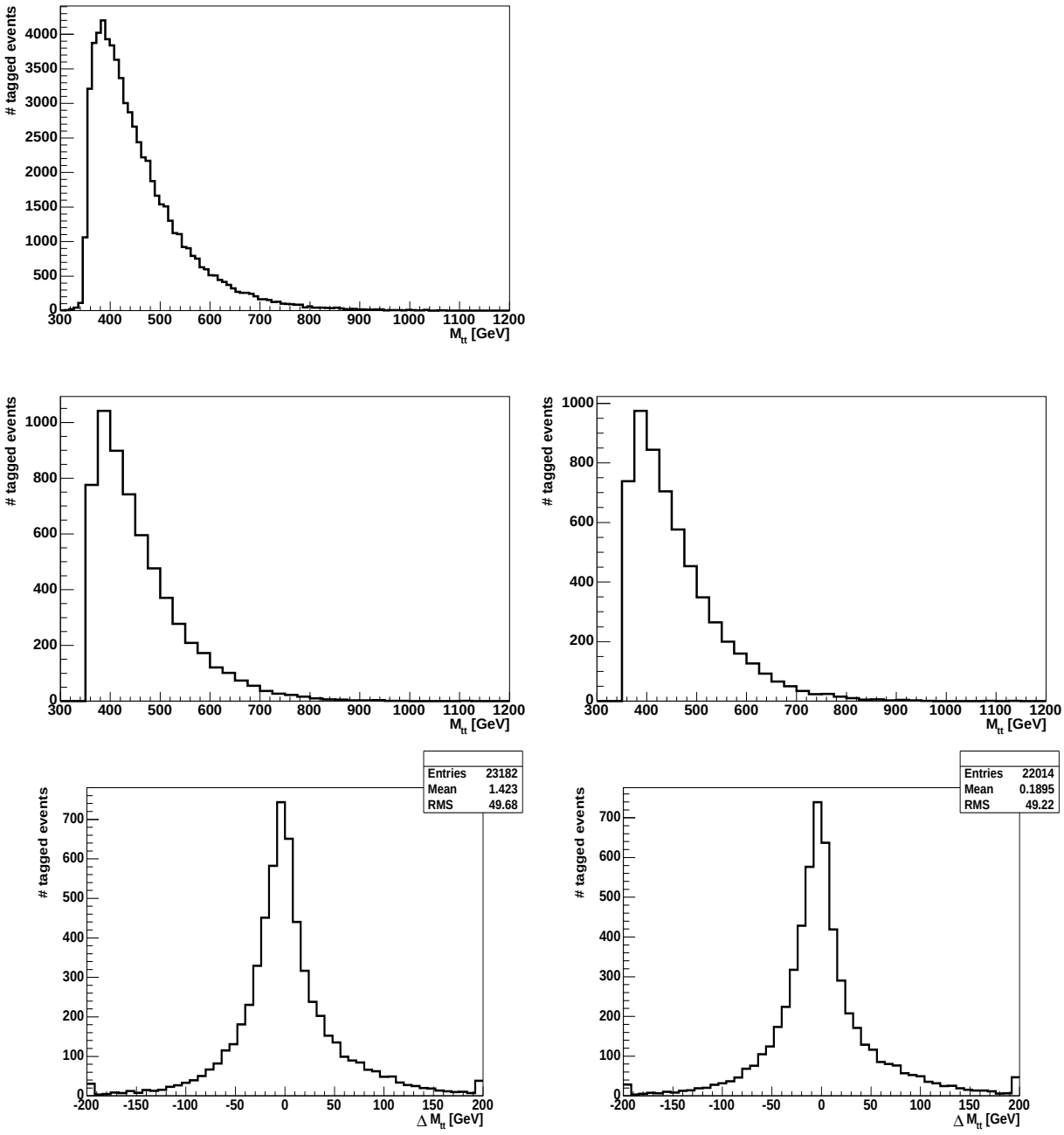

Figure 6.7: Comparison of the $t\bar{t}$ invariant mass for SM $t\bar{t} \rightarrow l$+jets . In the upper plot, the shape of $M_{t\bar{t}}$ can be seen using only the parton information. In the middle left plot, $M_{t\bar{t}}$ coming from `HitFit` using the "Plain" method is shown after all selection cuts in e+jets and μ+jets channel combined. The middle right plot shows the same distribution but using the "SVT" method to chose the solution from `HitFit`. The lower plots show the difference between $M_{t\bar{t}}$ at parton level and reconstructed with `HitFit` for the "Plain" method on the left and the "SVT" method on the right.

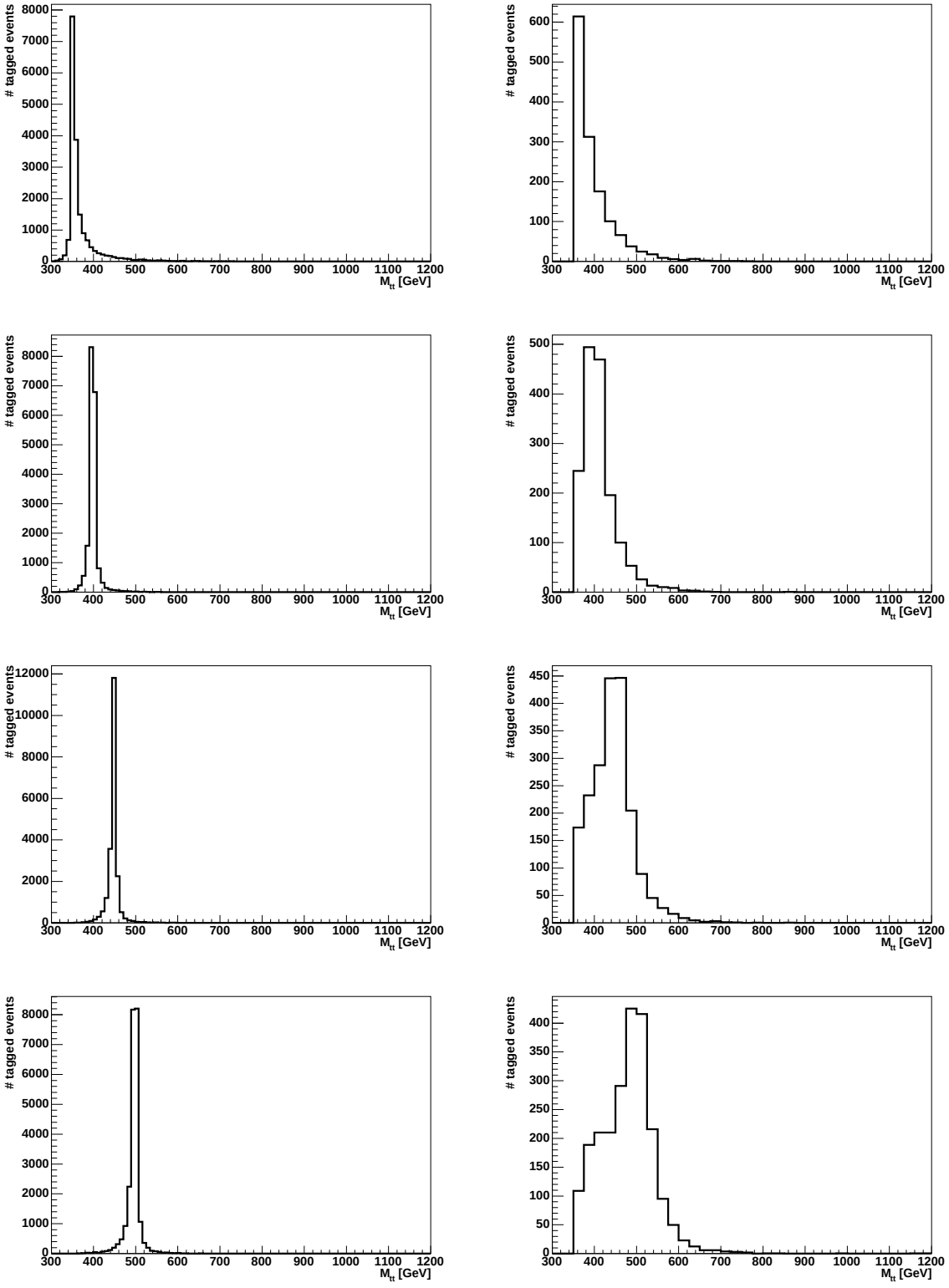

Figure 6.8: Comparison of the $t\bar{t}$ invariant mass. In the left plots, the shape of $M_{t\bar{t}}$ can be seen using only the parton information and in the right plots, $M_{t\bar{t}}$ coming from `HitFit` is shown for the "SVT" method after all selection cuts in e+jets and μ+jets channel combined. The different resonance masses are from top to bottom: 350 GeV, 400 GeV, 450 GeV and 500 GeV.

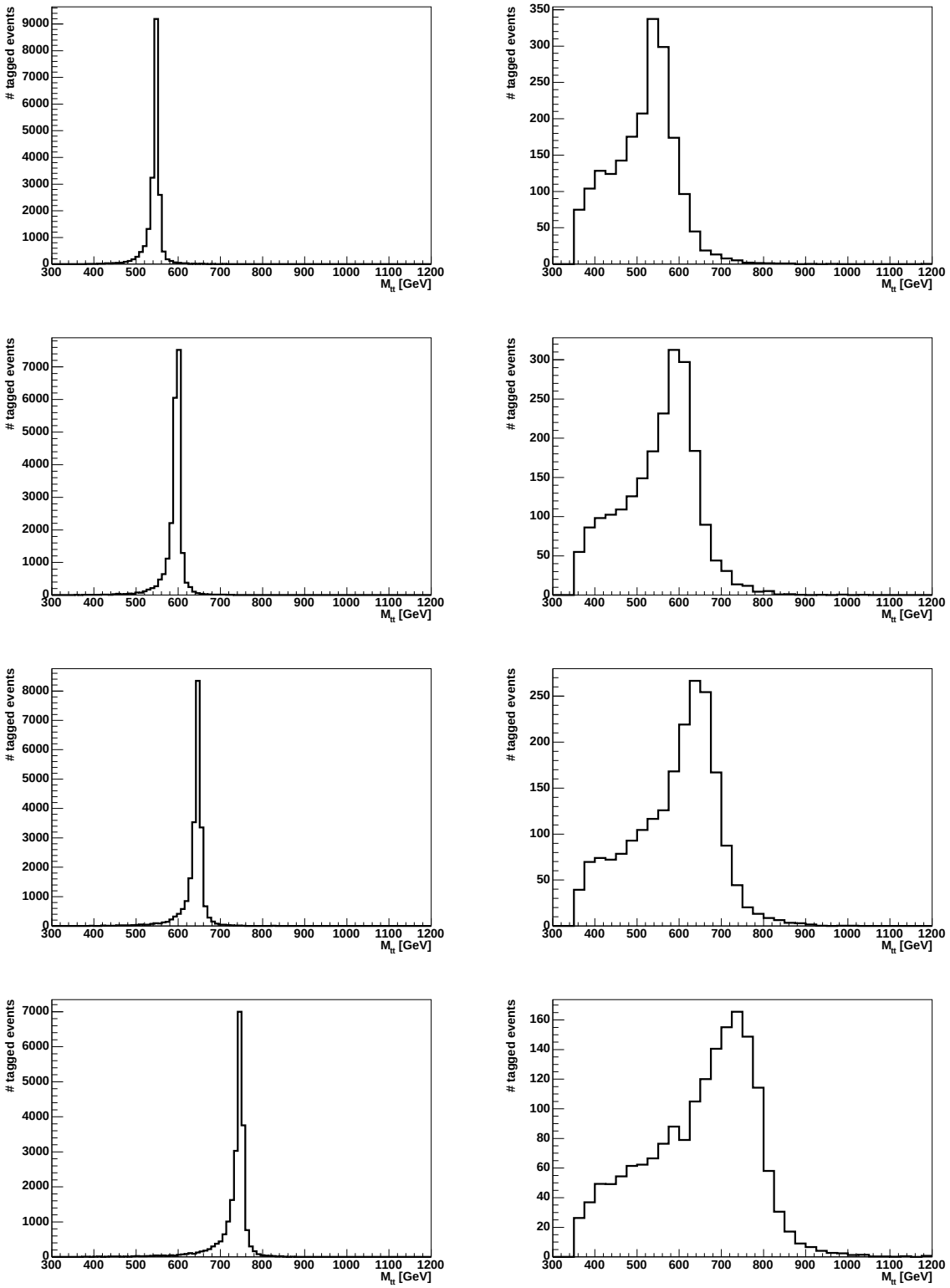

Figure 6.9: Comparison of the $t\bar{t}$ invariant mass. In the left plots, the shape of $M_{t\bar{t}}$ can be seen using only the parton information and in the right plots, $M_{t\bar{t}}$ coming from `HitFit` is shown for the "SVT" method after all selection cuts in e+jets and μ+jets channel combined. The different resonance masses are from top to bottom: 550 GeV, 600 GeV, 650 GeV and 750 GeV.

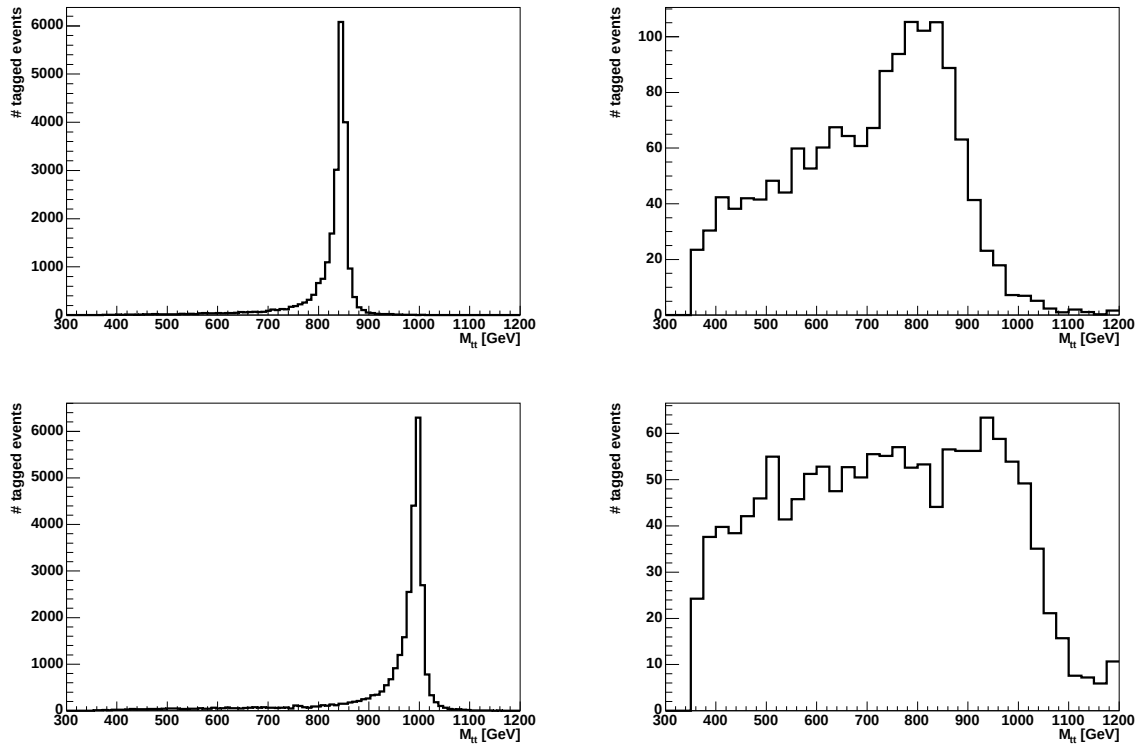

Figure 6.10: Comparison of the $t\bar{t}$ invariant mass. In the left plots, the shape of $M_{t\bar{t}}$ can be seen using only the parton information and in the right plots, $M_{t\bar{t}}$ coming from `HitFit` is shown for the "SVT" method after all selection cuts in e+jets and μ+jets channel combined. The different resonance masses are from top to bottom: 850 GeV and 1000 GeV.

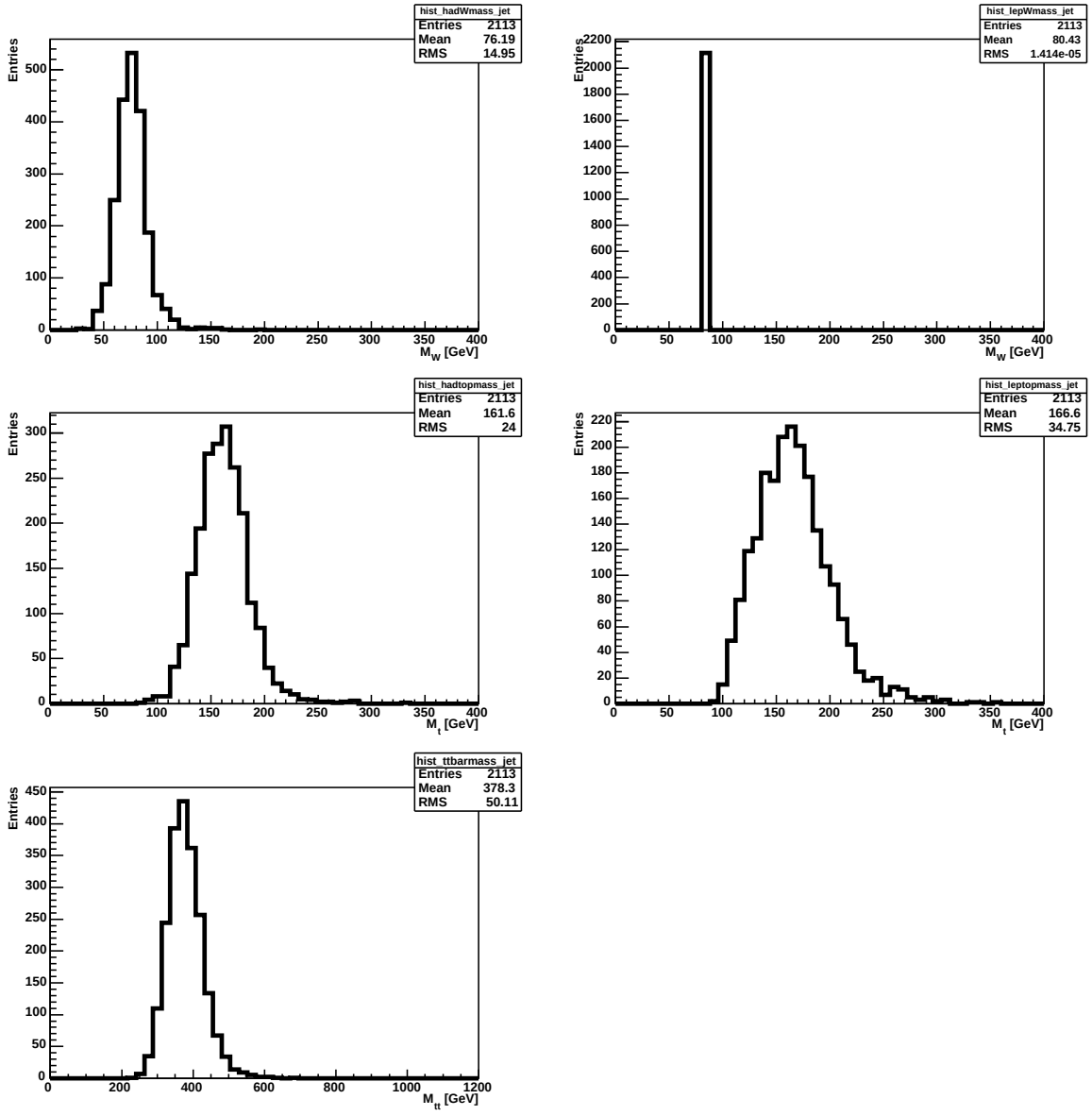

Figure 6.11: Invariant masses reconstructed for the 400 GeV resonance sample. In the upper plots M_W for the hadronically (on the left) and the leptonically (on the right) decaying W boson can be seen. In the middle plots, the corresponding M_t distribution is shown where the W boson from above is combined with the correct b-quark. The lower plot shows the resulting $M_{t\bar{t}}$. These plots are made only from reconstructed jets without `HitFit` and only those events where the quarks are separated by $\Delta R \geq 0.5$ and can be matched unambiguously to jets.

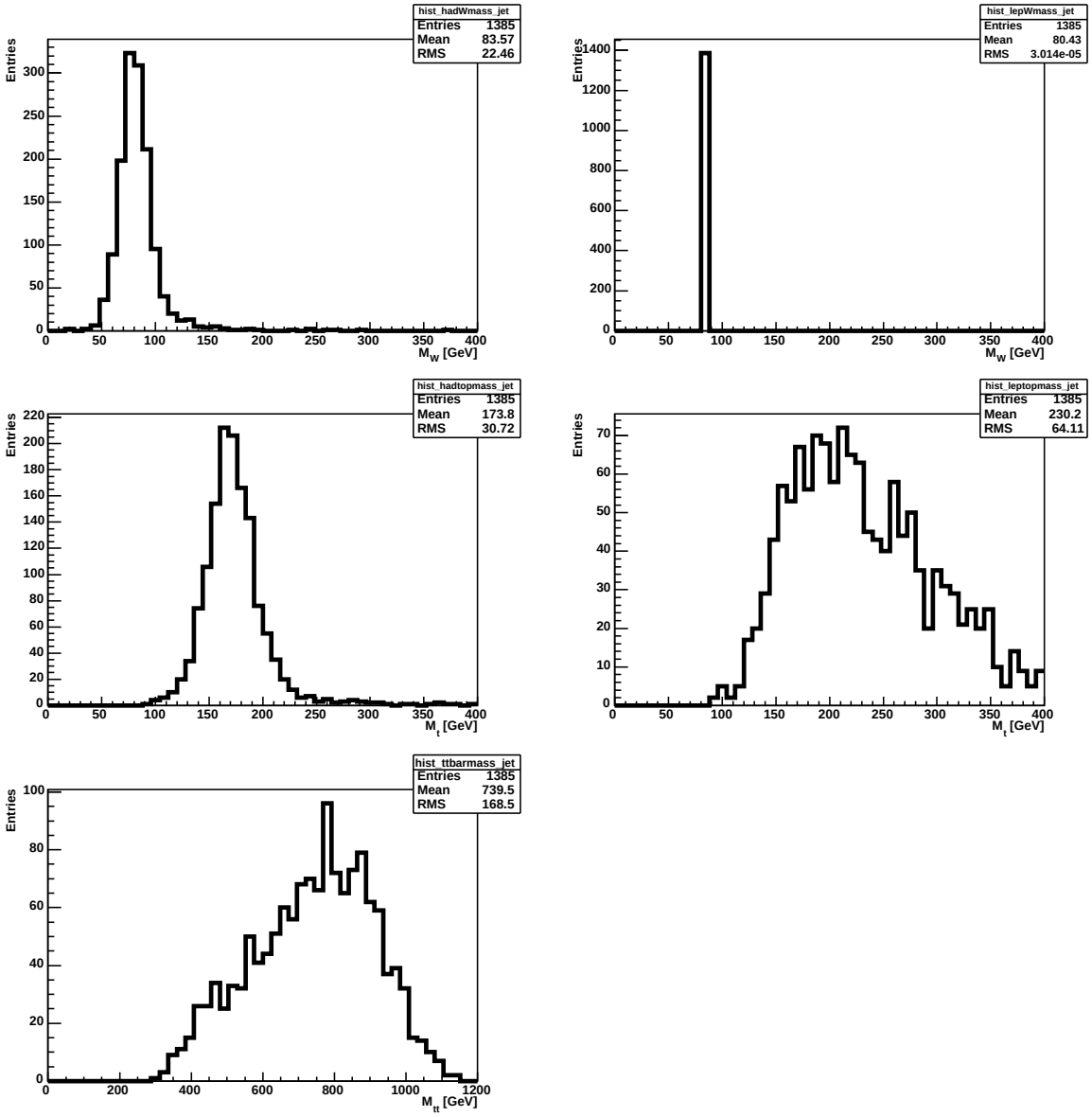

Figure 6.12: Invariant masses reconstructed for the 1000 GeV resonance sample. In the upper plots M_W for the hadronically (on the left) and the leptonically (on the right) decaying W boson can be seen. In the middle plots, the corresponding M_t distribution is shown where the W boson from above is combined with the correct b-quark. The lower plot shows the resulting $M_{t\bar{t}}$. These plots are made only from reconstructed jets without `HitFit` and only those events where the quarks are separated by $\Delta R \geq 0.5$ and can be matched unambiguously to jets.

the leptonically decaying W boson. This can be explained by a bad $\not\!\!E_T$ resolution since $\sigma_{\not\!\!E_T}$ is proportional to $\sqrt{scalar E_T}$ and a lower fraction of correct ν solutions. Also, it can be seen that the tail towards lower masses present at parton level is amplified due to the fact that the chance of having the four quarks separated by $\Delta R \geq 0.5$ is higher for lower masses.

6.4 Expected Number of Events

Due to the different convergence rates for the two methods to choose the correct solution from `HitFit`, the number of expected events for the background sources and for data are different for each method. Therefore, the numbers which were derived with the procedures described in Sect. 6.2, are presented here for both methods.

The number of loose and tight events which are needed for the Matrix Method to estimate the QCD and W+jets background can be found in Table 6.14 before and after applying the b-tagging. Applying the Matrix Method on tagged data events results in the following prediction for the number of tagged QCD events:

- "Plain": $N_{QCD} = 4.08 \pm 1.32$ in the e+jets channel
  $N_{QCD} = 1.23 \pm 0.64$ in the μ+jets channel
- "SVT": $N_{QCD} = 3.85 \pm 1.26$ in the e+jets channel
  $N_{QCD} = 0.81 \pm 0.55$ in the μ+jets channel

Applying the Matrix Method on untagged data events the following number of events for $t\bar{t}$ +W and W+jets in the untagged sample are obtained:

- "Plain": $N_{W+top} = 212.2 \pm 18.1$ in the e+jets channel
  $N^{untagged}_{W \geq 4jets} = 155.3 \pm 18.1$

  $N_{W+top} = 210.7 \pm 16.1$ in the μ+jets channel
  $N^{untagged}_{W \geq 4jets} = 152.5 \pm 16.1$
- "SVT": $N_{W+top} = 212.9 \pm 17.9$ in the e+jets channel
  $N^{untagged}_{W \geq 4jets} = 159.1 \pm 17.9$

  $N_{W+top} = 210.4 \pm 15.9$ in the μ+jets channel
  $N^{untagged}_{W \geq 4jets} = 155.2 \pm 15.9$

The expected total number of tagged W+jets events is shown in Table 6.15 together with the individual values for each flavor. All expected background values can be found in Table 6.16. Both tables show the numbers for the "Plain" and the "SVT" method. It can be seen that the event numbers of the Standard Model expectation is smaller for the "SVT" method as is the number of observed events in data. A data – Monte Carlo comparison can be found in the Appendix.

		before b-tagging		after b-tagging	
Method	Channel	N_ℓ	N_t	N_ℓ	N_t
"PLAIN"	e+jets	602	270	88	56
	μ+jets	451	227	75	51
"SVT"	e+jets	575	266	82	52
	μ+jets	430	225	68	49

Table 6.14: Observed data events for the loose and tight preselection before and after b-tagging as input for the matrix method shown for the "Plain" and "SVT" method.

	"Plain"		"SVT"	
	e+jets	μ+jets	e+jets	μ+jets
$Wjjjj$	1.32 ± 0.07	1.29 ± 0.11	1.28 ± 0.07	1.25 ± 0.06
$Wcjjj$	0.63 ± 0.03	0.62 ± 0.03	0.65 ± 0.03	0.63 ± 0.03
$W(bb)Jjj$	1.51 ± 0.13	1.48 ± 0.12	1.54 ± 0.14	1.50 ± 0.14
$W(cc)Jjj$	0.66 ± 0.09	0.64 ± 0.08	0.69 ± 0.10	0.67 ± 0.08
$WbbJj$	2.04 ± 0.10	2.01 ± 0.09	2.08 ± 0.10	2.03 ± 0.10
$WccJj$	0.90 ± 0.06	0.88 ± 0.05	0.92 ± 0.06	0.90 ± 0.06
W+jets	7.06 ± 0.21	6.93 ± 0.21	7.15 ± 0.22	6.98 ± 0.21

Table 6.15: Predicted number of tagged W+jets events for both methods and for e+jets and μ+jets channel separately.

	"Plain"		"SVT"	
	e+jets	μ+jets	e+jets	μ+jets
W+jets	7.06 ± 0.21	6.93 ± 0.21	7.15 ± 0.22	6.98 ± 0.21
QCD	4.08 ± 1.32	1.23 ± 0.64	3.85 ± 1.26	0.81 ± 0.55
single top	0.66 ± 0.03	0.61 ± 0.03	0.56 ± 0.03	0.55 ± 0.03
$t\bar{t} \rightarrow l\bar{l}$+jets	0.65 ± 0.03	0.60 ± 0.03	0.61 ± 0.03	0.54 ± 0.03
$t\bar{t} \rightarrow l$+jets	30.96 ± 0.30	31.29 ± 0.31	29.33 ± 0.29	29.65 ± 0.30
total	43.41 ± 1.37	40.65 ± 0.74	41.49 ± 1.31	38.52 ± 0.66
observed	56	51	52	49

Table 6.16: Predicted and observed number of tagged events for both methods in the e+jets and μ+jets channels. Errors are statistical only.

6.5 Systematic Uncertainties

The measurement of the $t\bar{t}$ invariant mass requires the shape of the distribution and the overall normalization. Both are affected by systematic uncertainties. To correctly normalize the Monte Carlo samples the MC-to-data correction factors, the cross sections and the luminosity are used which have been already explained before and whose uncertainties can be found in Table 6.17. The change in the total number of events for the Standard Model background when varying these factors up and down can be seen in Table 6.18. The relative change due to the uncertainties of the normalization factors is independent of the method to choose the correct solution of `HitFit`.

Other dominant uncertainties are the ones which potentially change the shape of the distribution in addition to the normalization. The following systematic effects of this kind have been studied on all samples:

- **Uncertainty associated to the jet energy scale (JES)**
  The effect of the JES uncertainty on the shape of the invariant mass distribution is obtained by varying the JES by $\pm 1\sigma$,where, conservatively,

  $$\sigma = \sqrt{\sigma^2_{stat,data} + \sigma^2_{syst,data} + \sigma^2_{stat,MC} + \sigma^2_{syst,MC}} \tag{6.7}$$

  The individual terms are the statistical and systematic uncertainties on the JES in data and in Monte Carlo. This variation was used everywhere except for the kinematic fit where a reduced JES variation of $\pm 5\%$ is applied internally inside `HitFit`.

- **Uncertainty associated to the jet reconstruction and identification efficiency (JetID)**
  As described in Sect. 4.5.3, the jet reconstruction and identification efficiency in Monte Carlo is higher than in data and a p_T-dependent data-MC correction factor had to be applied. The systematic uncertainty arises from the accuracy with which this correction factor is known, which is then varied by $\pm 1\sigma$. The impact on the preselection efficiency is taken into account.

- **Uncertainty associated to the jet energy resolution (JER)**
  As described in Sect. 4.5.5, the jet energy are smeared in Monte Carlo to match the resolution measured in data. The parameters of the jet energy smearing are varied by the size of their uncertainty [55]. The effect on the preselection efficiency is taken into account.

- **Uncertainty associated to the top quark mass**
  The mass of the top quark enters into the kinematic fit `HitFit` as a constraint ($m_{top} = 175$ GeV) and can influence the shape of the $M_{t\bar{t}}$ distribution. In addition it changes the normalization due to different preselection efficiencies and different $\sigma_{t\bar{t}}$ for different masses. To study the resulting systematic effect, $t\bar{t}$ MC samples with $m_{top} = 170$ GeV and $m_{top} = 180$ GeV have been used taking into account their different cross sections of 7.91 pb and 5.80 pb, respectively. Different masses

e+jets		μ+jets	
source	rel. uncertainty	source	rel. uncertainty
$\kappa_{electronreco,ID}$	$\pm 3\%$	$\kappa_{\mu\ ID\times\ acc\times\ cosmic\ veto}$	$\pm 4\%$
$\kappa_{electrontrackmatch}$	$\pm 0.7\%$	$\kappa_{\mu\ track}$	$\pm 3\%$
$\kappa_{electronlikelihood}$	$\pm 1.6\%$	$\kappa_{\chi^2_{trk}<4}$	$\pm 0.3\%$
		$\kappa_{\lvert dca\rvert/\sigma_{dca}<3}$	$\pm 0.2\%$
		$\kappa_{\text{Rat11}<0.08 \text{ and RatTrk}<0.06}$	$\pm 0.7\%$
κ_{PV}	$\pm 1.8\%$	κ_{PV}	$\pm 2.8\%$
$\kappa_{\lvert\Delta z(e,PV)\rvert<1\text{ cm}}$	$\pm 0.4\%$	$\kappa_{\lvert\Delta z(\mu,PV)\rvert<1\text{ cm}}$	$\pm 0.1\%$
$\sigma_{t\bar{t}}$	$\pm 6\%$	$\sigma_{t\bar{t}}$	$\pm 6\%$
$\sigma_{singletop}$	$\pm 12\%$	$\sigma_{singletop}$	$\pm 12\%$
Luminosity	$\pm 6.5\%$	Luminosity	$\pm 6.5\%$

Table 6.17: Relative systematic uncertainties on the normalization factors.

of the top quark will in the first instance not influence the $M_{t\bar{t}}$ distribution of the different resonance MC samples since the position of the resonance peak does not change with different top quark mass. The possible differences in the preselection efficiencies are assumed to be small and neglected due to the fact that no resonance MC samples with different top masses exist.

- **Uncertainty associated with the *b*-tag parameterizations**
  In Sect. 4.6.1 the different parameterizations were introduced which are needed to apply b-tagging on Monte Carlo. The parameterizations for the inclusive b-tag and c-tag efficiencies in MC, for semileptonic b-tag efficiencies in MC and data, as well as the negative tag rate have been varied by $\pm 1\sigma$ to estimate the systematic uncertainty due to these parameterizations.

- **Uncertainty associated with the flavor composition of the *W*+jets background**
  The fractions for the different flavor components of the W+jets background are estimated as described in Ref. [74]. From the different systematic uncertainties associated with this approach the uncertainties due to matching, higher order effects, heavy quark mass and the choice of the factorization scale are taken into account by propagating them to all W+jets fractions. In case of the uncertainty related to the factorization scale the factorization scale was varied by a factor of 2 up and down. The heavy quarks masses are varied by ± 0.3 GeV. Detailed information on this systematic effects can be found in Ref. [74].

- **Uncertainty associated with the modeling of the $t\bar{t}$ background**
  The nominal $t\bar{t}$ Monte Carlo includes only the $t\bar{t}$ LO matrix element and the

source	rel. sys. uncertainty (%)	
	σ^+	σ^-
MC-to-data correction factors in e+jets channel	+1.40	−1.40
MC-to-data correction factors in μ+jets channel	+2.05	−2.05
$\sigma_{t\bar{t}}$	+4.30	−4.30
$\sigma_{singletop}$	+0.16	−0.16
Luminosity	+4.60	−4.60

Table 6.18: The relative systematic change on the overall normalization of the standard model background from the uncertainties of the normalization factors.

radiation of additional jets is modeled by PYTHIA. To study the effect of extra jets, a separate sample including the extra radiation in the LO matrix element has been used. This sample is mixed with the nominal $t\bar{t}$ sample according to the relative cross section for the processes, 6 pb for $t\bar{t}$ and 2.5 pb for $t\bar{t}$ + j, to study this effect.

After taking into account the difference in the selection efficiency the fraction for the $t\bar{t}$ + jets sample is 35.4% in the e+jets channel and 33.5% in the μ+jets channel. When mixing these fractions of $t\bar{t}$ + j with the nominal $t\bar{t}$, a different shape of the $M_{t\bar{t}}$ distribution is obtained which is taken as the uncertainty of the $t\bar{t}$ modeling.

- **Uncertainty on ϵ_{QCD}**
  The uncertainty on the number of W+jets and QCD events obtained from the Matrix Method is obtained by varying ϵ_{QCD} by one standard deviation. The relatively small uncertainty of below 1% on ϵ_{sig} was neglected.

In Table 6.19, the relative change of the total number of predicted events in the standard model background is listed for all shape changing systematics. The numbers listed are for e+jets and μ+jets channels combined and reflect the influence of the systematic uncertainties on the estimated number of background events. The impact on the normalization and in case of JES, JetID, JER, and top quark mass also the differences in preselection efficiencies are taken into account.

The $M_{t\bar{t}}$ distributions of the nominal, $+1\sigma$, and -1σ jet energy scale systematic are shown as a Monte Carlo study in Figure 6.13 for the dominant $t\bar{t}$ background. Figure 6.14 shows the shapes of the distributions for $m_{top} = 175$ GeV, $m_{top} = 170$ GeV and $m_{top} = 180$ GeV for the top mass systematic. In Figure 6.15, the difference in shape is shown for $t\bar{t}$ with and without $t\bar{t}$ + j contribution. The invariant mass distributions of the total standard model background for the top mass systematic can be seen in Figure 6.16 and in Figure 6.17 the invariant mass is shown for the jet energy scale systematic. For all the shown distributions the "Plain" method was used since the shapes from both methods agree.

source	rel. sys. uncertainty (%)			
	"Plain"		"SVT"	
	σ^+	σ^-	σ^+	σ^-
Jet energy scale	+3.02	−3.34	+2.81	−3.49
Jet reconstruction and identification	+5.61	−6.70	+5.54	−6.61
Jet energy resolution	−0.39	−0.85	−0.51	−1.03
b-tag efficiency in MC	+0.24	−0.24	+0.17	−0.20
c-tag efficiency in MC	+0.18	−0.18	+0.14	−0.18
Semileptonic b-tag efficiency in MC	−1.01	+1.07	−0.87	+1.02
Semileptonic b-tagging efficiency in data	+2.15	−2.18	+2.04	−2.22
Negative tag rate parameterization	+0.13	−0.13	+0.08	−0.18
Factorization scale on W boson fractions	−0.14	+0.43	−0.15	+0.47
Heavy quark mass on W boson fractions	+0.99	−1.04	+1.07	−1.12
W boson fractions matching + higher order effects	+2.64	−2.70	+2.83	−2.90
ϵ_{QCD}	+0.77	−0.68	+0.47	−0.42
m_{top} in GeV	170	180	170	180
Top quark mass	+8.82	−7.58	+8.55	−7.80

Table 6.19: Summary of the relative systematic change on the overall normalization of the standard model background for the e+jets and μ+jets channel combined.

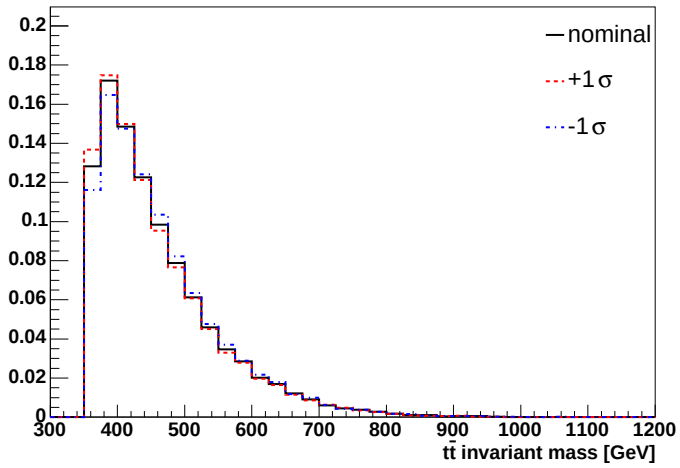

Figure 6.13: Shape comparison of the $M_{t\bar{t}}$ distributions of the nominal, $+1\sigma$, and -1σ jet energy scale systematic.

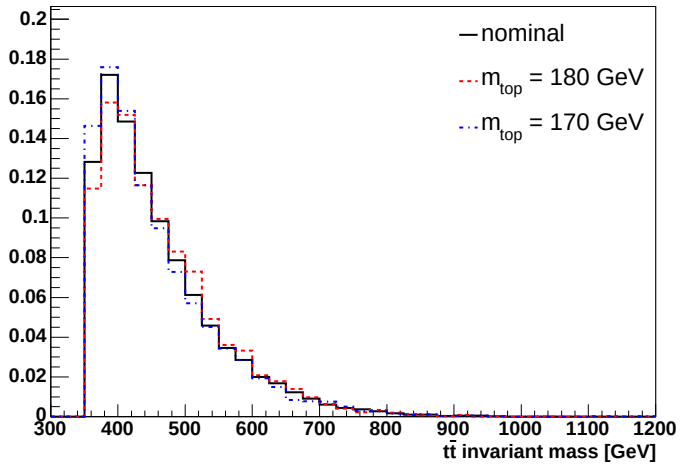

Figure 6.14: Shape comparison of the $M_{t\bar{t}}$ distributions of $m_{top} = 170$ GeV, the nominal $m_{top} = 175$ GeV, and $m_{top} = 180$ GeV top mass systematic.

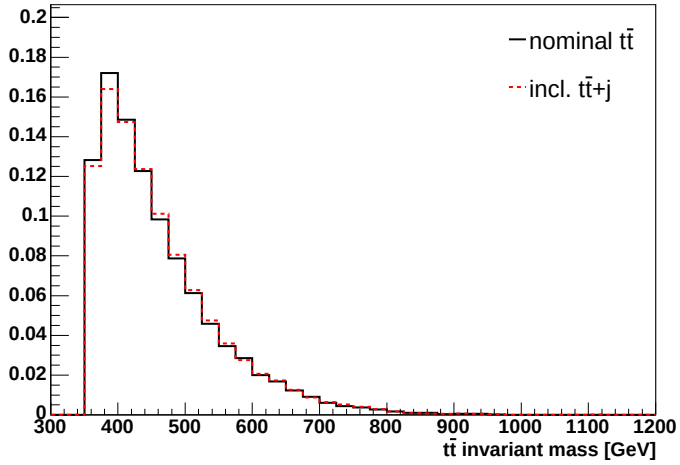

Figure 6.15: Shape comparison of the $M_{t\bar{t}}$ distributions of the pure $t\bar{t}$ sample and a $t\bar{t}$ sample mixed with $t\bar{t}$ + j.

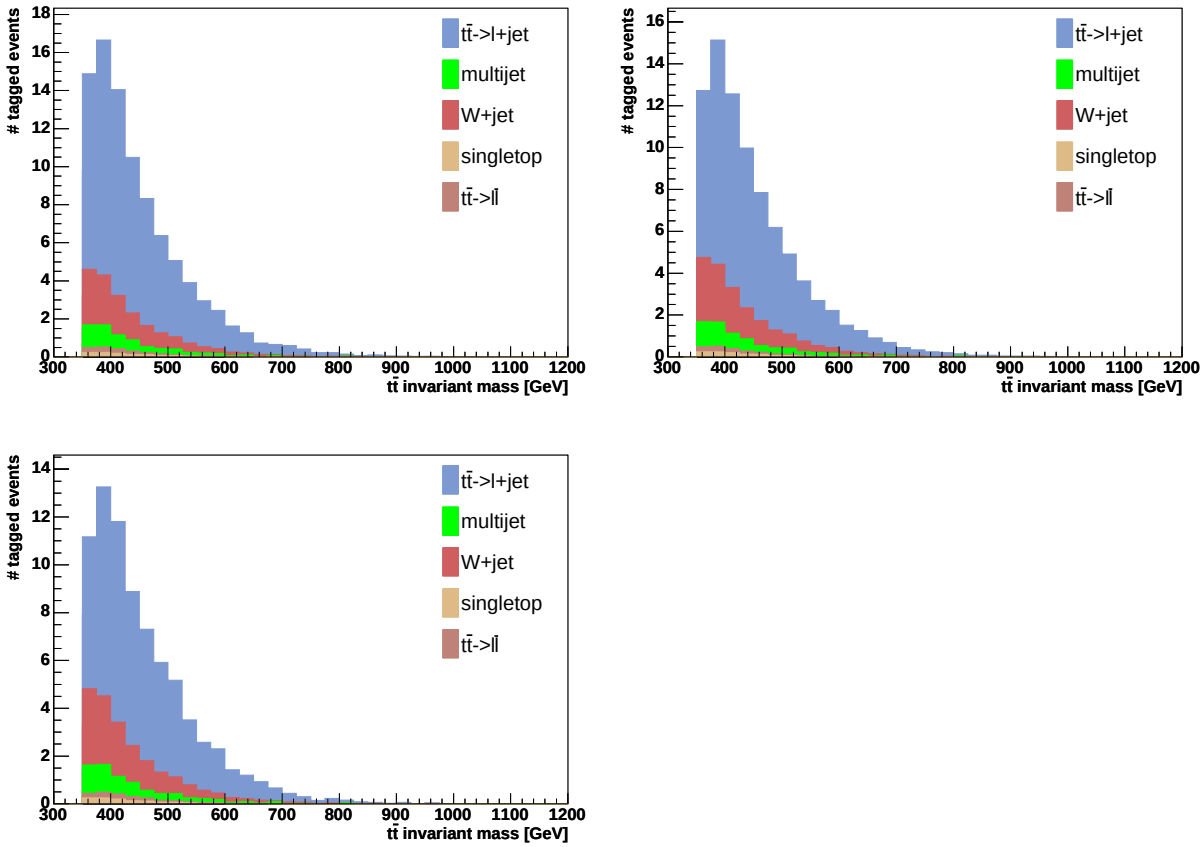

Figure 6.16: Invariant mass distribution for both e+jets and μ+jets channel combined. The upper left plot shows the invariant mass distribution with a top mass of $m_{top} = 170$ GeV, the upper right plot the nominal distribution with $m_{top} = 175$ GeV, and the lower plot shows the invariant mass distribution with $m_{top} = 180$ GeV.

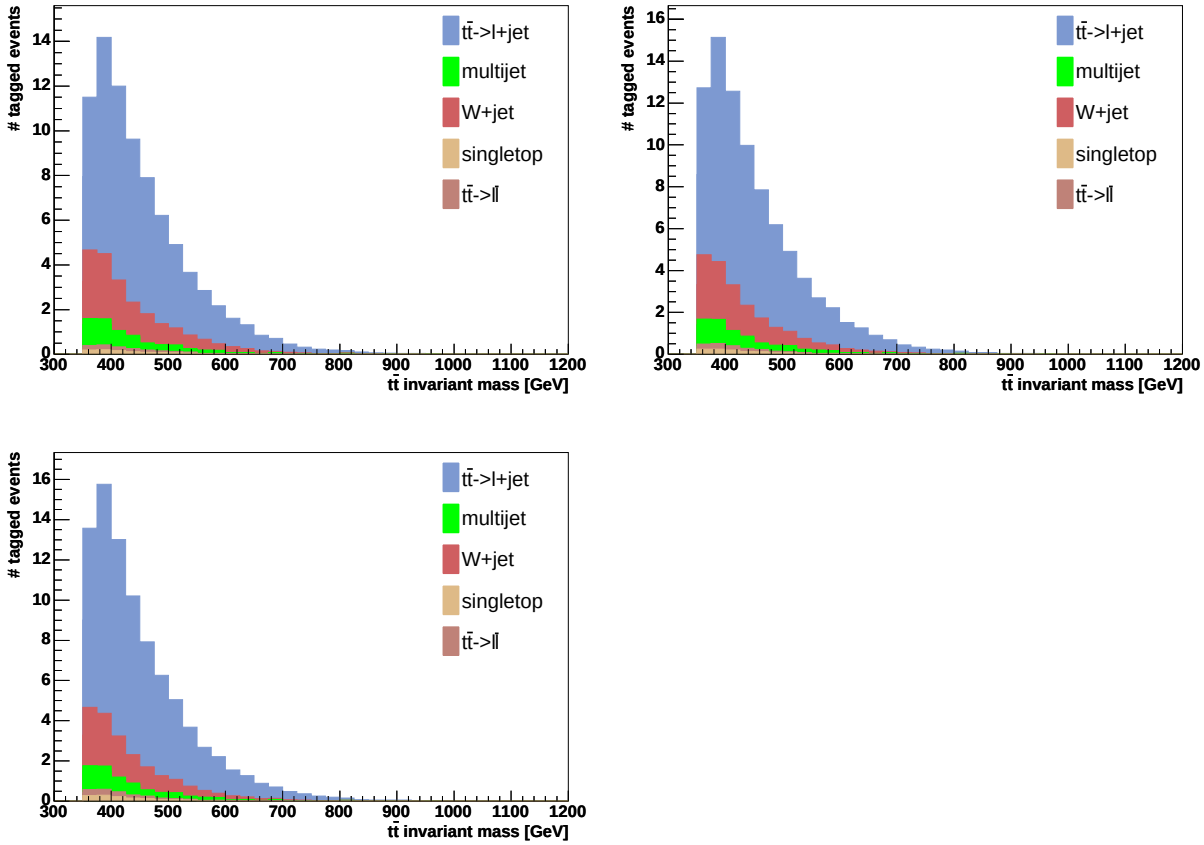

Figure 6.17: Invariant mass distribution for both e+jets and μ+jets channel combined. The upper left plot shows the invariant mass distribution where the jet energy scale was varied by -1σ, the upper right plot shows the nominal distribution, and the lower plot shows the invariant mass distribution with a jet energy scale variation of +1σ.

6.6 Resulting $t\bar{t}$ Invariant Mass Distribution

After all selection cuts 56 events remain in the e+jets channel and 51 events in the μ+jets channel using the "Plain" method and 52 events remain in the e+jets channel and 49 events in the μ+jets channel when using the "SVT" method. Their combined $t\bar{t}$ invariant mass distribution is shown in Figures 6.18 and 6.19 for the two different methods to choose the best permutation. The error bars in the plots on top of histograms show the total systematic uncertainties of each bin which are bin to bin correlated.

The $t\bar{t}$ invariant mass distribution observed in data for the "Plain" method is in general agreement with the Standard Model expectation. Some excesses at the threshold and in the mass region around 450 GeV to 550 GeV can be seen. However, they do not show a significant deviation. The probability that the SM background fluctuates and gives the number of observed data events in the sixth bin ranging from 425 to 450 GeV is only 1.7% and 3.3% for the ninth bin in the range of $500 - 525$ GeV. When taking into account all bins and performing a goodness of fit to the hypothesis that data and the Standard Model prediction agree, the probability for this hypothesis to be true is 92.9%. So no evidence for a $t\bar{t}$ resonance can be seen.

The distribution of the data when using the "SVT" method is also in good agreement with the Standard Model expectation. Only small excesses at the threshold and at 500 GeV can be seen. The probability for the fluctuation in the eighth bin between 475 and 500 GeV is 4.1%. The probability for the whole background distribution to agree with the observed data distribution is 99.9%. When comparing the two distributions obtained with the different methods to choose the correct solution, it can be seen that the agreement between data and Monte Carlo is better when using "SVT" information. In this case the shape observed in data is smoother and without big fluctuations. Common to both distributions is the disagreement between data and Standard Model prediction in the first bin at the threshold of 350 GeV. Also both distributions show an excess in the same mass region of 500 GeV.

6.7 Outlook on an Alternative Solution Finding Method

In Sect. 6.3 two methods were presented to choose the correct solution from `HitFit`, where one was using information obtained from the SVT b-tagging algorithm. Another way of taking advantage of b-tagging is to use the informations obtained with the Neural Network b tagger, described in Sect. 4.6.2.

In this case the χ^2 probability is multiplied with the NN b-tagging probabilities of all jets taking into account the assignment of being a b-jet in this permutation or not.

$$P = P(\chi^2) \cdot \prod^{\text{b-jet}} P_{b,NN}(jet) \cdot \prod^{\text{light-jet}} (1 - P_{b,NN}(jet)) \tag{6.8}$$

In this method data and Monte Carlo can be treated the same since they both have b-tag weights per jets, which are different from 0 and 1. Therefore, the process of rolling the dice to make data and Monte Carlo equal as in the "SVT" method can be avoided.

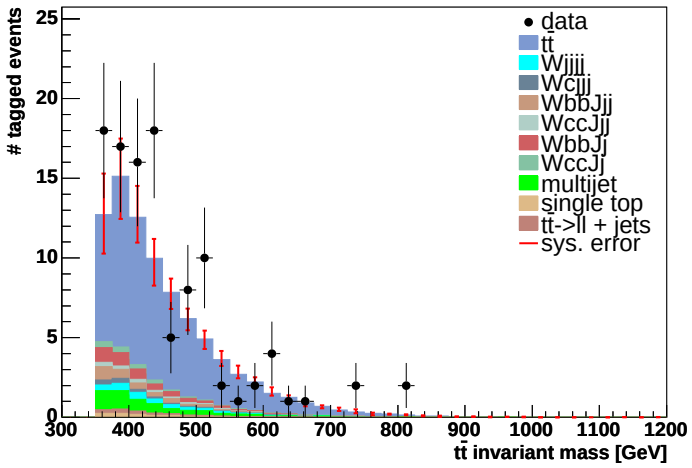

Figure 6.18: The resulting $t\bar{t}$ invariant mass distribution with the "Plain" method for e+jets and μ+jets channel combined.

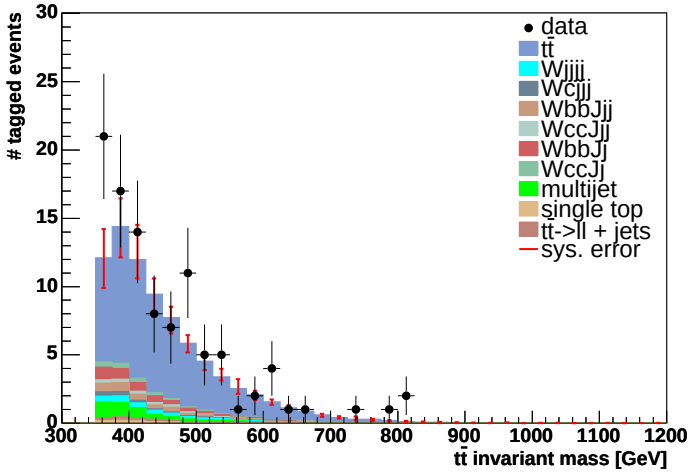

Figure 6.19: The resulting $t\bar{t}$ invariant mass distribution with the "SVT" method for e+jets and μ+jets channel combined.

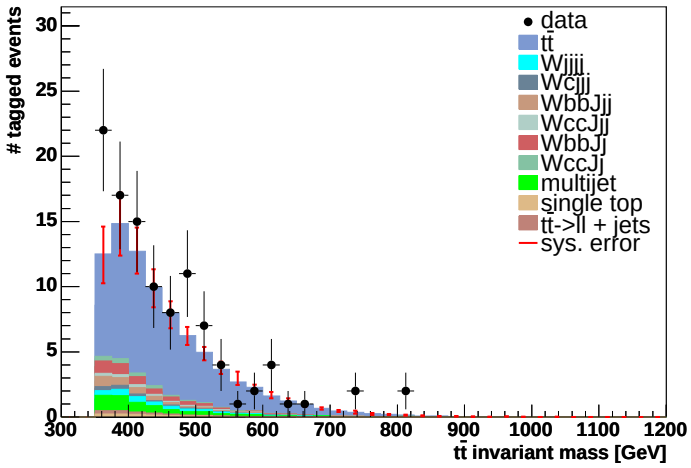

Figure 6.20: The resulting $t\bar{t}$ invariant mass distribution using NN b-tagging information for e+jets and μ+jets channel combined.

In Sect. 4.6.2 it was already mentioned that treating the Monte Carlo samples the same way as data leads to higher b-tag efficiencies for Monte Carlo. Therefore, this method of selecting the correct permutation is only a cross-check and an outlook for the ideal case of having a b-tagging method which treats data and Monte Carlo in the same way.

The expected number of events for this method is the same as for the "Plain" method since all 12 permutations are taken into account. The resulting $t\bar{t}$ invariant mass distribution obtained using the NN b-tagging information is shown in Fig. 6.20. This distribution is comparable in shape with the one obtained with the "SVT" method in Fig. 6.19 since both show the same characteristics as the small excess at 500 GeV and the smooth distribution otherwise.

In the future it is desirable to make the NN b-tagging algorithm work for Monte Carlo such that the b-tag efficiencies are not too high compared to data and that then the NN can directly be applied to Monte Carlo without having to use b-tag parameterizations. To achieve this, a better Monte Carlo simulation would be needed which includes all and the right description off the detector materials and simulates the detector response better so that less and smaller MC-to-data correction factors would be needed to describe the data with Monte Carlo. A first step in this direction has already been achieved by improving the description of the detector materials. Unfortunately, this was not yet available for this analysis and can only be used in the future.

7 Search for $t\bar{t}$ Resonances

No significant excess can be seen in the measured $t\bar{t}$ invariant mass distribution. Therefore, limits on $\sigma_X \times B(X \to t\bar{t})$ for a $t\bar{t}$ resonance X can be set. Here, a Bayesian approach is used as described below to calculate upper limits $\sigma_X \times B(X \to t\bar{t})$ at 95% C.L. for the several different resonance masses. This limit calculation was already available in the top physics group where it is used as a standard method to quote limits in searches for new signals. The obtained limits are then interpreted in a benchmark model of topcolor assisted technicolor.

7.1 Limit Calculation

A binned likelihood fit of the signal and background expectations compared to data is performed on the $t\bar{t}$ invariant mass distribution, as described in Ref. [18, 92]. The backgrounds, including standard model $t\bar{t}$ production, are normalized to the predictions, as described in Sect. 6.2.

The probability to observe Y events, when y events are predicted is given by the Poisson probability distribution:

$$P(Y|y) = \frac{\exp^{-y} y^Y}{Y!} \tag{7.1}$$

where y is the sum of the signal acceptance, $a = \mathcal{L}\epsilon$, times the signal cross section, σ, and N background sources b_s:

$$y = a\sigma + \sum_{s=1}^{N} b_s \tag{7.2}$$

Given M bins the probability to obtain an observed distribution D is

$$P(D|\sigma, \mathbf{a}, \mathbf{b}) = \prod_{m=1}^{M} P(D_m|y_m), \tag{7.3}$$

where $\mathbf{a}$ is the signal acceptance over all bins and $\mathbf{b}$ is the number of events of all bins and background sources. The posterior probability

$$P(\sigma|D) \propto \int_{\mathbf{a}} \int_{\mathbf{b}} P(D|\sigma, \mathbf{a}, \mathbf{b}) \pi(\sigma, \mathbf{a}, \mathbf{b}) \, \mathrm{d}\sigma \, \mathrm{d}\mathbf{a} \, \mathrm{d}\mathbf{b} \tag{7.4}$$

gives an estimate of the cross section, where $\pi(\sigma, \mathbf{a}, \mathbf{b})$ is the prior and encodes the pre-data knowledge of the parameters σ, $\mathbf{a}$, and $\mathbf{b}$. Assuming no correlations between the

parameters the prior density can be factorized as $\pi(\sigma, \mathbf{a}, \mathbf{b}) = \pi(\mathbf{a}, \mathbf{b})\pi(\sigma)$ and Bayes' Theorem can be written as:

$$P(\sigma|D) = \frac{L(D|\sigma)\pi(\sigma)\mathrm{d}\sigma}{\int L(D|\sigma)\pi(\sigma)\mathrm{d}\sigma} \tag{7.5}$$

where

$$L(D|\sigma) = \int \mathrm{d}\mathbf{a} \int \mathrm{d}\mathbf{b} P(D|\sigma, \mathbf{a}, \mathbf{b})\pi(\mathbf{a}, \mathbf{b}) \tag{7.6}$$

is the likelihood. A Bayesian upper limit σ_{95} at a confidence level (C.L.) of 95% is the solution of

$$\int_0^{\sigma_{95}} \mathrm{d}\sigma \, P(\sigma|D) = 0.95. \tag{7.7}$$

The prior density for the signal cross section is assumed to be flat, $\pi(\sigma) = 1/\sigma_{max}$ where σ_{max} is any sufficiently high upper bound on the signal cross section. The prior for the combined signal acceptance and background numbers, $\pi(\mathbf{a}, \mathbf{b})$, is a multivariate Gaussian where uncertainties due to normalization effects and changes in shape are taken into account. To calculate the limits in this analysis the e+jets and the μ+jets channel were combined. Since these two channels are independent, the single channel probability can be replaced by the product $\prod P(D|\sigma, \mathbf{a}, \mathbf{b})$ of the channel probabilities.

7.2 Signal Acceptance Correction

No $t\bar{t}$ resonance contributions were assumed when estimating the W+jets background as described in Sect. 6.2.2. But when calculating the limits, the presence of the resonance has to be taken into account, since in this case the number of estimated W+jets events would be reduced. This is due to the fact that in addition to the top background also the number of expected resonance events have to be subtracted from $N_{W+top}^{untagged}$ obtained from the Matrix Method. To correctly treat the W+jets background in the presence of a resonance the following considerations were made:

- The untagged data sample consists of $N_{W+top+X}^{untagged}$ and $N_{QCD}^{untagged}$.

$$N_{data}^{untag} = N_{W+top+X}^{untag} + N_{QCD}^{untag} \tag{7.8}$$

- $N_{W+top+X}^{untag}$ is the sum of the W+jets, top and resonance contributions, where the W+jets contribution is calculated by:

$$N_{W+jets}^{untag} = N_{W+top+X}^{untag} - N_{top}^{untag} - N_{X}^{untag} \tag{7.9}$$

- This leads to:

$$N_{data}^{untag} = (N_{W+top+X}^{untag} - N_{top}^{untag} - N_{X}^{untag}) + N_{top}^{untag} + N_{X}^{untag} + N_{QCD}^{untag} \tag{7.10}$$

- After applying the b-tagging, the number of untagged events for each sample is multiplied with the b-tag efficiency in that particular sample, which is then the number of events in the tagged sample.

$$N_{data}^{tag} = \epsilon_b^W (N_{W+top+X}^{untag} - N_{top}^{untag} - N_X^{untag}) + \epsilon_b^{top} N_{top}^{untag} + \epsilon_b^X N_X^{untag} + \epsilon_b^{QCD} N_{QCD}^{untag} \tag{7.11}$$

- Solving this equation for the number of resonance events N_X gives:

$$(\epsilon_b^X - \epsilon_b^W) N_X^{untag} = N_{data}^{tag} - \epsilon_b^{top} N_{top}^{untag} - \epsilon_b^W (N_{W+top+X}^{untag} - N_{top}^{untag}) - \epsilon_b^{QCD} N_{QCD}^{untag} \tag{7.12}$$

Thus, instead of correcting the number of W+jets events for the limit calculation, the resonance input can be corrected for the b-tag efficiency in a W+jets sample. This was done for all resonance samples and also for all systematics which potentially change the b-tag efficiency.

7.3 Limits on $\sigma_X \times B(X \to t\bar{t})$

The expected limits on $\sigma_X \times B(X \to t\bar{t})$ at the 95% confidence level for the e+jets and μ+jets channel combined calculated with and without systematic uncertainties taken into account are obtained for the different resonance masses and are listed in Table 7.1 for both, the "Plain" and the "SVT" method.

It can be seen that the expected limits increase when systematic uncertainties are taken into account. When comparing the "Plain" with the "SVT" method it is noticeable

	expected limits [pb]			
	statistical only		including systematics	
M_X [GeV]	"Plain"	"SVT"	"Plain"	"SVT"
350	2.27	2.34	3.59	3.44
400	2.14	2.21	3.26	3.31
450	1.88	1.95	3.09	3.22
500	1.59	1.65	1.95	2.11
550	1.38	1.46	1.55	1.67
600	1.18	1.26	1.25	1.38
650	1.08	1.16	1.14	1.27
750	0.99	1.09	1.00	1.16
850	1.01	1.15	1.02	1.19
1000	1.21	1.46	1.16	1.40

Table 7.1: Expected limits for $\sigma_X \times B(X \to t\bar{t})$ at the 95% confidence level with and without systematic uncertainties taken into account, shown for both, the "Plain" and the "SVT" method.

	"Plain"			
	statistical only		including systematics	
M_X [GeV]	exp. limit [pb]	obs. limit [pb]	exp. limit [pb]	obs. limit [pb]
350	2.27	4.55	3.59	5.82
400	2.14	4.24	3.26	5.95
450	1.88	3.66	3.09	4.82
500	1.59	2.99	1.95	2.93
550	1.38	2.01	1.55	1.57
600	1.18	1.76	1.25	1.35
650	1.08	1.57	1.14	1.19
750	0.99	1.62	1.00	1.33
850	1.01	1.81	1.02	1.35
1000	1.21	2.03	1.16	1.46

Table 7.2: Expected and observed limits for $\sigma_X \times B(X \to t\bar{t})$ at the 95% confidence level obtained for the "Plain" method with and without systematic uncertainties taken into account.

that the expected limits are increased by ≈ 1 pb for the "SVT" method for resonance masses up to 500 GeV. For the higher resonance masses the difference between the expected limits obtained with the two methods is much smaller although the limits are still higher when using the "SVT" method.

In Sect. 6.3.3 it was shown that both methods have about the same mass resolution. Based on this fact, the higher statistical limits obtained with the "SVT" method can be explained by the lower statistics due to this method. For the expected limits including systematics, the higher results with the "SVT" method are not only due to lower statistics, but also due to additional systematic effects since the uncertainty of the b-tagging enters twice.

The observed 95% C.L. limits on $\sigma_X \times B(X \to t\bar{t})$ with and without systematic uncertainties taken into account can be found in Table 7.2 for the "Plain" and in Table 7.3 for the "SVT" method. For comparison the expected limits are also included in the tables. In Figure 7.1 and Figure 7.2, the expected and observed limits with systematic uncertainties taken into account are shown for the different resonance masses for the "Plain" and "SVT" method, respectively.

The observation that the observed limits are almost always higher than the expected limits can be explained by the fact that there are more events found in data than predicted by the Standard Model. Although there is no deviation in shape when comparing the data and the Monte Carlo prediction, the excess in the number of observed events causes the observed limits to increase. Another observation is the increased expected and observed limits for the 850 GeV and 1000 GeV resonances compared to the decreasing limits for the lower mass resonances. This behavior is a consequence of the bad resolution in the $M_{t\bar{t}}$ distribution for the high resonance masses. When comparing the observed limits including systematics for the two methods, it can be seen that for the

	"SVT"			
	statistical only		including systematics	
M_X [GeV]	exp. limit [pb]	obs. limit [pb]	exp. limit [pb]	obs. limit [pb]
350	2.34	5.12	3.44	6.13
400	2.21	3.81	3.31	4.62
450	1.95	3.06	3.22	3.00
500	1.65	2.91	2.11	2.77
550	1.46	2.35	1.67	1.67
600	1.26	2.05	1.38	1.58
650	1.16	1.75	1.27	1.40
750	1.09	1.93	1.16	1.73
850	1.15	2.16	1.19	1.93
1000	1.46	2.67	1.40	2.02

Table 7.3: Expected and observed limits for $\sigma_X \times B(X \to t\bar{t})$ at the 95% confidence level obtained for the "SVT" method with and without systematic uncertainties taken into account.

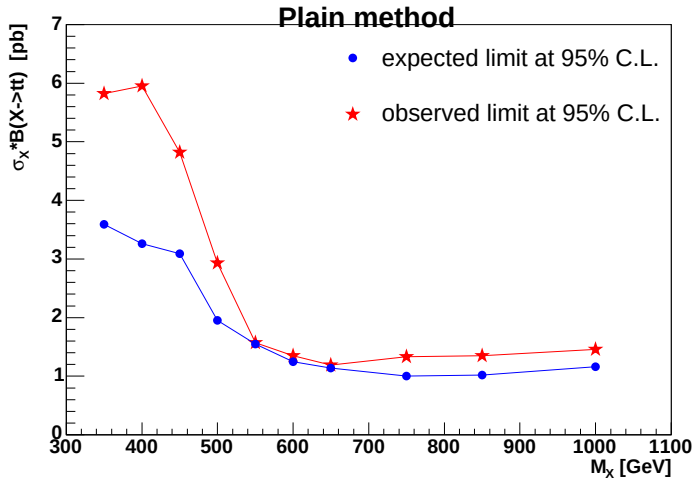

Figure 7.1: The expected and observed 95% C.L. upper limits on $\sigma_X \times B(X \to t\bar{t})$ with systematic uncertainties included as a function of the resonance mass M_X obtained for the "Plain" method.

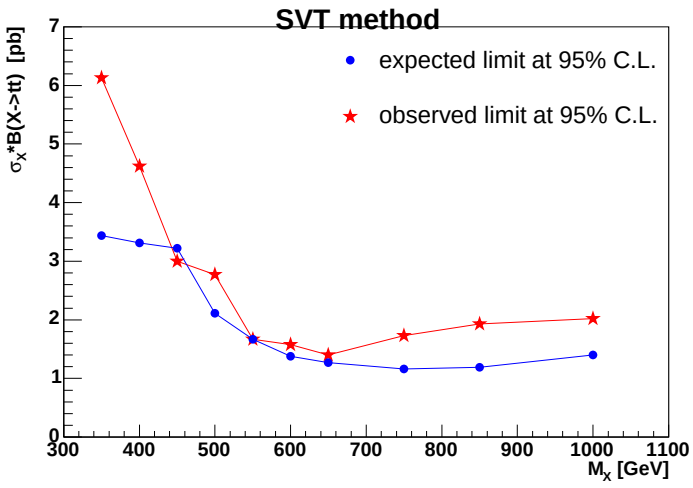

Figure 7.2: The expected and observed 95% C.L. upper limits on $\sigma_X \times B(X \to t\bar{t})$ with systematic uncertainties included as a function of the resonance mass M_X obtained for the "SVT" method.

masses of $400 - 500$ GeV the observed limits are lower for the "SVT" method, although the "SVT" method led to higher expected limits including systematics compared to the "Plain" method.

For the low resonance masses up to 500 GeV the observed limits including systematics for both methods are significantly higher than the expected ones, since in Fig. 6.18 and 6.19 a slight excess in this mass region could be seen, although no deviation in shape has been observed. The only exception is the limit for 450 GeV for the "SVT" method where the observed limit including systematics is lower than the expected limit which can be understood by the fact that the $t\bar{t}$ invariant mass distribution for the "SVT" method shows a deficit of events in the two bins around 450 GeV. The observed limits including systematics for the masses of $550 - 650$ GeV are close to the expected ones for both methods, whereas the differences between expected and observed limits increase for the higher masses. For the "Plain" method the increase is not as high as for the "SVT" method where the fraction of observed data events in the $M_{t\bar{t}}$ distribution in the mass region above 700 GeV is higher, as could be seen in Fig. 6.18 and 6.19.

In general the observed limits obtained with the "Plain" method are lower, but for a few resonance masses the "SVT" method results in better limits. Although the "SVT" method was expected to improve the analysis compared to the "Plain" method, this could not be confirmed in the obtained limits. The reason for this is the mass resolution which against the expectation did not improve by adding b-tag information. This needs to be investigated further.

In Figures 7.3 and 7.4 the posterior probability densities obtained with the "Plain" and the "SVT" method are shown as a function of $\sigma_X \times B(X \to t\bar{t})$ for the expected and observed limits at 95% C.L. including systematic uncertainties. Here, only the distribu-

tions for exemplary resonance masses of 400 GeV, 500 GeV, 650 GeV, and 1000 GeV are presented. The distributions for the other resonance masses can be found in the Appendix A.2. For illustration purposes, each $t\bar{t}$ invariant mass distribution is shown with an assumed resonance contribution where the value of the cross section is chosen to be the maximum posterior probability density for the observed limit including systematics. If this value is too small such that the resonance contribution is not visible, an additional contribution is plotted which is scaled up by a factor of 5 to 15.

7.4 Interpretation in topcolor assisted Technicolor

In Figure 7.5, the observed limits at 95% C.L. of the resonance masses above 350 GeV for both methods, the "Plain" and the "SVT", are shown together with the predicted cross section of a leptophobic Z' boson as given in Tab. 2.2 for a width of $\Gamma_{Z'} = 0.012 M_{Z'}$. The combination of the theoretical predictions with the experimental limits allows the exclusion of such a leptophobic Z' boson with

$$M_{Z'} < 660\,\text{GeV at}\,95\%\ \text{C.L. for the "Plain" method and}$$
$$M_{Z'} < 640\,\text{GeV at}\,95\%\ \text{C.L. for the "SVT" method.}$$

7.5 Comparison with other Analyses

In Run I both experiments, DØ and CDF, performed a search for $t\bar{t}$ resonances. The analysis performed by DØ [93] on 130 pb^{-1} of data used the same kinematic fit as presented in this analysis and found no evidence for a $t\bar{t}$ resonance. Therfore, the resulting limits on $\sigma_X \times B(X \to t\bar{t})$ were used to quote a limit on the mass of a topcolor Z' with $\Gamma_{Z'} = 0.012 M_{Z'}$ of 560 GeV. The CDF analysis [94] performed on 106 pb^{-1} of data also used a kinematic fit to reconstruct the $t\bar{t}$ invariant mass and could exclude a leptophobic Z' with $\Gamma_X = 0.012 M_X$ and a mass of 480 GeV.

In RunII preliminary conference results on the search for $t\bar{t}$ resonances have been presented by both experiments. For DØ an earlier version of this analysis resulted in a limit on the mass of a topcolor Z' of 680 GeV [95]. There, the use of b-tagging information in the choice for the correct solution from the kinematic fit and the correct treatment of the W+jets background in the presence of a resonance, as described in Sect. 7.2, were not yet implemented. Through these improvements implemented in the analysis the limits on $\sigma_X \times B(X \to t\bar{t})$ increased slightly and the mass exclusion limit on a leptophobic Z' is now lower compared to the preliminary conference result, although the Run II measurement on ~ 370 pb^{-1} of data still extends the DØ Run I exclusion on $M_{Z'}$ by 100 GeV when comparing with the result of the "Plain" method.

For the measurement of the $t\bar{t}$ invariant mass, CDF used a different approach in Run II [96]. The Standard Model $t\bar{t}$ matrix element information is used to extract the $t\bar{t}$ invariant mass spectrum. With this analysis performed on 680 pb^{-1} of data the leptophobic topcolor Z' mass has been excluded below 725 GeV. A new analysis from DØ on ~ 1 fb^{-1} of data will follow in the summer of 2006.

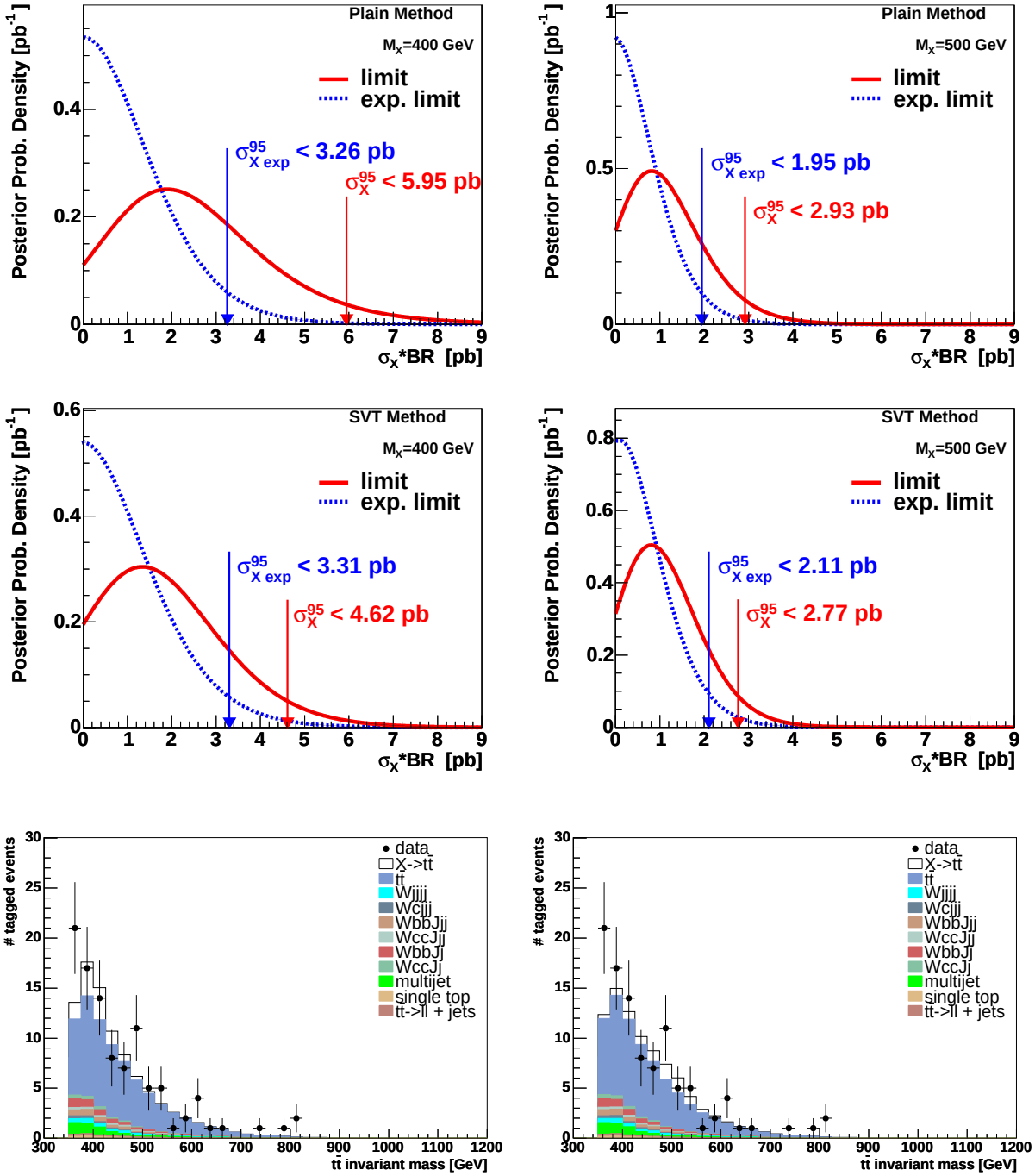

Figure 7.3: Posterior probability densities are shown as a function of $\sigma_X \times B(X \to t\bar{t})$ for the "Plain" method (top) and the "SVT" method (middle). In the left column the distributions are shown for a resonance mass of 400 GeV, and in the right column for 500 GeV. In the bottom plots the $M_{t\bar{t}}$ distribution is shown with an assumed resonance contribution of 1.3 pb and 0.8 pb for masses of 400 GeV and 500 GeV, respectively.

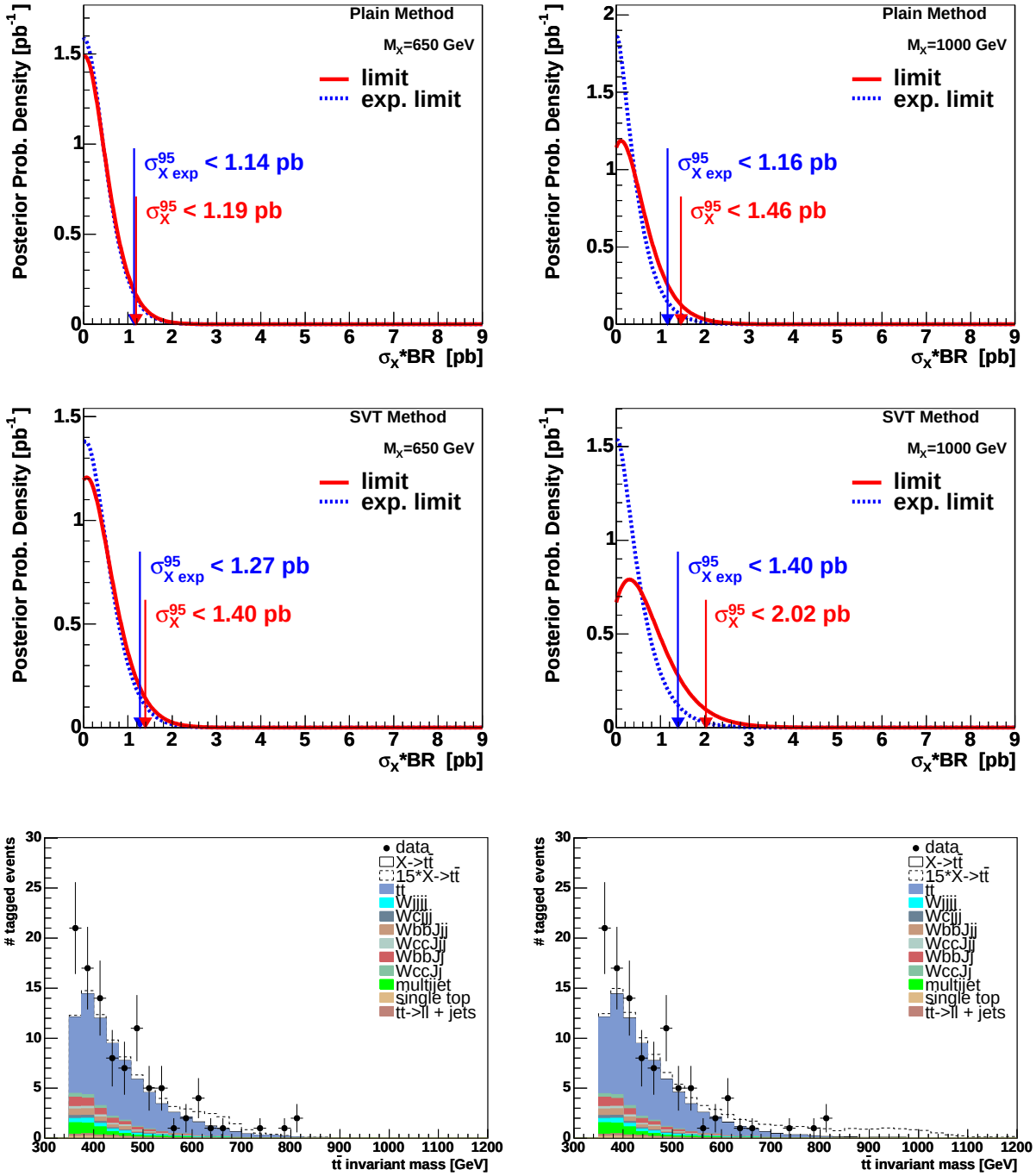

Figure 7.4: Posterior probability densities are shown as a function of $\sigma_X \times B(X \to t\bar{t})$ for the "Plain" method (top) and the "SVT" method (middle). In the left column the distributions are shown for a resonance mass of 650 GeV, and in the right column for 1000 GeV. In the bottom plots the $M_{t\bar{t}}$ distribution is shown with an assumed resonance contribution of (15×)0.1 pb and (15×)0.3 pb for masses of 650 GeV and 1000 GeV, respectively.

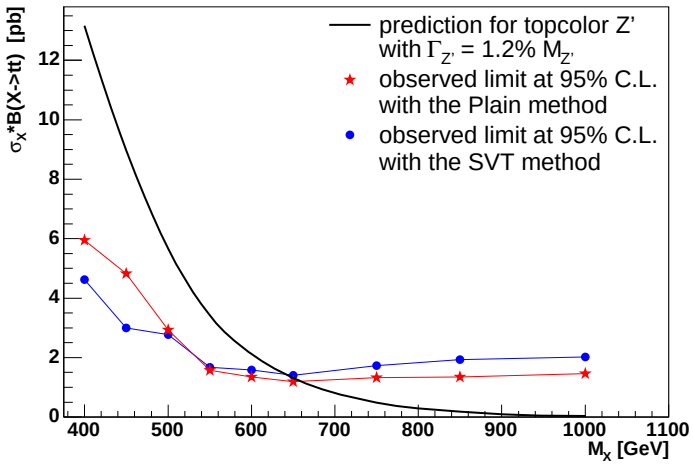

Figure 7.5: The observed 95% confidence level upper limits on $\sigma_X \times B(X \rightarrow t\bar{t})$ as a function of resonance mass $M_{Z'}$ for the "Plain" and the "SVT" method compared with the predicted topcolor assisted technicolor cross section for a leptophobic Z' with a width of $\Gamma_{Z'} = 0.012 M_{Z'}$.

7.6 Outlook

The upper limits on $\sigma_X \times B(X \rightarrow t\bar{t})$ at 95% C.L. which will be expected when performing this analysis on data samples with higher luminosities are shown in comparison with the limits obtained in this analysis for the "SVT" method in Fig. 7.6. The values for the luminosities represent the currently available amount of data of 1 fb^{-1} which will be analyzed shortly, the base luminosity of 4 fb^{-1} which the Tevatron will hopefully deliver at least until its final run in 2009, and the design luminosity of 8 fb^{-1} which will be the final luminosity in 2009 if everything works as planned.

In addition to higher statistics, further improvements can be achieved by reducing the systematic uncertainties. The uncertainty on the top quark mass will be reduced due to improved top mass measurements which will have only a small uncertainty in the order of a very few GeV. Already, the world average of the top quark mass has an uncertainty of 2.9 GeV which will be further decreased. Another systematic uncertainty which can be reduced by an improved understanding of the detector and more calibration data is due to the jet energy scale. Also all systematic uncertainties which need to be derived from Monte Carlo and data, such as the uncertainties on the MC-to-data correction factors, ϵ_{QCD}, and all the b-tagging parameterizations, will be reduced through higher statistics in data, a better description of the detector in Monte Carlo, and therefore a better data – Monte Carlo agreement.

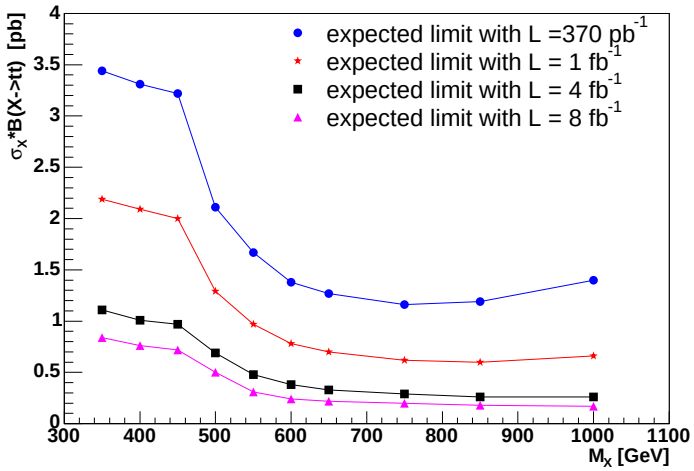

Figure 7.6: The expected 95% C.L. upper limits on $\sigma_X \times B(X \rightarrow t\bar{t})$ as a function of the resonance mass M_X for higher luminosities of 1 fb^{-1}, 4 fb^{-1}, and 8 fb^{-1}, compared with the obtained limits in this analysis on $\approx$ 370 pb^{-1} of data.

8 Summary

The measurement of the $t\bar{t}$ invariant mass distribution and a search for $t\bar{t}$ resonances has been performed in the l+jets final states using data corresponding to an integrated luminosity of about 370 pb^{-1}, collected with the DØ detector during Run II of the Tevatron collider. The event selection made use of the b-jet identification via secondary vertices which enhanced the $t\bar{t}$ fraction in the data sample considerably. The $t\bar{t}$ invariant mass distribution was obtained from a kinematic fit where the mass of the W boson and the top quark were constraint to nominal values. Two methods were used to select the best permutation. The "Plain" method chose the permutation with the highest χ^2 probability, in addition the "SVT" method used b-tagging information to reject wrong permutations. With the "SVT" method developed in the framework of this thesis, the number of correct solutions could be increased by more than 12%. It is a further development of the preliminary conference result [95] which has been achieved in an earlier stage of this thesis.

The $t\bar{t}$ invariant mass distributions obtained by the two methods agree well with the Standard Model prediction and no statistically significant deviation indicating a $t\bar{t}$ resonance could be observed. Therefore, no evidence for new physics can be claimed. Model independent upper limits at 95% C.L. on $\sigma_X \times B(X \rightarrow t\bar{t})$ using a Bayesian method have been obtained for different hypothesized masses of a narrow-width heavy resonance decaying into $t\bar{t}$. Compared to the preliminary conference result the correct treatment of the W+jets background in the presence of a resonance, as described in Sect. 7.2, has been implemented in the limit calculation. The observed limits obtained for the "SVT" method are slightly higher than for the one obtained from the "Plain" method due to decreased statistics and additional systematic uncertainties.

Within a topcolor-assisted technicolor model, the existence of a leptophobic Z' boson with a width of $\Gamma_{Z'} = 0.012 M_{Z'}$ can be excluded at 95% C.L. for masses of

$$\begin{aligned} M_{Z'} &< 660\,\text{GeV for the "Plain" method and} \\ M_{Z'} &< 640\,\text{GeV for the "SVT" method.} \end{aligned}$$

Through the correct treatment of the W+jets background, the limits on $\sigma_X \times B(X \rightarrow t\bar{t})$ increased slightly and the mass exclusion limit on a leptophobic Z' is now lower compared to the preliminary conference result. Nevertheless, these limits obtained for the two methods significantly increase the limits on $M_{Z'}$ previously published by DØ [93] and CDF [94] for Run I data by 100 GeV when comparing with the result of the "Plain" method.

At the end of Run II of the Tevatron the available statistics will be higher by a factor of $10 - 20$ than that in the presented analysis. In addition to higher statistics,

the systematic uncertainties will be reduced due to an improved understanding of the detector and the resulting advanced reconstruction algorithms. Also a better data – Monte Carlo agreement will be achieved by a better description of the detector in Monte Carlo. With all these improvements which will follow in the near future, the invariant mass distribution is expected to be even more sensitive to possible $t\bar{t}$ resonances and either an evidence for a $t\bar{t}$ resonance will be seen or the limits on $\sigma_X \times B(X \to t\bar{t})$ will decrease significantly.

A Additional Information about the Analysis

A.1 Input Parameters for Pythia

In order to generate $X \rightarrow t\bar{t}$ with $M_X = 500$ GeV/c^2 and $\Gamma_X = 0.012\ M_X$ the following parameters were used:

- $MSTP(51) =$: the $CTEQ5L$ parton distribution functions are used
- $MSTP(52) = 2$: use PDFLIB as pdf library
- $PMAS(6,1) = 175$: this sets the top mass to 175 GeV/c^2
- $MSEL = 21$: this selects the process $f_i\bar{f}_i \rightarrow \gamma/Z^0/X$
- $MSTP(44) = 3$: only the X boson is considered in the matrix elements
- $CKIN(1) = 300, CKIN(2) = 2000$: the invariant mass of $t\bar{t}$ varies between $300 - 2000$ GeV/c^2
- $PMAS(32,1) = 500$: this sets the mass of the X boson to 500 GeV/c^2
- $MDME(289,1) = 0$ – $MDME(293,1) = 0$, $MDME(295,1) = 0$ – $MDME(310,1) = 0$, $MDME(294,1) = 1$:
  only $t\bar{t}$ decay mode is allowed for the X boson
- $PARU(121) = -0.423$, $PARU(122) = -0.610$, $PARU(123) = 0.236$, $PARU(124) = 0.610$, $PARU(125) = -0.049$, $PARU(126) = -0.610$, $PARU(127) = 0.610$, $PARU(128) = 0.610$:
  vector and axial couplings of the X boson to first generation quark and leptons
- $PARJ(180) = -0.423$, $PARJ(181) = -0.610$,$PARJ(182) = 0.236$, $PARJ(183) = 0.610$, $PARJ(184) = -0.049$, $PARJ(185) = -0.610$, $PARJ(186) = 0.610$, $PARJ(187) = 0.610$:
  vector and axial couplings of the X boson to second generation quark and leptons
- $PARJ(188) = -0.423$, $PARJ(189) = -0.610$, $PARJ(190) = 0.236$, $PARJ(191) = 0.610$, $PARJ(192) = -0.049$, $PARJ(193) = -0.610$, $PARJ(194) = 0.610$, $PARJ(195) = 0.610$:
  vector and axial couplings of the X boson to third generation quark and leptons

The settings for the vector and axial couplings are needed to set the width of the X boson to the desired value of $\Gamma_X = 0.012 M_X$ since the full interference structure needs to be included. In Pythia, the default setting for the couplings of the X boson to quarks and leptons is the same as that for the Standard Model Z boson.

A.2 Control Plots

As a sanity check, the following control plots are shown:

- Figures A.1 - A.5 show data–MC comparisons after applying all cuts. The variables shown are the p_T of the four leading jets and the lepton, the p_T sum of all jets (Ht), the missing energy $\not\!\!E_T$, the aplanarity, the sphericity, and the centrality. These distributions are shown using the normalization obtained with the "Plain" method. The plots show good agreement between data and Monte Carlo although, when looking at the p_T distributions of the third and fourth leading jets, it can be seen that the Monte Carlo does not describe well the data in the low p_T region. This is influenced by a cut on the minimum quark energy of 8 GeV at generator level for the W+jets Monte Carlo samples. After applying the jet energy scale on the reconstructed jets, the jet energies will be in the region of the minimum p_T requirement for jets of 15 GeV. But since this is only the lowest possible energy a jet in a W+jets sample can have, and most of the generated quarks will have a higher energy leading to a higher jet energy, the low p_T region in the jet p_T spectrum is underpopulated by W+jets events.

- Figures A.6 - A.9 show data–MC comparisons after applying all cuts. The variables shown are the χ^2 coming from `HitFit` for the chosen solution, the $t\bar{t}$ invariant mass if $\chi^2 \leq 10$ and $\chi^2 > 10$, and the p_T of the top quark. These distributions are shown for the "Plain" and the "SVT" method. When comparing these two methods it can be seen that the $t\bar{t}$ invariant mass distributions obtained for events with $\chi^2 \leq 10$ and $\chi^2 > 10$ differ in the amount of events. While for $\chi^2 \leq 10$ the "SVT" method has less events in the distribution, this is the case for the "Plain" method when requiring $\chi^2 > 10$. This is due to the different χ^2 distributions. This distribution is broader and with a larger tail towards higher values for the "SVT" method since not necessarily the lowest $\chi 2$ solution could be matched with a tagged jet.

- In Figures A.10 – A.12 the posterior probability densities obtained with the "Plain" and the "SVT" method are shown as a function of $\sigma_X \times B(X \rightarrow t\bar{t})$ for the expected and observed limits at 95% C.L. including systematic uncertainties. Here the distributions for resonance masses of 350 GeV, 450 GeV, 550 GeV, 600 GeV, 750 GeV, and 850 GeV are presented. For illustration purposes, each $t\bar{t}$ invariant mass distribution is shown with an assumed resonance contribution where the value of the cross section is chosen to be the maximum posterior probability density for the observed limit including systematics. If this value is too small such that the resonance contribution is not visible, an additional contribution is plotted which is scaled up by a factor of 5 to 15.

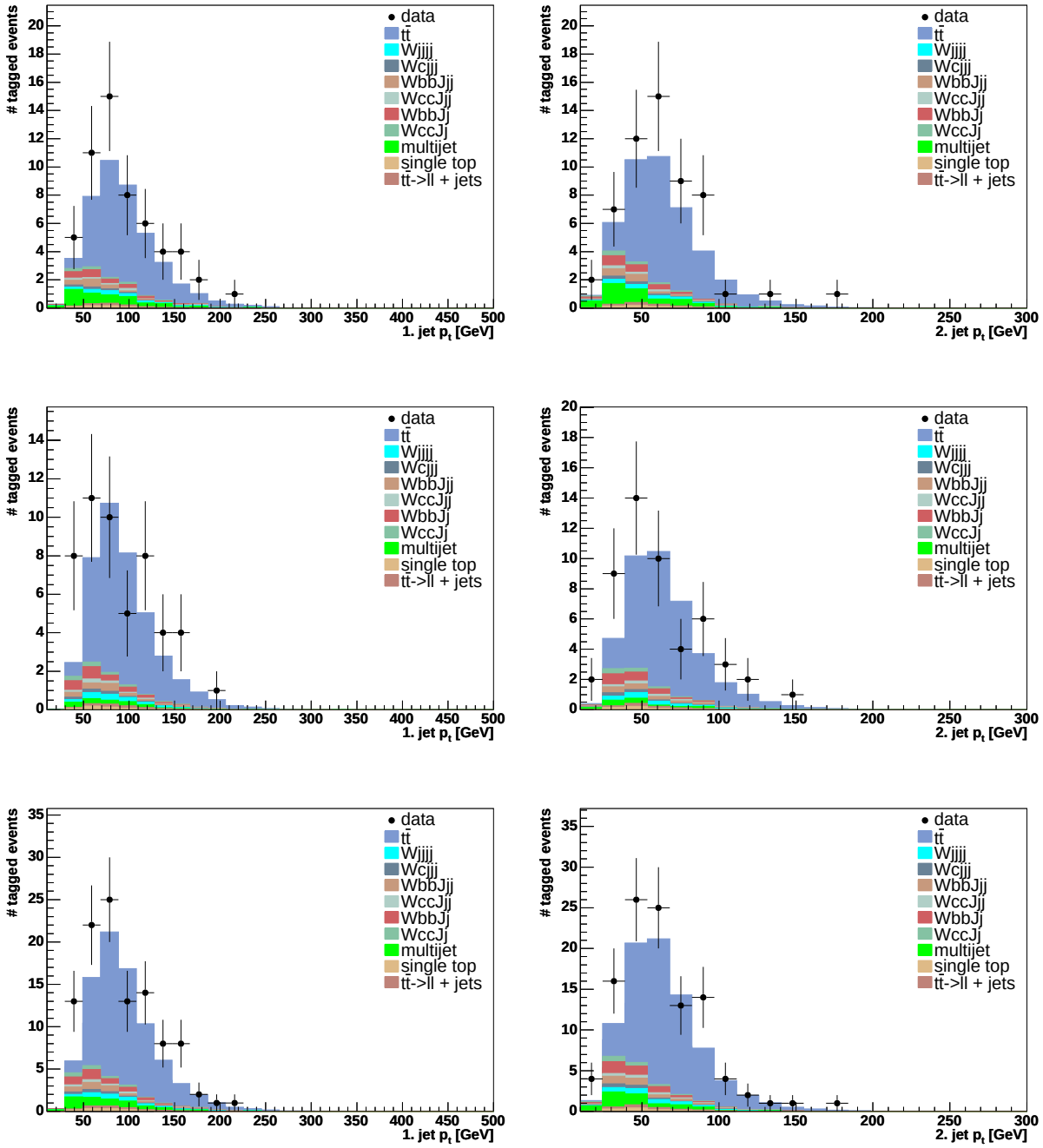

Figure A.1: Comparison between data and Monte Carlo after applying all cuts for the e+jets channel (top), the μ+jets channel (middle), and for both channels combined (bottom). The variables are the p_T of the first leading jet (left), and the p_T of the second leading jet (right).

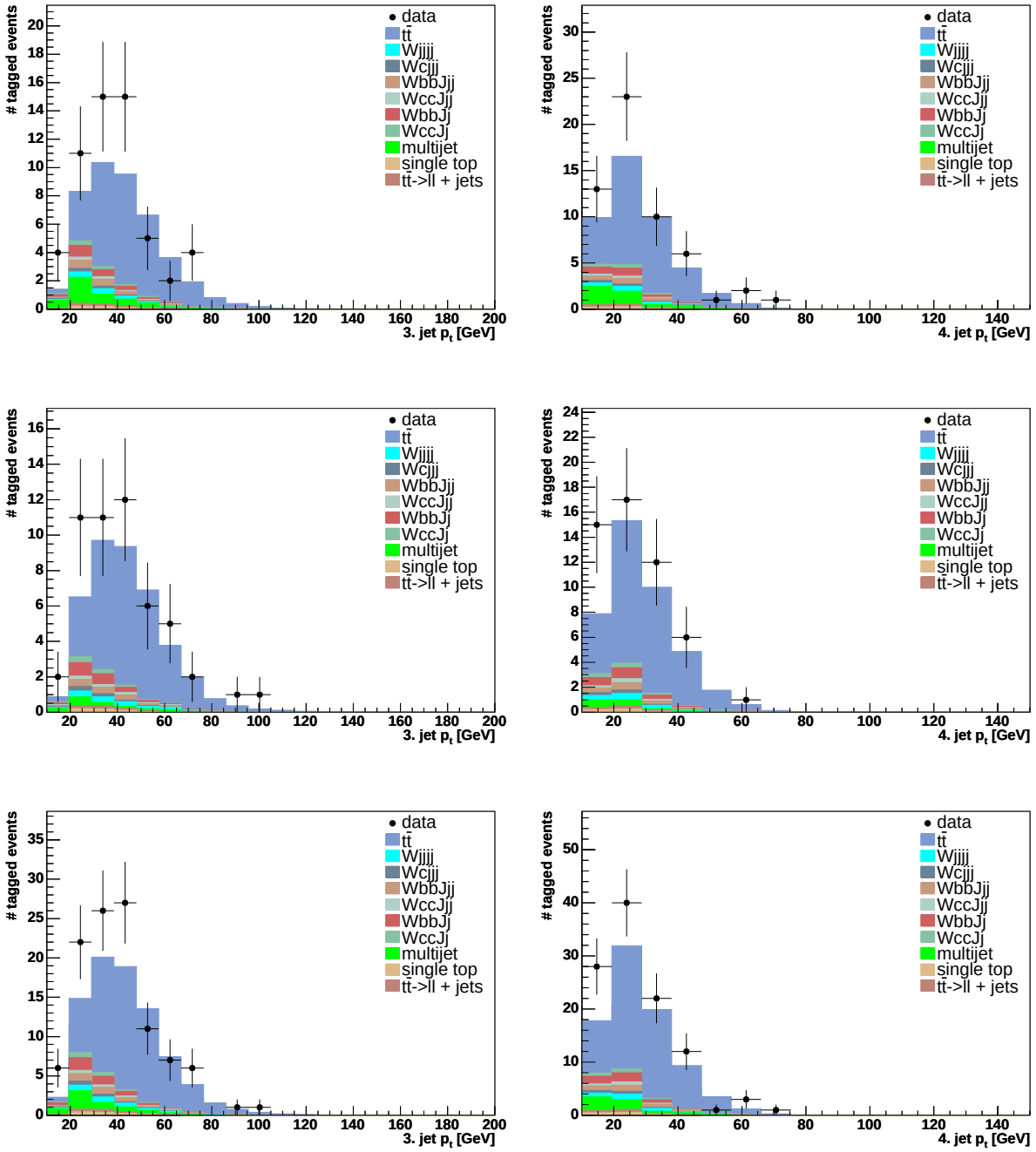

Figure A.2: Comparison between data and Monte Carlo after applying all cuts for the e+jets channel (top), the μ+jets channel (middle), and for both channels combined (bottom). The variables are the p_T of the third leading jet (left), and the p_T of the fourth leading jet (right).

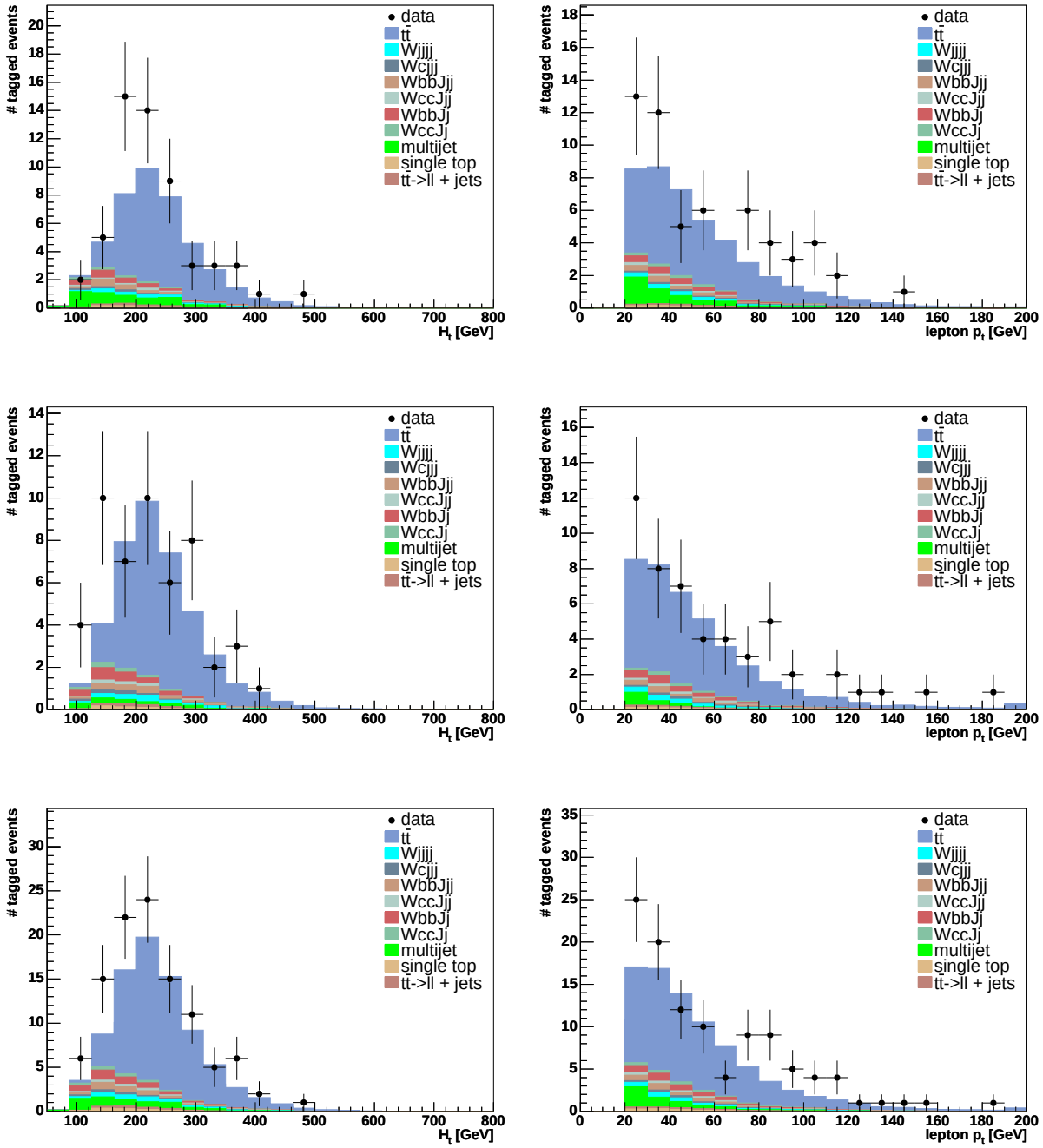

Figure A.3: Comparison between data and Monte Carlo after applying all cuts for the e+jets channel (top), the μ+jets channel (middle), and for both channels combined (bottom). The variables are the p_T sum of all jets (Ht) (left), and the p_T of the lepton (right).

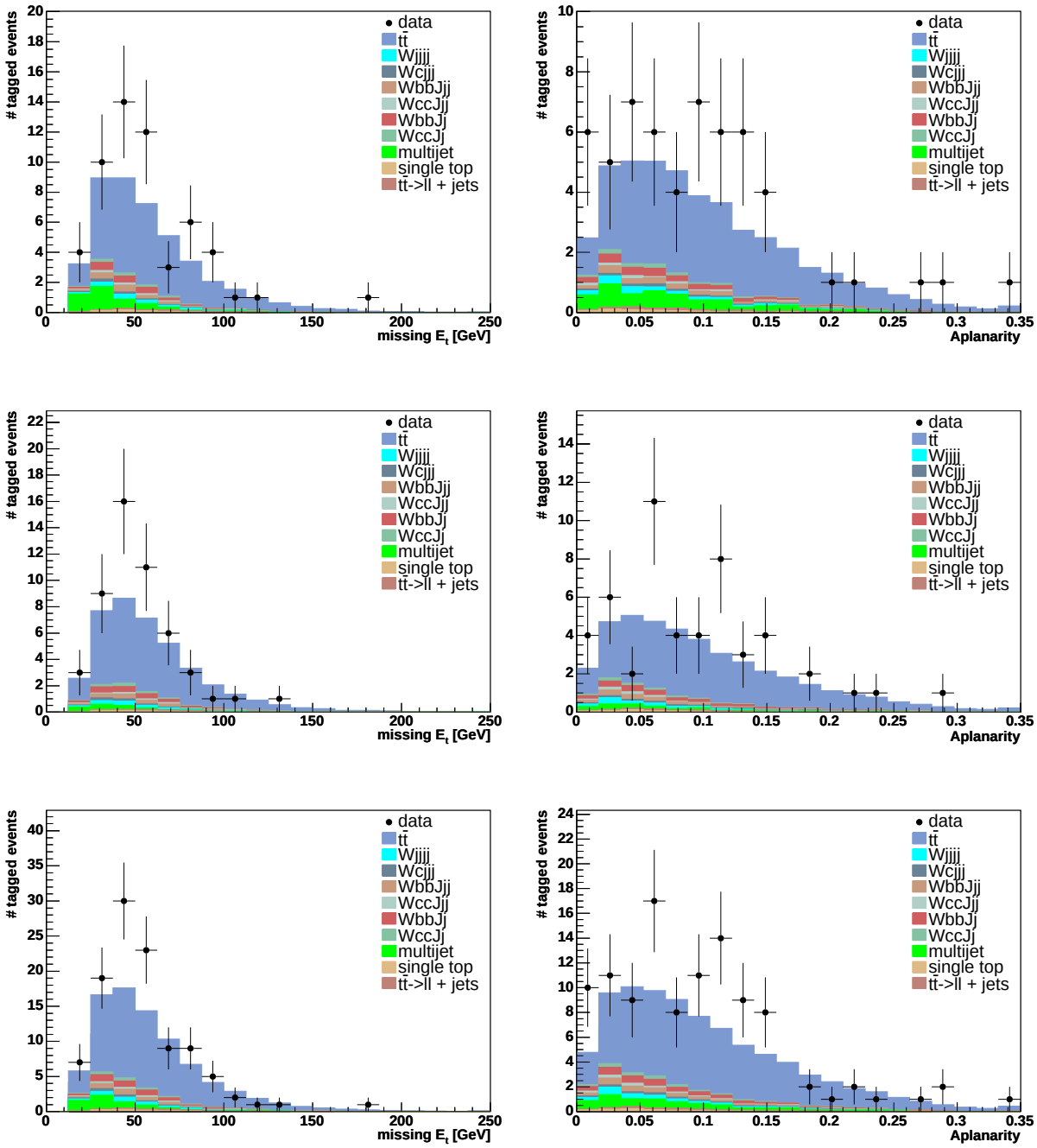

Figure A.4: Comparison between data and Monte Carlo after applying all cuts for the e+jets channel (top), the μ+jets channel (middle), and for both channels combined (bottom). The variables are the missing E_T (left), and the angle between the $\not\!\!E_T$ and the aplanarity (right).

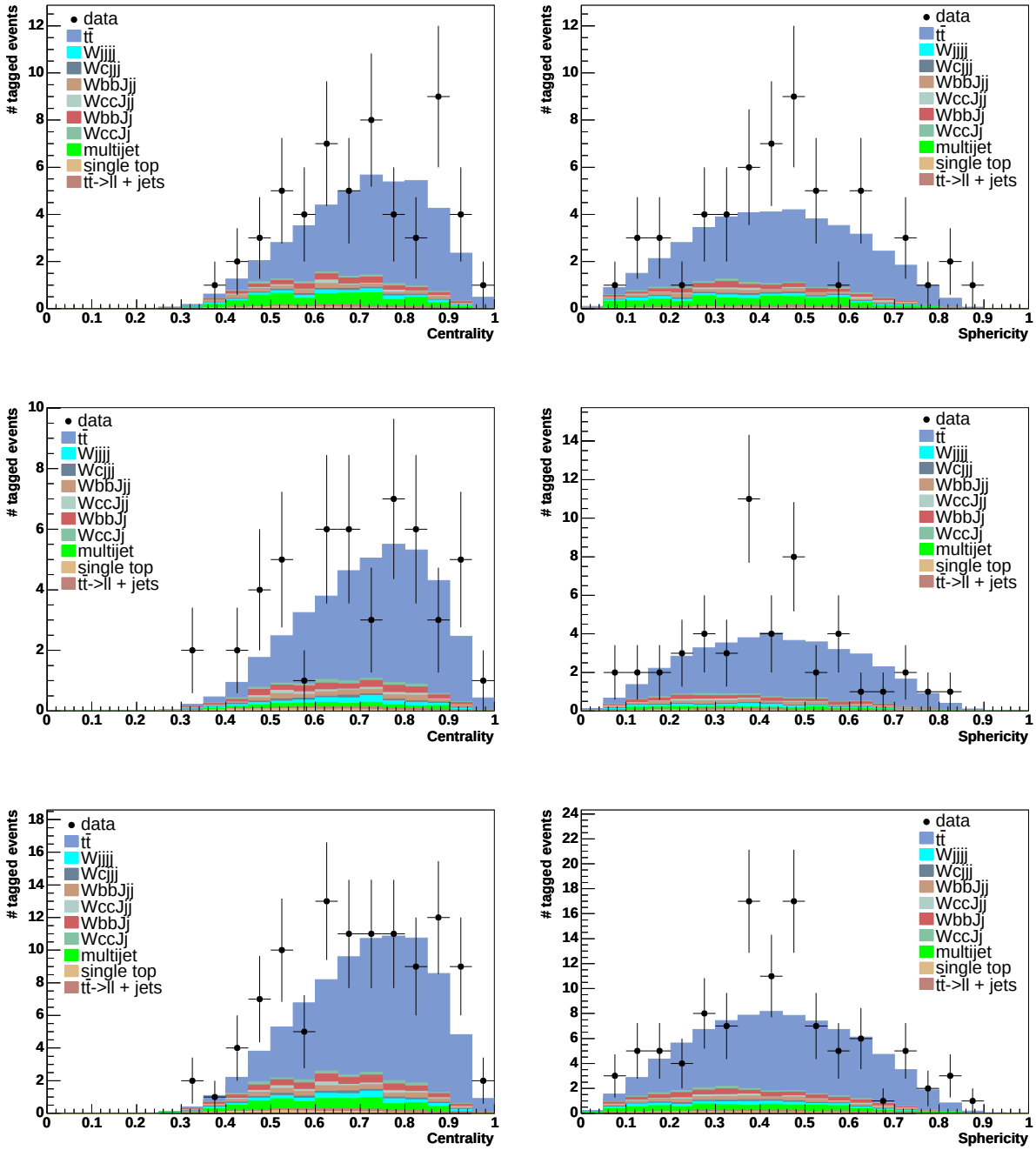

Figure A.5: Comparison between data and Monte Carlo after applying all cuts for the e+jets channel (top), the μ+jets channel (middle), and for both channels combined (bottom). The variables are the centrality (left), and the spericity (right).

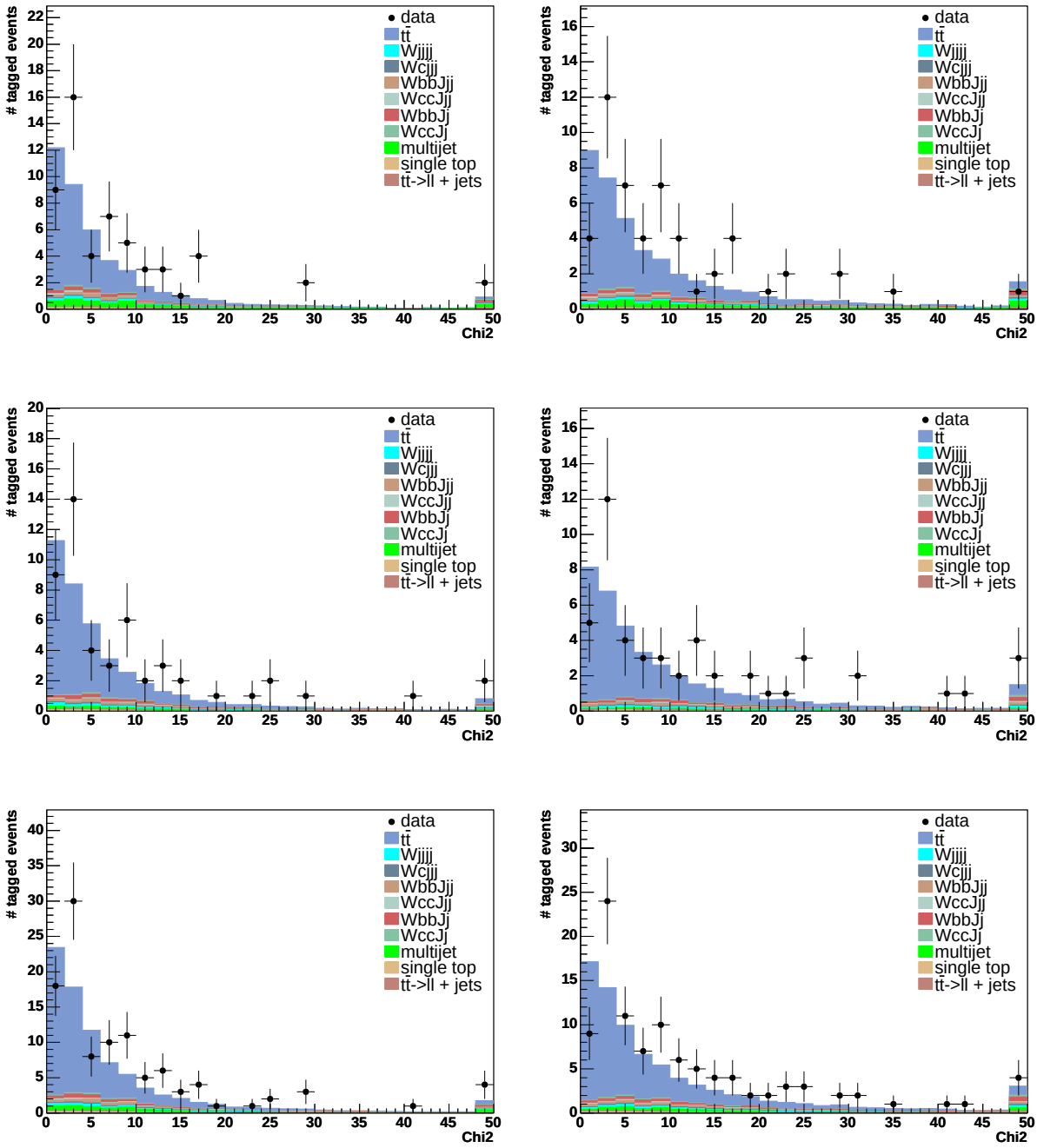

Figure A.6: Comparison between data and Monte Carlo after applying all cuts for the e+jets channel (top), the μ+jets channel (middle), and for both channels combined (bottom). The variable is the χ^2 from `HitFit` for the "Plain" method on the left, and for the "SVT" method on the right.

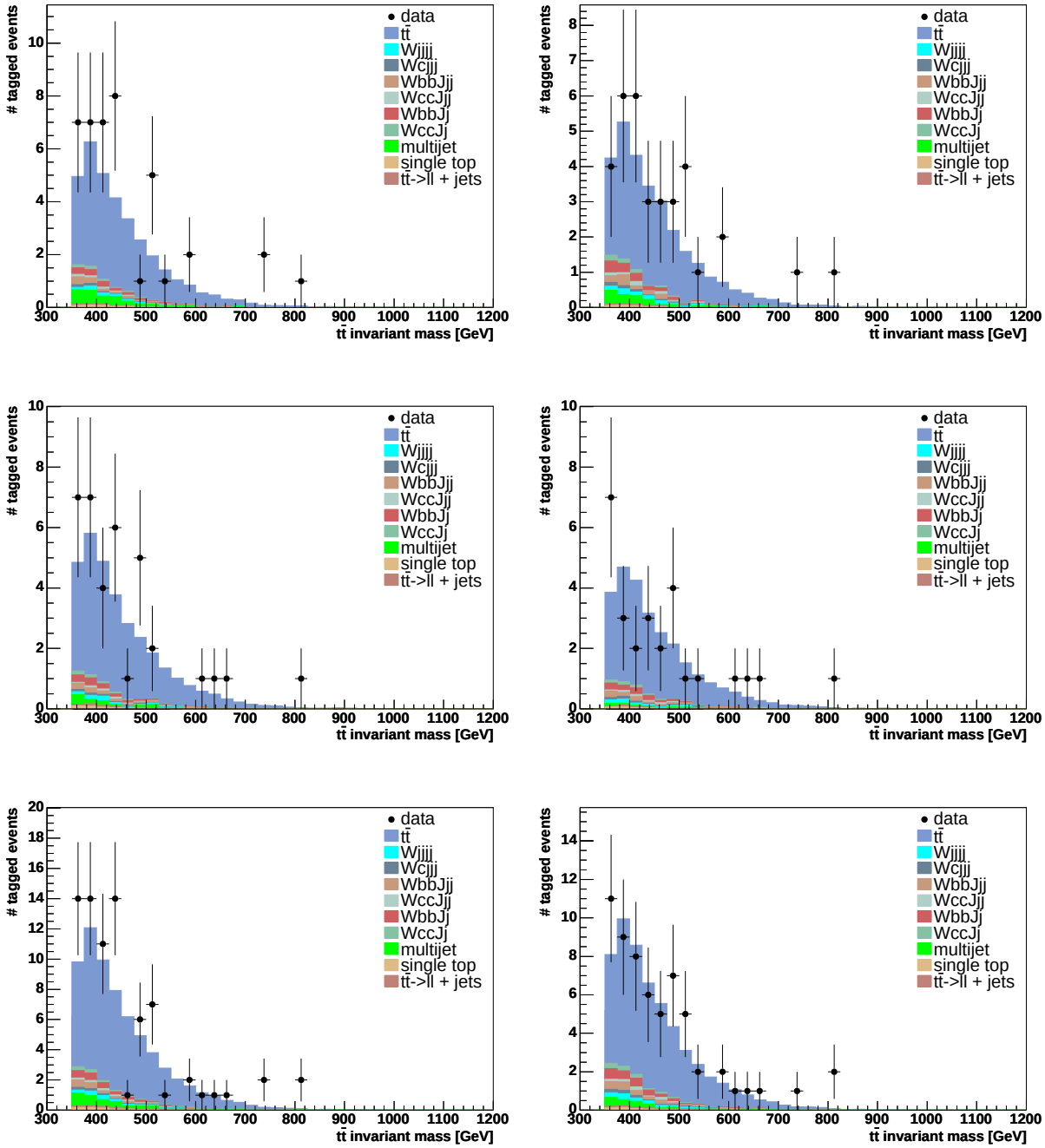

Figure A.7: Comparison between data and Monte Carlo after applying all cuts for the e+jets channel (top), the μ+jets channel (middle), and for both channels combined (bottom). The variable is the $t\bar{t}$ invariant mass distribution if $\chi^2 \leq 10$ for the "Plain" method on the left, and for the "SVT" method on the right.

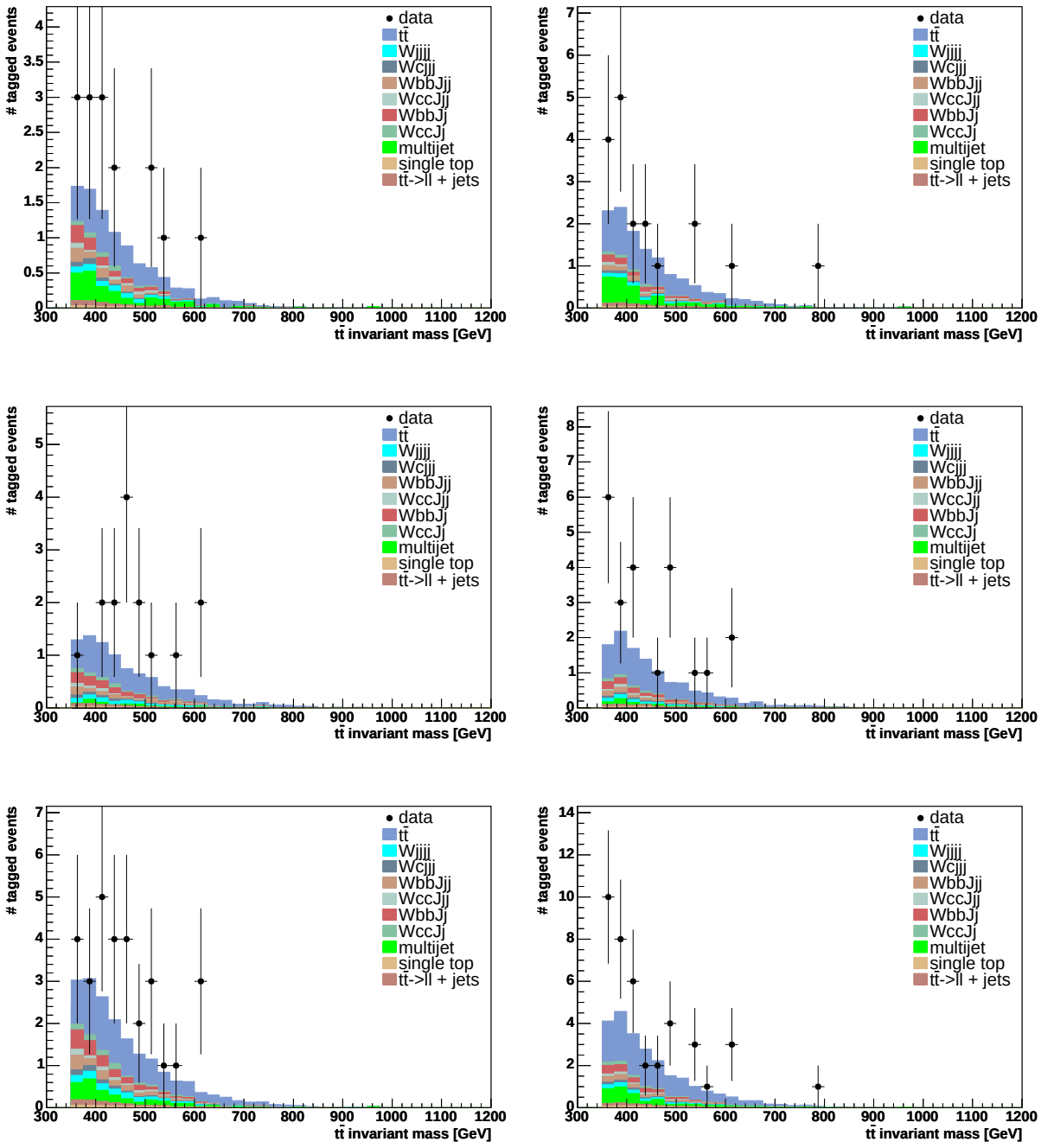

Figure A.8: Comparison between data and Monte Carlo after applying all cuts for the e+jets channel (top), the μ+jets channel (middle), and for both channels combined (bottom). The variable is the $t\bar{t}$ invariant mass distribution if $\chi^2 > 10$ for the "Plain" method on the left, and for the "SVT" method on the right.

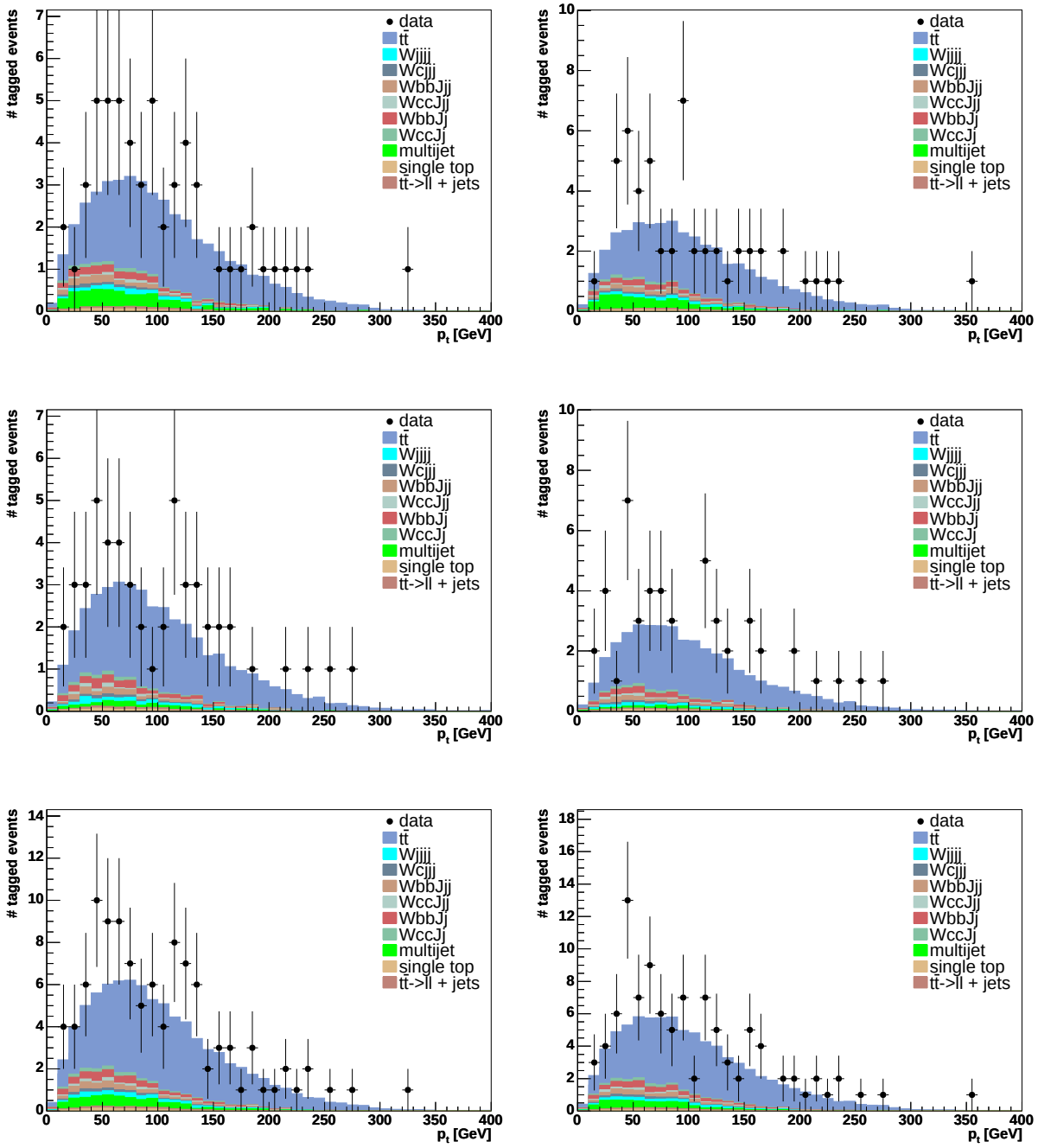

Figure A.9: Comparison between data and Monte Carlo after applying all cuts for the e+jets channel (top), the μ+jets channel (middle), and for both channels combined (bottom). The variable is the 'p_T of the top quark coming from `HitFit` for the "Plain" method on the left, and for the "SVT" method on the right.

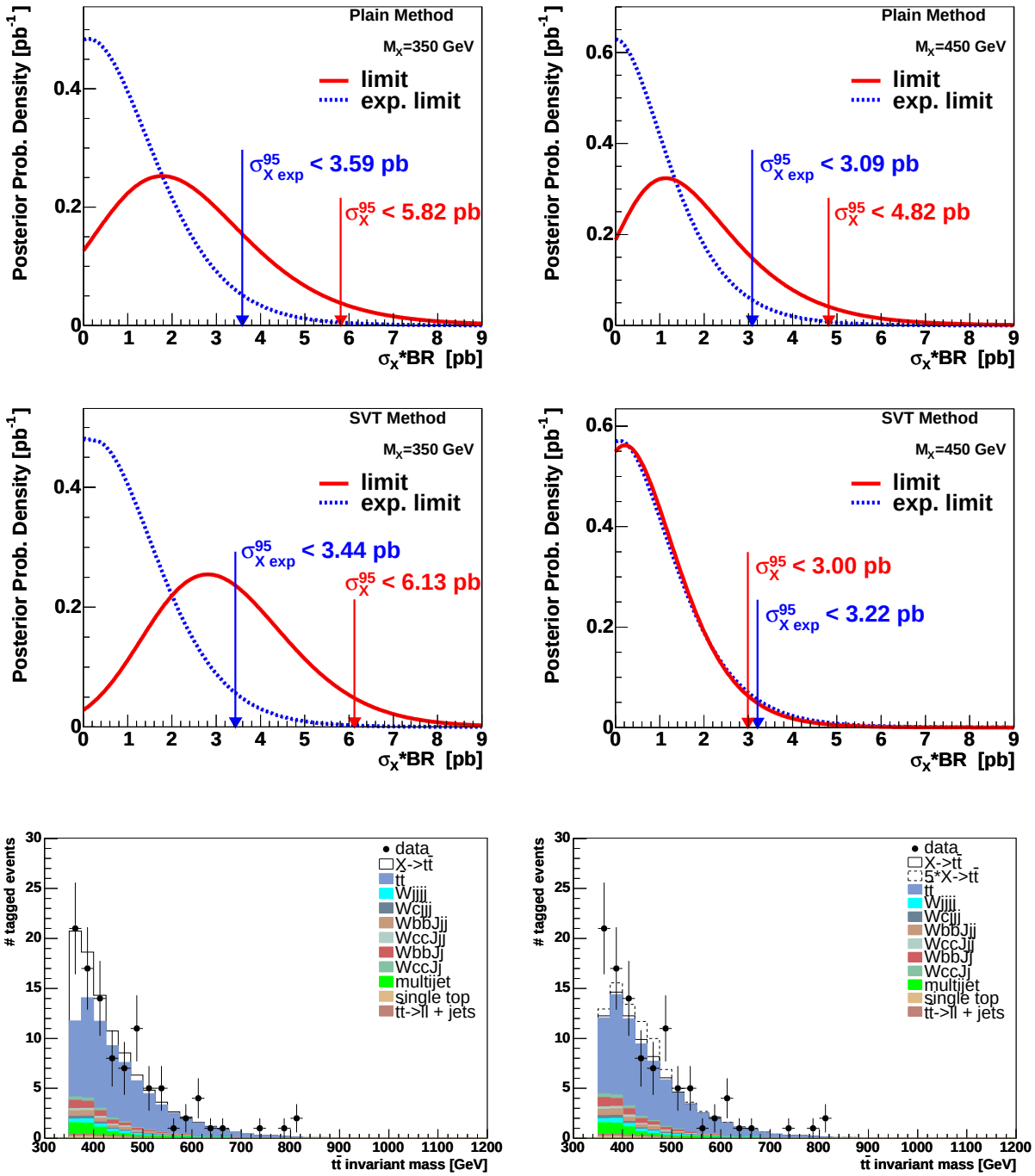

Figure A.10: Posterior probability densities are shown as a function of $\sigma_X \times B(X \to t\bar{t})$ for the "Plain" method (top) and the "SVT" method (middle). In the left column the distributions are shown for a resonance mass of 350 GeV, and in the right column for 450 GeV. In the bottom plots the $M_{t\bar{t}}$ distribution is shown with an assumed resonance contribution of 2.8 pb and (5×)0.2 pb for masses of 350 GeV and 450 GeV, respectively.

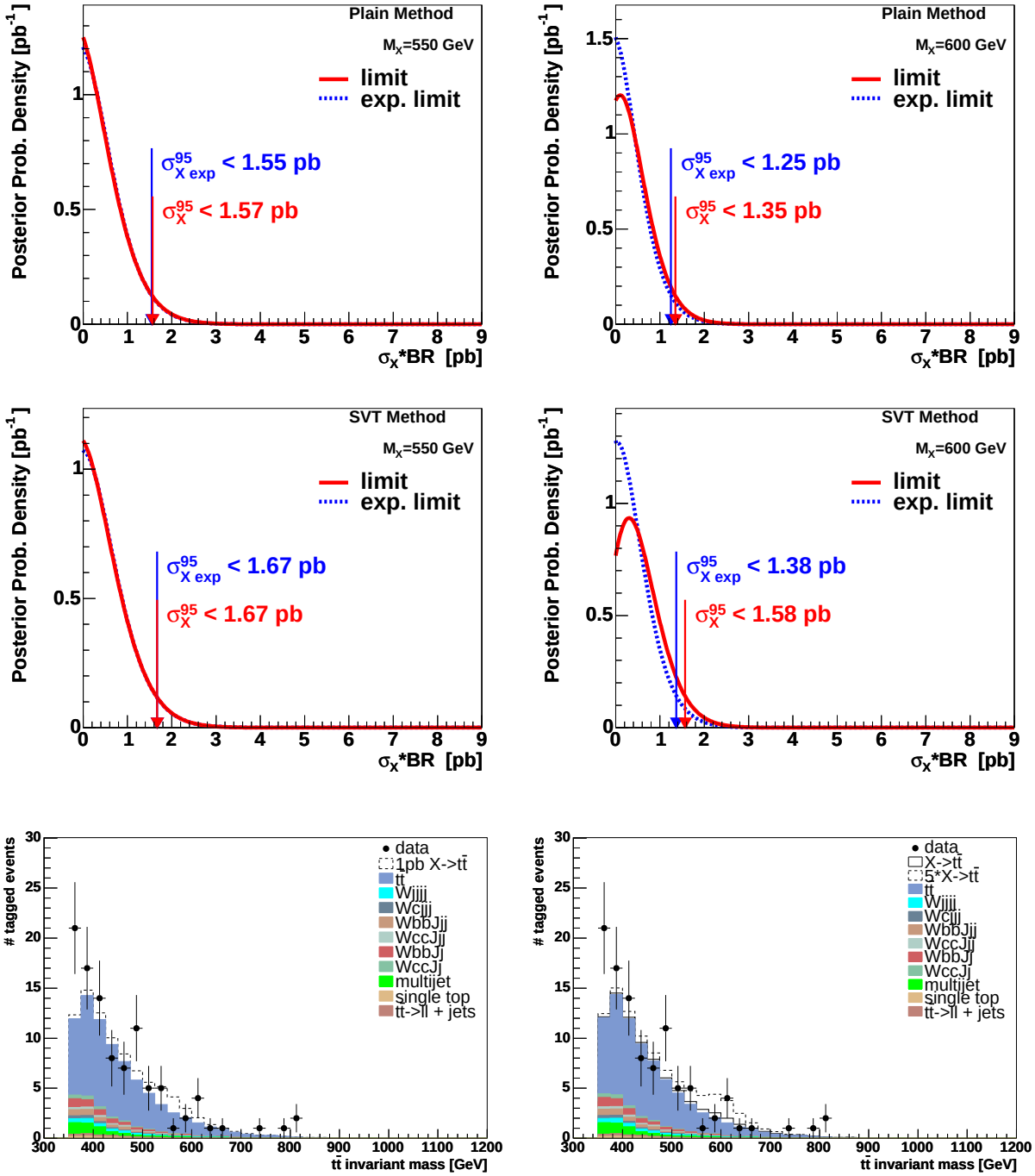

Figure A.11: Posterior probability densities are shown as a function of $\sigma_X \times B(X \to t\bar{t})$ for the "Plain" method (top) and the "SVT" method (middle). In the left column the distributions are shown for a resonance mass of 550 GeV, and in the right column for 600 GeV. In the bottom plots the $M_{t\bar{t}}$ distribution is shown with an assumed resonance contribution of 1 pb and (5×)0.3 pb for masses of 550 GeV and 600 GeV, respectively. For the mass of 550 GeV a value of 1 pb was chosen since the maximum probability density is 0.

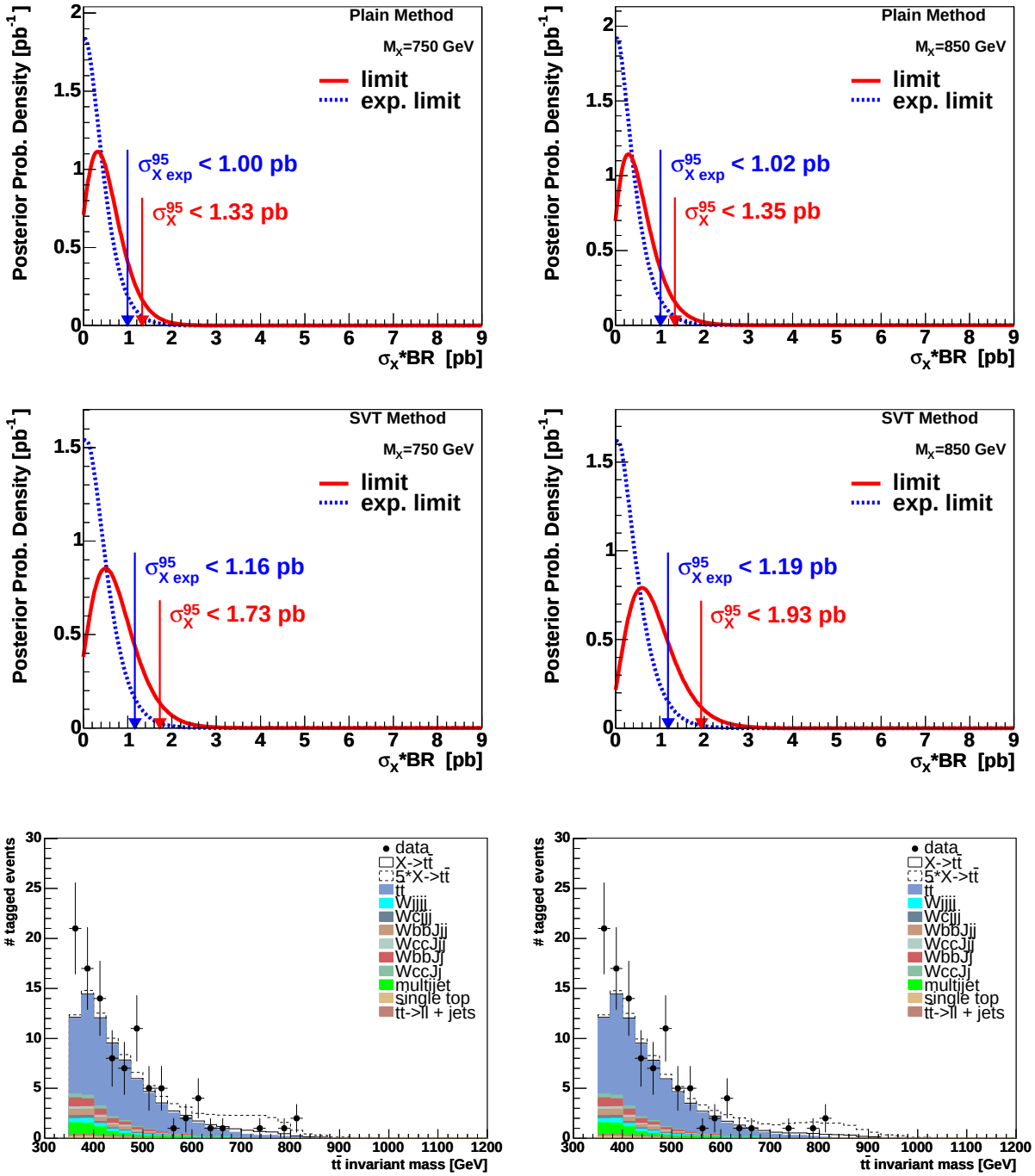

Figure A.12: Posterior probability densities are shown as a function of $\sigma_X \times B(X \to t\bar{t})$ for the "Plain" method (top) and the "SVT" method (middle). In the left column the distributions are shown for a resonance mass of 750 GeV, and in the right column for 850 GeV. In the bottom plots the $M_{t\bar{t}}$ distribution is shown with an assumed resonance contribution of (5×)0.5 pb and (5×)0.6 pb for masses of 750 GeV and 850 GeV, respectively.

Bibliography

[1] M. Kaku. Quantum field theory: A Modern introduction. New York, USA: Oxford Univ. Pr. (1993) 785 p.

[2] F. Halzen and Alan D. Martin. Quarks and Leptons: an introductory course in modern particle physics. New York, USA: Wiley (1984) 396p.

[3] David J. Griffiths. Introduciton to elementary particles. New York, USA: Wiley (1987) 392p.

[4] S. L. Glashow. Partial symmetries of weak interactions. *Nucl. Phys.*, 22:579–588, 1961.

[5] Abdus Salam and J. C. Ward. Electromagnetic and weak interactions. *Phys. Lett.*, 13:168–171, 1964.

[6] Steven Weinberg. A model of leptons. *Phys. Rev. Lett.*, 19:1264–1266, 1967.

[7] Y. Fukuda et al. Evidence for oscillation of atmospheric neutrinos. *Phys. Rev. Lett.*, 81:1562–1567, 1998.

[8] S. Eidelman et al. Review of Particle Physics. *Physics Letters B*, 592:1+, 2004.

[9] Peter W. Higgs. Broken symmetries, massless particles and gauge fields. *Phys. Lett.*, 12:132–133, 1964.

[10] R. Barate et al. Search for the standard model Higgs boson at LEP. *Phys. Lett.*, B565:61–75, 2003.

[11] Makoto Kobayashi and Toshihide Maskawa. CP violation in the renormalizable theory of weak interaction. *Prog. Theor. Phys.*, 49:652–657, 1973.

[12] Tevatron Electroweak Working Group. Combination of CDF and DØ Results on the Top-Quark Mass, 2005. FERMILAB-TM-2323-E.

[13] Scott Willenbrock. The standard model and the top quark. 2002.

[14] N. Kidonakis and R. Vogt. *Eur. Phys. J. C*, 33:466, 2004.

[15] B. W. Harris, E. Laenen, L. Phaf, Z. Sullivan, and S. Weinzierl. The fully differential single top quark cross section in next-to-leading order QCD. *Phys. Rev.*, D66:054024, 2002.

[16] T. Stelzer, Z. Sullivan, and S. Willenbrock. Single-top-quark production via W-gluon fusion at next-to-leading order. *Phys. Rev.*, D56:5919–5927, 1997.

[17] Martin C. Smith and S. Willenbrock. QCD and Yukawa Corrections to Single-Top-Quark Production via q qbar -¿ t bbar. *Phys. Rev.*, D54:6696–6702, 1996.

[18] M. Agelou et al. Search for single top quark production at DØ in RunII. DØ Note 4398, 2004.

[19] Top Group Website. http://www-d0.fnal.gov/Run2Physics/top/.

[20] The LEP Electroweak Working Group. 2006. http://lepewwg.web.cern.ch/LEPEWWG/.

[21] A. Djouadi, J. Kalinowski, and M. Spira. HDECAY: a program for Higgs boson decay in the Standard Model and its sypersymmetric extension. 1997.

[22] A. Stange, W. J. Marciano, and S. Willenbrock. Higgs bosons at the Fermilab Tevatron. *Phys. Rev. D*, 49:1354–1362, 1994.

[23] C. Quigg. Top-ology. *Phys. Today*, 50N5:20–26, 1997.

[24] D. Dicus, A. Stange, and S. Willenbrock. Higgs decay to top quarks at hadron colliders. *Phys. Lett. B*, 333:126, 1994.

[25] C.N. Yang. Selection rules for the dematerialization of a particle into two photons. *Phys. Rev.*, 77:242, 1950.

[26] Christopher T. Hill. Topcolor assisted technicolor. *Phys. Lett.*, B345:483–489, 1995.

[27] Peter L. Cho and Elizabeth H. Simmons. Searching for G3 in t anti-t production. *Phys. Rev.*, D51:2360–2370, 1995.

[28] D. Atwood, A. Kagan, and T. G. Rizzo. Constraining anomalous top quark couplings at the Tevatron. *Phys. Rev.*, D52:6264–6270, 1995.

[29] Kenneth D. Lane. Top quarks and flavor physics. *Phys. Rev.*, D52:1546–1555, 1995.

[30] Christopher T. Hill. Topcolor: Top quark condensation in a gauge extension of the standard model. *Phys. Lett.*, B266, 1991.

[31] Kenneth D. Lane and Estia Eichten. Two scale technicolor. *Phys. Lett.*, B222, 1989.

[32] Kenneth D. Lane and M. V. Ramana. Walking technicolor signatures at hadron colliders. *Phys. Rev.*, D44:2678–2700, 1991.

[33] Abdelhak Djouadi. The anatomy of electro-weak symmetry breaking. II: The Higgs bosons in the minimal supersymmetric model. 2005.

[34] Steven Weinberg. Implications of dynamical symmetry breaking. *Phys. Rev.*, D13:974–996, 1976.

[35] Leonard Susskind. Dynamics of spontaneous symmetry breaking in the Weinberg-Salam theory. *Phys. Rev.*, D20:2619–2625, 1979.

[36] Savas Dimopoulos and Leonard Susskind. Mass without scalars. *Nucl. Phys.*, B155:237–252, 1979.

[37] Estia Eichten and Kenneth D. Lane. Dynamical breaking of weak interaction symmetries. *Phys. Lett.*, B90:125–130, 1980.

[38] Kenneth D. Lane. Technicolor 2000. 2000.

[39] C. T. Hill and S. Parke. Top production: sensitivity to new physics. *Phys. Rev.*, D49:4454, 1994.

[40] R. M. Harris, C. T. Hill, and S. Parke. Cross section for Topcolor Z' decaying to $t\bar{t}$. 1999.

[41] Fermilab Visual Media Services. http://www-visualmedia.fnal.gov/VMS_Site_2/index.shtml.

[42] Fermilab Operations Devision. Accelerator Concepts. http://www-bdnew.fnal.gov/operations/rookie_books/rbooks.html.

[43] Fermilab Beams Devision. Run II Handbook. http://www-bd.fnal.gov/runII/index.html.

[44] DØ Run II data taking web page, `http://d0server1.fnal.gov/Projects/Operations/D0RunIIa_DataTaking.htm`.

[45] The DØ Collaboration. The Upgraded DØ Detector, 2005.

[46] A. M. Patwa. The Forward Preshower System and a Study of the J/ψ Trigger with the DØ Detector. FERMILAB-THESIS-2002-04, 2002.

[47] G. Borissov. Ordering a chaos or ... technical details of the AA tracking. http://www-d0.fnal.gov/atwork/adm/d0_private/2003-02-28/adm_talk.ps.

[48] A. Khanov. HTF: histogramming method for finding tracks. The algorithm description. DØ Note 3778, 2000.

[49] H. Greenlee. The DØ Kalman Track Fit. DØ Note 4303, 2004.

[50] A. Garcia-Bellido et al. Primary Vertex certification in p14. DØ Note 4320, 2004.

[51] A. Schwartzman and M. Narain. Probabilistic Primary Vertex Selection. DØ Note 4042, 2002.

[52] J. Kozminski et al. Electron Likelihood in p14. DØ Note 4449, 2004.

[53] J. Kozminski. Measurements of the top- anti-top production cross section at $\sqrt{s} = 1.96$ TeV and top mass in the dielectron channel. FERMILAB-THESIS-2005-21, 2005.

[54] C. Clement et al. MuonID Certification for p14. DØ Note 4350, 2004.

[55] Top Physics Working Group. DØ Top Analysis and Data Sample for the Winter Conferences 2004, 2004. DØ Note 4419.

[56] U. Bassler and G. Bernardi. Towards a Coherent Treatment of Calorimetric Energies: Missing Transverse Energy, Jets, E.M. Objects and the T42 Algorithm. DØ Note 4124, 2003.

[57] J.-R. Vlimant, U. Bassler, G. Bernardi, and S. Trincaz-Duvoid. Technical description of the T42 algorithm for the calorimeter noise suppression. DØ Note 4146, 2003.

[58] G. Bernardi, E. Busato, and J.-R. Vlimant. Improvements from the T42 Algorithm on Calorimeter Objects Reconstruction. DØ Note 4335, 2004.

[59] G. Blazey et al. Run II Jet Physics. DØ Note 3750, 2000.

[60] S. Grinstein et al. Inclusive Jet Cross Section using the k_T Algorithm. DØ Note 3777, 2001.

[61] T. Golling. Measurements of the top quark pair production cross section in l+jets final states using a topological multivariate technique as well as lifetime b-tagging in $p\overline{p}$ collisions at $\sqrt{s} = 1.96$ TeV with the DØ detector at the Tevatron. FERMILAB-THESIS-2005-01, 2005.

[62] N. Gollub et al. Update on the Measurement of the $t\bar{t}$ Production Cross-Section at $\sqrt{s} = 1.96$ TeV in the Muon+Jets Final State using a Topological Method on PASS2 data. DØ Note 4667, 2005.

[63] J.-L. Agram et al. Jet Energy Scale at DØ RunII. DØ Note 4720, 2005.

[64] DØ Jet Energy Scale study group, `http://www-d0.fnal.gov/phys_id/jes/d0_private/certified/v5.3/links.html`.

[65] R. Demina et al. b-tagging with Counting Signed Impact Parameter method. DØ Note 4049, 2002.

[66] D. Bloch and B. Clement. Update of the JLIP b-tagger performance in p14/pass2 with Jes 5.3. DØ Note 4824, 2005.

[67] A. Schwartzman and M. Narain. b-quark jet identification via Secondary Vertex Reconstruction. DØ Note 4080, 2003.

[68] A. Schwartzman and M. Narain. b-quark jet identification via Secondary Vertex reconstruction in DØ reco p13 Software. DØ Note 4081, 2003.

[69] D. Boline et al. Update on b-quark jet identification with Secondary Vertex reconstruction using DØreco version p14-Pass2. DØ Note 4796, 2004.

[70] K. Hanagaki and J. Kasper. Identification of b-jet by Soft Muon. DØ Note 4867, 2005.

[71] T. Scanlon. A Neural Network b-tagging Tool. DØ Note 4889, 2005.

[72] T. Scanlon and M. Anastasoaie. Performance of the NN b-tagging Tool on Pass 2 p14 Data. DØ Note 4890, 2005.

[73] C. E. Gerber et al. Taggability in p14 pass2 data. DØ Note 4995, 2005.

[74] C. Clement et al. Measurement of the $t\bar{t}$ Production Cross-Section at $\sqrt{s} = 1.96$ TeV using lifetime tagging. DØ Note 4900, 2005.

[75] M. Begel et al. The Top Trigger Package: Including Version 13 Triggers and Other Improvements. DØ Note 4883, 2005.

[76] K. Ranjan et al. Calorimeter Event Quality Using Level 1 Confirmation. DØ Note 4554, 2004.

[77] T. Edwards et al. FERMILAB-TM-2278-EB.

[78] D. Stump et al. Inclusive jet production, parton distributions, and the search for new physics. *JHEP*, 10:046, 2003.

[79] T. Sjostrand, L. Lonnblad, and S. Mrenna. PYTHIA 6.2: Physics and manual. 2001.

[80] `http://www-d0.fnal.gov/computing/MonteCarlo/simulation/d0sim.html`.

[81] Y. Fisyak and J. Womersley. D0gstar D0 GEANT Simulation of the Total Apparatus Response. DØ Note 3191, 1997.

[82] M. Agelou et al. Top Trigger Efficiency Measurement and the top_trigger packacke. DØ Note 4512, 2004.

[83] `http://www-clued0.fnal.gov/d0_mess/`.

[84] S. Jadach, Z. Was, R. Decker, and Johann H. Kuhn. The tau decay library TAUOLA: Version 2.4. *Comput. Phys. Commun.*, 76:361–380, 1993.

[85] M. L. Mangano, M. Moretti, F. Piccinini, R. Pittau, and A. D. Polosa. ALPGEN, a generator for hard multiparton processes in hadronic collisions. *JHEP*, 07:001, 2003.

[86] E. Boos et al. CompHep 4.4: automatic computations from lagrangians to events. *Nucl. Instrum. Meth.*, A534:250–259, 2004.

[87] C. Clement et al. Measurement of the $t\bar{t}$ Production Cross-Section in the Electron+Jets Final State using a Topological Method on 366 pb^{-1} of DØPass-2 Data at $\sqrt{s} = 1.96$ TeV. DØ Note 4662, 2005.

[88] V.M. Abazov et al. Direct Measurement of the Top Quark Mass. *Phys. Rev. Lett.*, 79:1197, 1997.

[89] J. Peter Berge, F. T. Solmitz, and H. D. Taft. *Rev. of Scientific Instruments*, 32 (5):538–548, 1961.

[90] Top Physics Working Group. Direct measurement of the top quark mass in the lepton+jets channel using Run II data, 2004. DØ Note 4426.

[91] S. S. Snyder. Measurements of the top-quarks mass at DØ. Doctorial thesis, SUNY, Stony Brook, May , 1995.

[92] M. Agelou et al. Improved search for single top quark production. DØ Note 4670, 2005.

[93] V.M. Abazov et al. Search for Narrow $t\bar{t}$ Resonances in $p\overline{p}$ Collisions at $\sqrt{s} = 1.8$ TeV. *Phys. Rev. Lett.*, 92:221801, 2004.

[94] T. Affolder et al. Search for new particles decaying to $t\bar{t}$ in $p\overline{p}$ Collisions at $\sqrt{s} = 1.8$ TeV. *Phys. Rev. Lett.*, 85:2062, 2000.

[95] The DØ Collaboration. Search for a $t\bar{t}$ Resonance in $p\overline{p}$ Collisions at $\sqrt{s} = 1.96$ TeV in the Lepton+Jets Final State, 2005. DØ Note 4880-CONF.

[96] The CDF Collaboration. Search for resonant $t\bar{t}$ production in $p\overline{p}$ Collisions at $\sqrt{s} = 1.96$ TeV, 2005. CDF Note 8087.

Acknowledgments

At first I would like to thank my supervisor Prof. Dr. Peter Mättig for giving me the opportunity to work on top-quark physics, especially in an international collaboration. His interest and enthusiasm in this analysis were very valuable not only since the almost discovery in the conference result. I am particularly grateful for the frequent long-term stays at Fermilab which made it possible to keep up-to-date with the developments in the groups at DØ.

Without the infrastructure and input of the top group at DØ this analysis could not have been carried out. I am deeply grateful to Dr. Aurelio Juste for his commitment and support especially during the stressful time leading to the conference result. I also want to thank Dr. Arnulf Quadt for his encouragements and the moral support.

In addition I have to thank all members of the Wuppertal particle physics group for the great working environment. The atmosphere in Wuppertal was always very enjoyable and the infrastructure well maintained. German colleagues from Wuppertal who shared time with me at Fermilab made the stays very pleasant and being away from home easier. To Dr. Christian Schmitt I owe special thanks for the support and all the fruitful discussions not only about physics. Dr. Klaus Hamacher and Dr. Daniel Wicke always had an open door when experience and further knowledge were needed for the analysis, thank you for that.

Zum Schluß gebührt mein Dank natürlich meiner Familie, der ich unendlich dankbar bin für die unermüdliche Unterstützung, die sie mir mein ganzes Leben lang hat zuteil kommen lassen. Zu allerletzt möchte ich an meinen guten Freund Kay Bente erinnern ohne den ich wohl nicht in Wuppertal Physik studiert hätte. Ihm möchte ich postum dafür danken, dass ich den Weg durch das Physikstudium nicht alleine gehen musste.